Imperial College London
Department of Physics

Diagnosing Particle Acceleration in Pulsed Power Driven Magnetic Reconnection Experiments

J. W. D. Halliday

March 2020

Supervised by S. V. Lebedev

Submitted in part fulfilment of the requirements for the degree of
Doctor of Philosophy in Physics of Imperial College London
and the Diploma of Imperial College London

Declaration of Originality

I hereby certify that all work contained within this thesis is entirely original and my own work, unless otherwise stated.

J. Halliday
April 17, 2020

Copyright Notice

Abstract

Acknowledgements

I would like to thank Jack Hare for preparing this thesis template.

This work was also supported in part by the Engineering and Physical Sciences Research Council (EPSRC) EP/N013379/1, aand by the U.S. Department of Energy (DOE) Awards No. DE-F03-02NA00057, DE-SC-0001063, and DE-NA-0003764.

Contents

List of Tables

List of Figures

1 Introduction and Background

Magnetic reconnection describes a dissipation process through which the field lines in a magnetised plasma are able to break and rejoin, enabling a global change in the magnetic field topology. This change enables the energy stored within magnetic fields into be efficiently converted into energy associated with the particles in the plasma. It leads to bulk plasma heating; increases in plasma flow velocity; and the generation of fast particles.

Magnetic reconnection is frequently invoked to describe transient phenomena in magnetised plasmas across an incredible range of spatial scales [Zweibel, 2009]. Astrophysical examples include the acceleration of pulsar winds [Lyubarsky, 2000] and the formation of gamma ray bursts [Thompson, 1994]. In space physics, reconnection is relevant to processes including the eruption of solar flares [Forbes, 1991] and the interaction of the solar wind with planetary magnetospheres [Gosling, 2012]. For magnetically confined plasmas, it is necessary to describe the sawtooth instability in tokamaks [Yamada, 1994]. It has also been claimed that reconnection plays a part in hohlraum plasma evolution, so is a relevant process for inertial confinement fusion [Nilson, 2006].

It seems lacking to talk about reconnection without some discussion of solar flares as these are the original phenomena which magnetic reconnection was invoked to describe [Parker, 1957], and because they are an extraordinary beautiful example of a physical system in which magnetic reconnection is important – see for example the observational data shown in figure 1.1.

Solar flares are defined as a localised brightening of the solar emission spectrum on time scales lasting minutes to hours [Benz, 2016]. Enhanced brightness is typically observed across a very wide range of photon energies, with prominent emission in the Hα (visible); hard X-Ray ($\sim 1\,\mathrm{keV}$); and very hard X-Ray ($\sim 10\,\mathrm{keV}$) regions. They occur within active regions of the photosphere near solar prominences (loops of plasma supported by magnetic field lines that protrude from the solar surface, as shown in figure 1.1). The hard X-Ray emission is produced due to the heating of plasma within coronal loops; very hard X-Ray emission is Bremsstrahlung radiation produced by fast electrons streaming down field lines; and Hα emission is exited by fast particles slowing down as they move from the collisionless corona to the collisional photosphere [Benz, 2016]. Spectroscopic measurements of Zeeman splitting show that the onset of solar flairs are associated with the build-up of stress in magnetic fields in the surrounding active region and this stress is reduced after a flair has occurred [Zweibel, 2009].

Taken together these observations are a strong indication that reconnection is the mech-

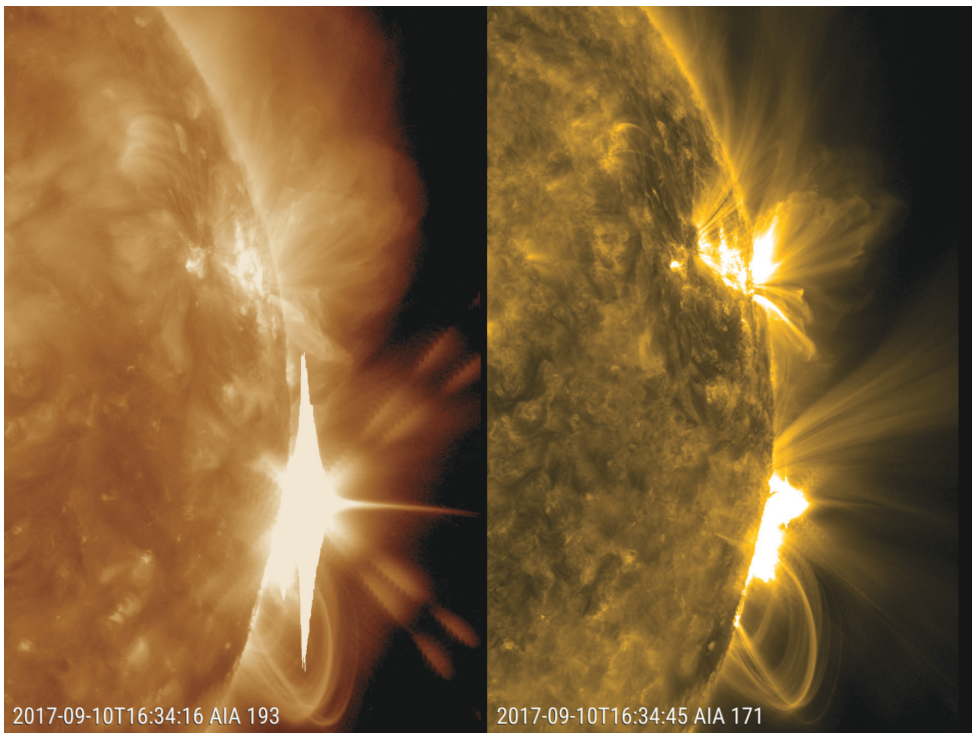

Figure 1.1: Extreme ultra violet (XUV) images obtained with the Solar Dynamics Observatory's Atmospheric Imaging Assembly (AIA) [Lemen, 2012]. The images show the eruption of an active region of the solar surface – producing an X8 solar flare. *Left:* Image from the instrument's 193 Å channel (optimised for spectral features associated with Fe XII and Fe XXIV). *Right:* Image from the instrument's 171 Å channel (optimised for spectral features associated with Fe IX). Credit: Solar Dynamics Observatory, NASA.

anism which drives the production of flares: Magnetic field observations demonstrate that flare onset is associated with an adjustment of global field topology, and X-Ray emission indicates that this adjustment coincides with plasma heating and non-thermal particle acceleration, all key signatures of reconnection.

Whilst it is generally accepted that reconnection is the mechanism which drives solar flares, models describing the precise nature of this reconnection are still far from adequate. Observations indicate that reconnection should occur over longer length-scales and shorter time-scales than models are able to explain. Furthermore, the number of fast particles inferred from observations are much greater than the number models are able to ascribe to a single reconnection event [Zweibel, 2009]. In some flares, the number of accelerated electrons can even become comparable to the number of electrons in the thermal bulk [Krucker, 2010], suggesting that non-thermal acceleration has a strong influence on the way reconnection proceeds in these systems.

Although plasma in solar active regions is relatively collisionless and weakly driven, it is worth emphasising that magnetic reconnection is frequently invoked to describe transient phenomena in more strongly driven and collisional plasmas. An example of a more collisional environment in which reconnection is potentially important is in the plasma of the solar convective zone, where the collisional length scale is only a factor of a few larger than the Debye length and so phenomena ought to be well described by the physics of resistive magneto-hydrodynamics (MHD) [Ryutov, 2015].

Reconnection has been an active area of research in space physics since at least the late 1950s [Parker, 1957], however in the last twenty years advances in computing power; an increase in the fidelity of satellite observations; and the emergence of dedicated laboratory experiments have enabled profound improvements in our understanding of the physics mediating magnetic reconnection. Conceptual advancements in our understanding which are still seen as novel include acknowledgement of the need to invoke kinetic or two-fluid descriptions in order to account for the separation of electrons and ions in the reconnection layer; understanding the importance of instabilities in reconnecting plasma geometries; and the way in which three dimensional reconnecting systems differ from two dimensional ones.

In spite of this progress, there still exist a number of open problems in magnetic reconnection research. It has been suggested [Zweibel, 2016], that conceptual issues with reconnection fall into four broad categories:

1. *The rate problem* – The reconnection rate sets the timescale over which magnetic flux is annihilated. Historically models of reconnection predicted timescales many orders of magnitude larger than those which were seen in physical systems.

2. *The trigger/onset problem* – Essentially this describes the idea of understanding what determines the amount of energy that can be built up in magnetic flux before a system disrupts and the energy is dissipated through reconnection.

3. *The interplay of scales problem* – This describes the idea that the length scales over

which magnetic field lines are able to break lie within the realm of microphysics and that these scales are potentially separated from global scales (over which magnetic energy is stored and the plasma responds) by many orders of magnitude. In order to arrive at a complete picture of the reconnection process it is important to understand how the different length scales are coupled together.

4. *The energy balance problem* – This describes the idea of being able to predict what fraction of the dissipated magnetic is given to different degrees of freedom associated with the plasma (such as plasma heating, plasma acceleration, and fast particle generation) for a given system.

Historically, the rate problem was considered of primary importance [Parker, 1957], but recent work has gone a long way to resolving this problem [Zweibel, 2016]. In particular current sheet instability [Loureiro, 2007]; two fluid effects leading to in-plane electric fields [Yamada, 2006]; and anomalous resistivity due to kinetic turbulence have all been shown to increase the reconnection rate.

Comment: Add reference for kinetic turbulence statement

The original goal of the work presented in this thesis was to measure signatures of particle acceleration in pulsed power driven magnetic reconnection experiments. In a broad sense, this falls under the scope of attempting to address the energy balance problem.

This chapter will begin by discussing theoretical models of reconnection and some mechanisms for particle acceleration in magnetic reconnection. I will then give an overview of some of the most prominent dedicated reconnection experiments in order to provide context for the work presented here. Finally, I will self emission processes which are relevant to high energy density (HED) plasma physics. The final section might seem a little out of place but it is important because the diagnostic signatures of particle acceleration discussed later in this thesis are all spectroscopic and so some level of atomic physics is required in order to interpret experimental data.

1.1 Theoretical Models of Magnetic Reconnection

1.1.1 Sweet Parker Reconnection

The prototypical theory describing magnetic reconnection is the Sweet Parker Model [Parker, 1957; Sweet, 1958]. This is a steady state, incompressible, single fluid, MHD model in which magnetic diffusivity is invoked as the sole dissipative process. The geometry of this model is shown in figure 1.2. This shows two regions of oppositely directed magnetic field which are frozen into plasma inflows. Where the two inflows meet a diffusion region is formed, and magnetic reconnection occurs within this region. In the diagram,

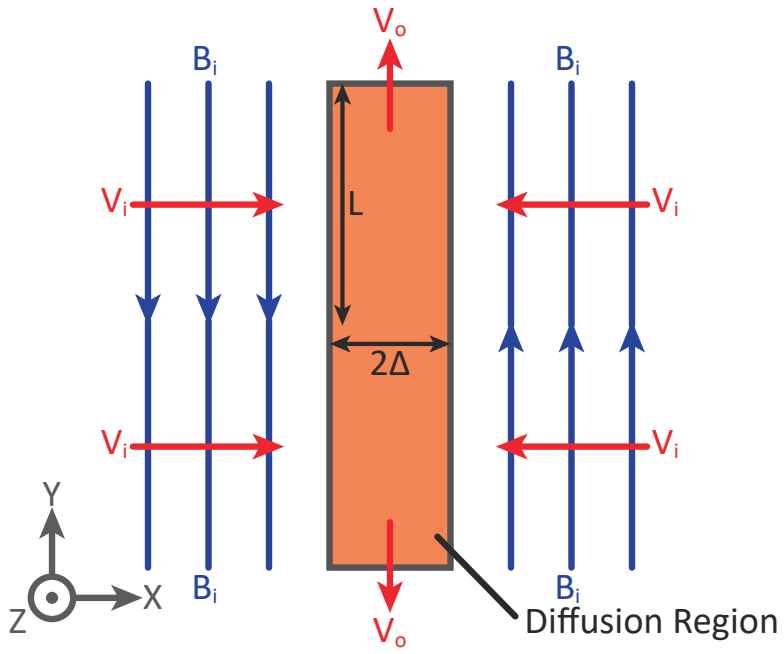

Figure 1.2: A diagram of the Sweet Parker reconnection geometry. The diffusion region is shaded in orange; the direction of magnetic field is indicated with blue arrows; and the direction of fluid velocity is indicated with red arrows. The system is invariant in the Z direction.

the subscript i denotes the value of a plasma parameter in the inflow region; the subscript o denotes the value of a plasma parameter in the outflow region; the half-*width* of the diffusion region is labelled Δ; the half-*length* of the layer is labelled L; $\mathbf{E}$ is the eletric field; $\mathbf{B}$ is the magnetic field; and $\mathbf{v}$ is the plasma velocity.

From Faraday's law it follows that

$$\oint \mathbf{E} \cdot d\mathbf{l} = 0, \tag{1.1}$$

since, in steady state, $\partial \mathbf{B}/\partial t = \mathbf{0}$. By considering an arbitrary contour integral in the plane perpendicular to figure 1.2 it can be shown that the out of plane component of electric field (E_Z) does not vary as a function of position. This constant (out of plane) field is referred to as the reconnecting electric field.

In order to understand what supports the reconnecting electric field, consider Ohm's law for a conducting fluid

$$\mathbf{E} + \mathbf{v} \times \mathbf{B} = \eta \mathbf{j}, \tag{1.2}$$

here η is the plasma resistivity; and $\mathbf{j}$ is the current density. In the inflow region, the reconnecting electric field is supported entirely by plasma motion and so $E_Z = V_i B_i$. In the diffusion region, the magnetic field vanishes and so $E_z = \eta j_z$. From the integral form of Ampere's law, neglecting displacement current, it follows that $j_z = B_i/(\mu_0 \Delta)$. By

combining these results, one obtains the result

$$v_i = \frac{\eta}{\mu_0 \Delta}. \tag{1.3}$$

Physically this result can be understood as a statement of the fact that, in order to support a steady state, the plasma carries field lines in to the system at the same rate as the field diffuses outwards [Priest, 2000, p. 120].

From mass continuity it follows that

$$L v_i \rho = \Delta v_o \rho, \tag{1.4}$$

where ρ is the plasma mass denisty. This can be combined with equation 1.3 to obtain the result

$$v_i^2 = \frac{\eta v_o}{\mu_0 L}. \tag{1.5}$$

Sweet Parker Outflow Velocity

A key question to address is what sets the outflow velocity in the Sweet Parker reconnection. This can be obtained by considering the steady state form of the momentum equation

$$\rho \mathbf{u} \cdot \nabla \mathbf{u} = -\nabla p + \mathbf{j} \times \mathbf{B}, \tag{1.6}$$

where p is the pressure. If plasma pressure is neglected then the form of this equation in the outflow region is

$$\frac{\rho v_o^2}{L} \approx (\mathbf{j} \times \mathbf{B_o}) \cdot \hat{x} \approx j_z B_0 = \frac{B_i B_o}{\mu_0 \Delta}, \tag{1.7}$$

where the last step follows from using the expression for j_z which was stated previously.

From the fact that magnetic field is divergence-free, it follows that $B_o/\Delta \approx B_i/L$ and combining this with equation 1.7 gives

$$v_o \approx \frac{B_i}{\sqrt{\mu_0 \rho}} = v_{A,i}, \tag{1.8}$$

where $v_{A,i}$ is the inflow Alfvén speed. The physical interpretation of this result is that magnetic tension in the outflows accelerates plasma to $v_{a,i}$.

Sweet Parker Reconnection Rate

The reconnection rate is defined as the ratio of the inflow speed to the Alfvén speed. By combining equations 1.8 and 1.5, one obtains the result

$$\frac{v_i}{v_{A,i}} \approx \frac{1}{\sqrt{S}}, \tag{1.9}$$

where S is a dimensionless quantity which is known as the Lundquist number and is given by

$$S = \frac{\eta}{\mu_0 L v_{A,i}}. \tag{1.10}$$

The strong Lundquist number dependence in the predicted reconnection rate is the essential problem with the Sweet Parker mechanism. Observational and experimental evidence generally suggests that reconnection generally happens at a much faster rate than predicted [Zweibel, 2009] and is only very weakly dependant on Lundquist number [Loureiro, 2016]. For example, in a solar flare, large spatial scales drive Lundquist numbers to values $\sim 10^6 - 10^{12}$, and this gives rise to predicted reconnection rates $\sim 10^{-3} - 10^{-6}$ [Priest, 2000], implying that energy dissipation should take several days. In reality flares take only a few hours to dissipate, suggesting a true reconnection rate of order $10^{-2} - 10^{-1}$.

1.1.2 Fast Reconnection

Reconnection models are said to be fast when they predict a reconnection rate which scales as $S^{-\gamma}$, with $\gamma < 1/2$, so predict faster reconnection rate than Sweet Parker for a given Lundquist number [Priest, 2000].

It is tempting to think that Sweet Parker might under predict reconnection rates because single fluid resistive MHD does not properly resolve the phenomena which truly mediate fast reconnection. Theories treating reconnection in more complex frameworks, ranging from extended MHD to fully kinetic models, have been proposed. The problem with this line of thinking is that there are certainly astrophysical observations of reconnection, which are believed to be well described by resistive MHD, where Sweet Parker still under predicts the reconnection rate [Loureiro, 2016].

Models able to support fast reconnection across a large range of parameter space typically do so by introducing some process which stops the system from caring about the global length scale of the system. An example of a model that achieves fast reconnection in this way is the plasmoid instability.

1.1.3 The Plasmoid Instability

An implicit assumption in the Sweet Parker treatment of reconnection is that the Sweet Parker reconnection geometry is stable. If this were not the case then assuming a steady state would be invalid. It has been shown that, above some critical Lundquist number (S_C), Sweet Parker type current sheets are unstable to special case of the resistive tearing instability, known as the plasmoid instability [Loureiro, 2007]. If plasma flows in the system are well described by resistive MHD then the value of S_C has no parametric dependence: It is just a number of order 10^4 [Biskamp, 1986].

As shown in figure 1.3, resistive tearing allows a region of the reconnection layer to 'pinch off', forming a island of enhanced magnetic flux and plasma density, with an 'O-point' field topology, known as a plasmoid. If the layer is remains unstable then this process

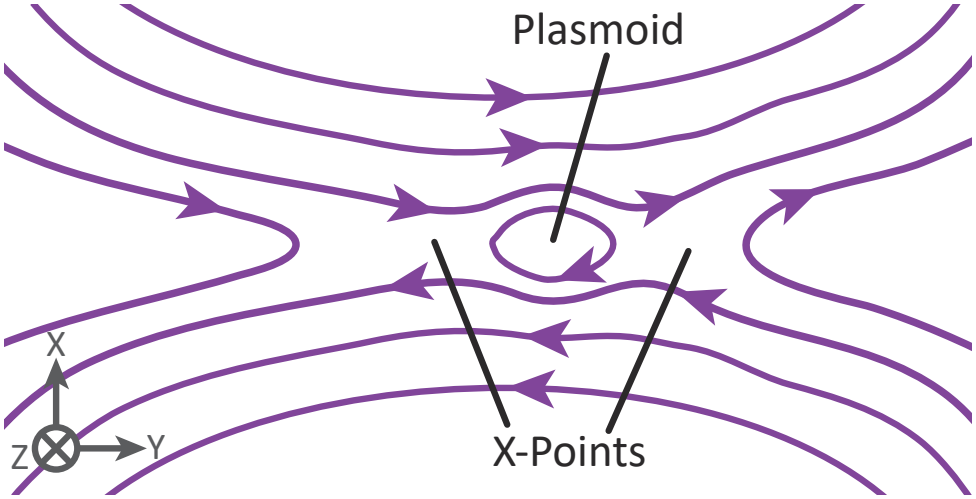

Figure 1.3: Magnetic field lines in a current sheet which has broken up due to the plasmoid instability. The Diagram shows a single plasmoid (O-Point field structure) with two secondary current sheets (X-Point field structure) on either side of it.

happens repeatedly and the reconnection layer will contain a number of plasmoids at any one time. The plasmoids are generally advected out of the layer but when two meet they may coalesce. The regions between two plasmoids have an 'X-line' field structure, and are known as a secondary current sheets.

Thus a reconnection layer of sufficient length will develop a stochastic, fractal-like structure containing many plasmoids, separated by secondary current sheets with a distribution of different lengths. The shortest length of a secondary current sheet will be a length L_C, where $S_C = S(L_C)$. The reconnection rate of the system will be set by these shortest current sheets but will take the form predicted by Sweet Parker, so $u_i/u_{A,i} \sim S_C^{1/2}$ [Loureiro, 2016]. This means the rate is independent of the global system length scale so it fulfils the criteria for fast reconnection.

Although the theory of the plasmoid instability was initially developed for resistive MHD, two-fluid and kinetic theories of reconnection which predict plasmoids have also been proposed [Loureiro, 2016]. These are qualitatively similar to the picture described above but quantitatively distinct (i.e. different growth rates are predicted). For example, in a regime where two fluid effects become important, a variant of the standard plasmoid instability, known as the semi-collisional plasmoid instability emerges. In this regime, the value of the critical Lundquist number required for plasmoids to form is significantly suppressed compared to the resistive MHD case [Loureiro, 2016]. This is interesting because Lundquist numbers exceeding 10^4 are hard to achieve in an experiment, so the semi-collisional form of the instability has proven easier to verify experimentally [Hare, 2017b].

1.1.4 Particle acceleration mechanisms in magnetic reconnection

One of the primary signatures of reconnection from space physics observations (for example in the eruption of solar flares) is the generation of fast particles. The theoretical descriptions

of reconnection we have discussed were been routed in a MHD framework and there was little discussion of collisionless processes which are required for the non thermal particle acceleration. That said, MHD can provide information relevant to understanding how fast particles are generated: If plasma flows are approximately thermal with a relativity small population of fast particles then the models described above may provide information about background plasma conditions experienced by the non thermal population.

In the context of the plasmoidal reconnection geometry, shown in figure 1.3, two prominent acceleration mechanisms have been proposed. The first of these is direct acceleration by the electric field, which causes acceleration at X-points and in the direction perpendicular to the reconnection plane [Priest, 2000]. The second is a Fermi type acceleration process, which accelerates particles isotropically in the reconnection plane and occurs within plasmoids [Drake, 2006].

Direct Acceleration by the Reconnecting Electric Field

Figure 1.4 (a) shows data from a particle in cell (PIC) simulation [Totorica, 2017] where the trajectory of a test electron undergoing direct acceleration is plotted in red. The figure shows that the electron repeatedly scatters off the strong inflow magnetic field so is trapped within the reconnection layer and that it gains a large amount of energy before exiting the simulation volume. Because the magnetic field acting on the electron within the reconnection layer is relatively weak, it is able to travel more easily in the z direction (when compared to an electron in the inflow region) and so it is efficiently accelerated by the reconnecting electric field. The energy gained by a trapped electron ($\Delta\varepsilon$) as a result of its motion is given by

$$\Delta\varepsilon = E_z d_z, \tag{1.11}$$

where d_z is the distance which the electron travels in the z direction [Priest, 2000, p. 478]. This is the same result as for a particle travelling in a constant electric field and zero magnetic field. It is in dramatic contrast with the well known result for a particle travelling in *constant* electric and magnetic fields, which experiences a $\mathbf{E} \times \mathbf{B}$ drift and no acceleration parallel to $\mathbf{E}$.

For the simulation shown in figure 1.4, the meaning of d_z can be interpreted simply as the extent of the system in the z direction. For a more collisional case, such as the environment generated in MAGPIE reconnection experiments, the meaning of d_z is less straight forward as the electrons will experience collisional friction against the ion population. The electrons will gain directed kinetic energy until collisional friction balances the force induced by the reconnecting electric field. When these two forces balance, the drift velocity of electrons with respect to ions, denoted v_d, is given by

$$m_i \frac{v_d}{\tau_{ei}} \sim ZeE, \tag{1.12}$$

where m_i is the ion mass; τ_{ei} is the electron-ion slowing down time; and Ze is the charge of

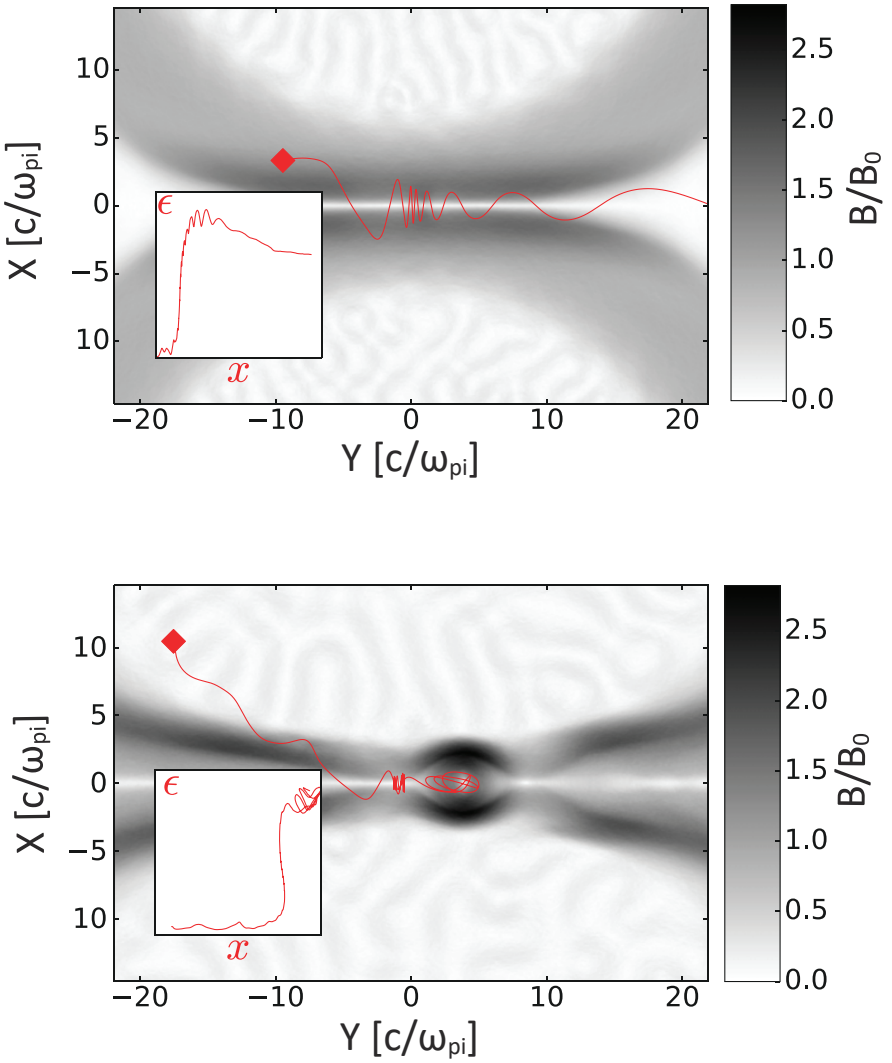

Figure 1.4: Data from particle in cell (PIC) simulations of a laser driven reconnection experiment showing the trajectory of test electrons. Particle trajectories are plotted in red, superimposed over the magnitude of the background magnetic field (plotted in grey). The red diamonds indicate the position of the test particles at $t = 0$, and the smaller plots on the bottom left of each plot show the energy of test particles as a function of X. *Above:* Electron undergoing direct acceleration by E_{rec}. *Below:* Electron undergoing Fermi acceleration in a plasmoid. Credit: [Totorica, 2017].

an ion. When this equilibrium is achieved, the energy gained from the reconnecting electric field goes to heating the plasma rather than increasing bulk velocity.

This is not quite the entire picture as it can be shown that the electron ion collision frequency (ν_{ei}) has a velocity dependence which goes as

$$\nu_{ei} \propto \left(\frac{1}{v_e}\right)^3, \tag{1.13}$$

where v_e is the electron velocity in the rest frame of the ions. This means that faster electrons experience fewer collisions. For a fraction of the fastest electrons, in the far wings of the velocity distribution, collisional friction is never sufficient to overcome the force from the electric field. These electrons are accelerated until they leave the system and are referred to as runaway electrons. It can be shown that the threshold velocity required for runaway (v_r) is given by

$$v_r = v_{Te}\sqrt{\frac{E_D}{E}}, \tag{1.14}$$

where v_{Te} is the electron thermal speed; E is the applied electric field; and E_D is called the Dreicer electric field. This is named after Harry Dreicer, who first formulated the theory for electron runaway [Dreicer, 1959]. The expression for the Dreicer electric field (in a high Z plasma) is

$$E_D = \frac{Ze\ln\Lambda}{4\pi\epsilon_0\lambda_D^2}, \tag{1.15}$$

here Z is the charge state of ions in the background plasma; $\ln\Lambda$ is the Coulomb logarithm; and λ_D is the Debye length. From equation 1.14 it follows that the density of runaway electrons (n_r) is approximated by

$$n_r \approx n_e \exp\left(-\frac{E_D}{2E}\right), \tag{1.16}$$

where n_e is the electron density in the background plasma.

An important side note is that all of the electron runaway results which were presented here are only valid in the limit $E_D >> E$. As the applied field strength approaches the value of the Dreicer electric field, the drift velocity of the thermal electrons (v_d in equation 1.12) approaches the electron thermal speed. As a result, the electrons become unstable to kinetic instabilities and Dreicer's theory ceases to be valid [Priest, 2000, p. 466].

Fermi Acceleration in Reconnection

Figure 1.4(b) shows results from a PIC simulation [Totorica, 2017] where an electron experiences Fermi acceleration in a plasmoid. The figure shows that the electron enters the plasmoid, where it undergoes a series of type-B Fermi reflections [Fermi, 1949] due to the field line curvature associated with the O-point structure. Because the plasmoid is continually accumulating reconnected flux as the electron bounces around within it, the

majority of these collisions will be 'head-on', and will therefore cause the electron to gain energy. It is interesting to observe that this particular application of the Fermi acceleration mechanism is not stochastic [Totorica, 2017]: The nature of the reconnection geometry means that most collisions are head-on and that they occur at regular intervals rather than at random. This means we might expect Fermi acceleration to be more efficient here than it is in diffusive shock acceleration.

Comment: Should there be an explanation of what a type B Fermi process is here?

The observation that electrons could be accelerated by plasmoids in this manor was first proposed in [Drake, 2006]. It is still not clear weather this mechanism is more important than direct electron acceleration by reconnecting electric fields. Results from PIC simulations suggest that more particles are accelerated by Fermi acceleration in plasmoids than by the reconnecting electric field, simply because the spatial scale of plasmoids is larger than that of X-lines so more particles encounter them [Dahlin, 2015]. But it seems to also be the case that the most energetic electrons are accelerated by the reconnecting electric field [Totorica, 2017]. It has been suggested that the relative importance of the two mechanisms might depend on the presence of a guide field (magnetic field perpendicular to the reconnection plane) – perhaps because this changes the properties of electron transport [Dahlin, 2015]. The role of collisions in plasmoidal electron acceleration is still very much an open question and to my knowledge all of published work in this area has assumed collisionless conditions.

1.2 Laboratory Reconnection Experiments

Several prevalent frameworks for studying reconnection in the laboratory have been developed over the last ~ 20 years. These experimental campaigns are motivated by a desire to understand the fundamental plasma precesses which drive reconnection.

One framework commonly used to study reconnection are purpose built plasma discharge chambers, typified by the Princeton Plasma Laboratory's Magnetic Reconnection eXperiment (MRX) [Yamada, 1997]. The MRX apparatus is effectively a large (~ 2 m radius) vacuum vessel containing a configuration of magnetic field coils, and filled with a working gas (typically hydrogen). A rapidly varying magnetic field is driven through the vessel by the coils, inducing a strong electric field which ionises the gas to form a plasma. The configuration of magnetic field in the vessel can be varied as a function of time – setting the plasma dynamics and driving magnetic reconnection. The flows which are created using this framework are have a low plasma β (are weakly driven), and are long lasting ($\sim 50\,\mu$s). Plasma flows are typically diagnosed using in situ Langmuir and magnetic probes. The generation of fast particles is not measured. Notable findings from MRX data include

an appreciation of the importance of two fluid physics and the hall effect in collisionless reconnection [Zweibel, 2009; Zweibel, 2016].

Another common method of generating a reconnecting plasma is to create two colliding, high energy density, plasma flows with a high powered laser system. These flows are either externally magnetised using field coils [Fiksel, 2014], or are designed to self magnetise via the Biermann battery mechanism [Nilson, 2006]. The dynamics generated in laser driven experiments are very strongly driven (high plasma β), and short lived ($\sim 500\,\mathrm{ps}$). The primary way of diagnosing the thermal bulk of the plasma is typically via proton radiography [Borghesi, 2001].

Diagnosing fast particle production in laser driven reconnection experiments is an area of current interest, but there are still relatively few papers available on the topic. Some work has been done on simulating fast particle production, which is being used to plan future experimental campaigns (for example [Totorica, 2017]). An experimental paper claiming to have measured particle acceleration was released several years ago [Zhong, 2010], but more recent work (e.g. [Raymond, 2016]) is exiting in the sense that these experiments are more cleanly diagnosed.

Comment: Should perhaps mention that the Raymond result is on a short pulse laser – so very different conditions to us.

The results presented here used a third, pulsed power driven experimental platform to generate reconnecting plasma flows [Suttle, 2016; Hare, 2017b; Hare, 2017a]. This platform was developed using Imperial College's MAGPIE current generator. It is capable of generating relatively long lasting plasma flows ($\sim 500\,\mathrm{ns}$), and experiments are relatively weakly driven ($\beta \sim 1 - 10$). At present, the work published using this framework has focussed on describing the dynamics of plasma flows in reconnection. The generation of fast particles has not been discussed.

Comment: Should extend this section, perhaps include a picture of the MAGPIE setup, include some key results.

1.3 Emission Processes in High Energy Density Plasma Physics

In the following discussion spectrally resolved quantities will be parametrised in terms of photon energy (ε). This can be related to wavelength (λ) via Planck's relation:

$$\varepsilon = \frac{hc}{\lambda}, \tag{1.17}$$

where h is Planck's constant, and c is the speed of light. This equation can be restated as

$$\varepsilon\ [\mathrm{eV}] = \frac{1.2398 \times 10^4}{\lambda\ [\mathrm{\AA}]}, \tag{1.18}$$

where the units are chosen to be convenient for experimental work.

A detailed discussion of the different techniques which are commonly employed to model the emission from laboratory plasmas is well beyond the scope of this thesis. In essence, in order to make predictions about the spectral emission from a plasma, it is usually necessary to use some model in order to estimate the population of the atomic states of the system. One way to do this is to assume the plasma is in local thermodynamic equilibrium (LTE). This means that the velocity distribution of plasma particles is Maxwellian; the energy distribution of the radiation field is Planckian; and the population of the atomic states of the system are dictated by the Saha equation, and furthermore that these different degrees of freedom have the same characteristic temperature. In order for this to be a valid assumption, the plasma has to be opaque across all photon energies. This ensures that, when a photon is emitted, it does not travel a long way (or escape the system) before it interacts with the plasma again.

A more appropriate model to use in optically thin plasma is a so called non local thermodynamic equilibrium (nLTE) treatment. This requires that a set of coupled rate equations are solved in parallel. These equations describe how the various atomic states of the system are connected by a variety of different atomic processes. They are solved with plasma density and electron temperature specified as independent variables.

Comment: This was all written from memory. It obviously needs referencing. I'm also worried it might sound a little naive.

Figure 1.5 shows an example of a data obtained using the nLTE atomic code PrismSPECT. The simulation was run with an electron temperature of 100 eV and an ion number density of $1 \times 10^{17}\,\mathrm{cm}^{-3}$. The spectrum seen in the plot is relativity complex, and three different emission processes contribute to the total spectrum. The first of these produces emission lines at discrete energies, due to electrons transitioning from one bound atomic

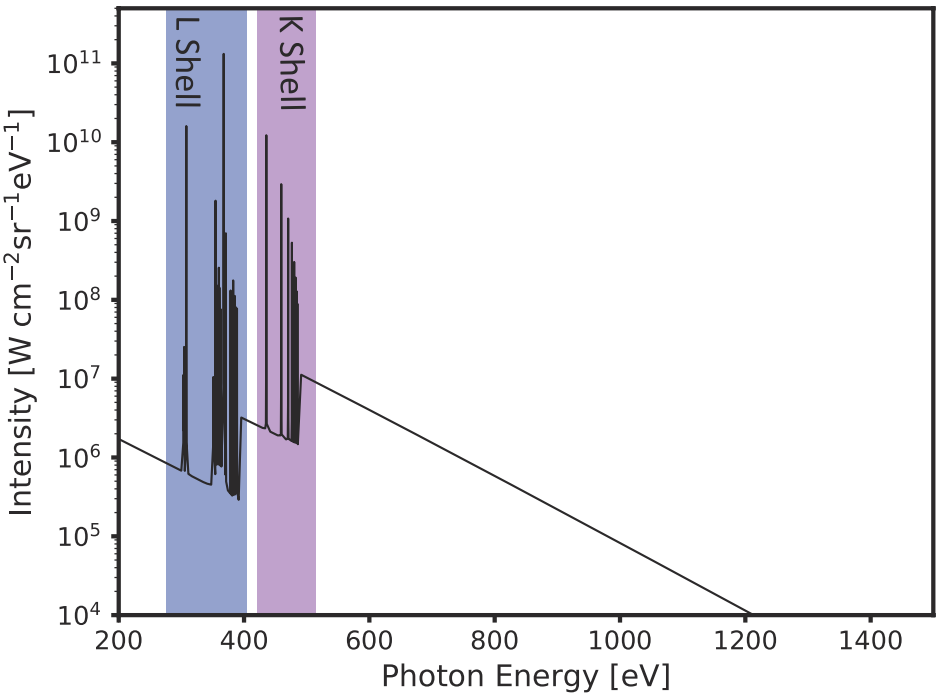

Figure 1.5: An example of a simulated spectrum produced using the atomic code PrismSpect. The results show the predicted emission from a carbon plasma with an electron temperature of 100 eV and an ion density of $1 \times 10^{17}\,\mathrm{cm}^{-3}$. The positions of Carbon K and L shell emission lines are also indicated.

state to another bound state. For this reason, these are referred to as bound-bound emission features. The second process which contributes to the spectrum is radiative recombination. This occurs when a free electron recombines with an ion. It is called free-bound emission. The third process which contributes is emission which occurs when a free electron scatters off an ion. This is called free-free or Bremsstrahlung emission. Figure 1.6 shows the relative contribution of these three emission possesses to the total spectrum shown in figure 1.5. As can be seen, free-free and free-bound are continuum emission processes. For the work presented in this thesis, measurements of the continuum represent the majority of experimental results, and so the discussion in this section is limited to emission from Bremsstrahlung and radiative recombination.

1.3.1 Bremsstrahlung

A well known result from classical electrodynamics is that a free electron, moving in the electric field of a positive ion, will emit radiation. In the process this electron looses some fraction of its kinetic energy, causing it to slow down. This is known as *Bremsstrahlung*, which derives from the German words *bremsen* (to break) and *Strahlung* (radiation). The equation describing the this process is

$$e^-(\varepsilon_e) + A^{(Z)} \rightleftharpoons A^{(Z)} + e^-(\varepsilon_e') + \gamma(\varepsilon_\gamma), \tag{1.19}$$

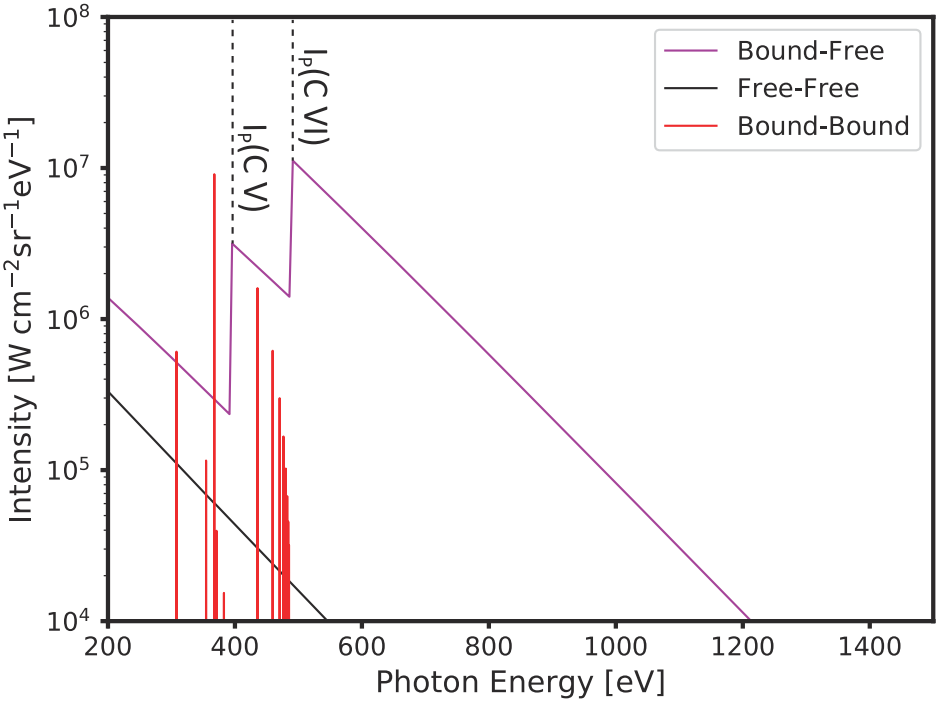

Figure 1.6: An illustration of the various emission processes which contribute to the spectrum shown in figure 1.5. The position of the Carbon V and Carbon VI ionisation potentials, denoted I_P(C V) and I_P(C VI), are also indicated.

where e^- represents a free electron; $A^{(Z)}$ represents a positive ion of charge Ze; γ represents an emitted photon; ε_e is the initial energy of the electron; ε'_e is the final energy of the electron; and ε_γ is the energy of the emitted photon. The scattering process is elastic and so the relation

$$\varepsilon_e - \varepsilon'_e = \varepsilon_\gamma \tag{1.20}$$

is implied by energy conservation.

In a plasma with electrons distributed according to the velocity distribution $f_e(v)$, the contribution to total Bremsstrahlung emission from electrons with velocities in the interval v to $v + dv$ is given by the equation

$$P_{\varepsilon,v}\, dvd\varepsilon = \sum_\alpha n_{i,\alpha} n_e f_e(v) \varepsilon\, d\sigma_{ff}(v,\varepsilon)\, dv, \qquad \text{[Power/Volume]} \tag{1.21}$$

where v is electron velocity; ε is photon energy; α indexes ion species; $n_{i,\alpha}$ is the density of a given ion species; n_e is free electron density; and $\sigma_{ff}(v,\varepsilon)$ is the cross section for Bremsstrahlung (free-free) emission. The photon energy resolved total Bremsstrahlung spectrum is obtained by computing

$$P_\varepsilon\, d\varepsilon = \int_{v_{min}}^{\infty} P_{\varepsilon,v}\, dvd\varepsilon. \tag{1.22}$$

Here v_{min} is the minimum velocity of an electron which is capable of emitting a photon with energy ε, and so $\frac{1}{2}m_e v_{min}^2 = \varepsilon$, where m_e is the electron mass.

A common way to parametrise the Bremsstrahlung emission spectrum for a Maxwellian electron population (with a temperature T_e) is

$$P_\varepsilon \, d\varepsilon = \frac{32\pi}{3}\sqrt{\frac{2\pi}{3k_B T_e m_e}}\left(\frac{e^2}{4\pi\epsilon_0}\right)^3 \frac{n_e}{h m_e c^3}\left(\sum_\alpha Z_\alpha^2 n_{i,\alpha}\right)\exp\left(-\frac{\varepsilon}{k_B T_e}\right)\overline{g}_{ff}\, d\varepsilon, \quad (1.23)$$

where k_B is Boltzmann's constant; e is the electronic charge; ϵ_0 is the permittivity of free space; and Z_α is the degree of ionisation for the species α. The factor $\overline{g}_{ff}$ is called the free-free Gaunt factor. If the result for the single electron emission spectrum from classical electrodynamics is used and the interaction between electrons and ions is assumed to be described by Coulomb scattering, then $\overline{g}_{ff} = 1$. The correction obtained from a quantum mechanical treatment of the interaction is a function of temperature and density, but usually is negligible.

For a quasi-neutral plasma, with a single ion species, taking $\overline{g}_{ff} = 1$ reduces equation 1.23 to

$$P_\varepsilon(T_e, n_e, Z)\ \left[\frac{\mathrm{W}}{\mathrm{cm^3\,eV}}\right] = 1.1\times10^{-32}\frac{\left(n_e\ [\mathrm{cm^{-3}}]\right)^2 Z}{\sqrt{T_e\ [\mathrm{eV}]}}\exp\left(-\frac{\varepsilon\ [\mathrm{eV}]}{T_e\ [\mathrm{eV}]}\right). \quad (1.24)$$

A key feature to note is that the only dependence on photon energy is in the $\exp(-\varepsilon/T_e)$ factor in the equation. Determining the slope on the emission spectrum is therefore a common way to measure electron temperature.

The characteristic exponential shape of the Bremsstrahlung spectrum is shown in the black trace of figure 1.6.

1.3.2 Radiative Recombination

Radiative recombination describes a process in which a free electron is captured by a positive ion, releasing a photon in the process. This process, and its inverse (which is referred to as photoionisation), are described by the equation

$$A^{(Z)} + e^-(\varepsilon_e) \rightleftharpoons A^{(Z+1)} + \gamma(\varepsilon_\gamma), \quad (1.25)$$

where the various symbols retain the meaning that they had in the equivalent equation for Bremsstrahlung emission. Energy conservation implies that

$$\varepsilon_e + I_P = \varepsilon_\gamma, \quad (1.26)$$

where I_p is the ionisation potential of the state occupied by the electron after it is captured.

By following a similar process to the one described for Bremsstrahlung , it can be shown that the radiative recombination emission spectrum, for a plasma with a thermal electron

velocity distribution, is proportional to

$$P_\varepsilon \propto \begin{cases} 0 & \varepsilon < I_P, \\ n_{A(Z)} n_e \frac{\varepsilon^3 \sigma_{PI}(\varepsilon)}{(k_B T_e)^{\frac{3}{2}}} \exp\left(\frac{I_P - \varepsilon}{k_B T_e}\right) & \varepsilon > I_P. \end{cases} \tag{1.27}$$

Here, $\sigma_{PI}(\varepsilon)$ is the cross section for photoionisation; and $n_{A(Z)}$ is the number density of ions with charge Ze. For photon energies which are far from I_P, the cross section is proportional to $1/\varepsilon^3$, and so dependence on photon energy goes as

$$\exp\left(\frac{I_P - \varepsilon}{k_B T_e}\right). \tag{1.28}$$

This means that the slope of a recombination feature can be used as a temperature diagnostic, in the same way as is true for Bremsstrahlung emission.

The characteristic saw-tooth like emission spectrum which is emitted as a result of recombination to different ion charge states is shown in the magenta trace of figure 1.6. The slope of the recombination continua are all parallel to the slope on the Bremsstrahlung continuum curve. This is characteristic of the fact that all of the slopes are set by electron temperature.

2 The MAGPIE Generator and Diagnostic Suite

In this chapter I discuss the MAGPIE generator which was used to drive the experiments I present later in this thesis, and the suite of diagnostics which were used to measure plasma conditions in the experiments. Diagnosing pulsed power driven plasma physics experiments is challenging. One reason for this is because the dynamics of these experiments are very short ($1 - 100\,\mathrm{ns}$). Another area of difficulty is the fact that the operation of a pulsed power generator creates a fairly harsh environment, in that it produces strong EMP, intense radiation and mechanical debris.

In the last few years, experiments on MAGPIE have been diagnosed primarily with a variety of laser probing diagnostics. During the course of my PhD, I have added to these with a variety of X-Ray imaging diagnostics. The discussion presented here begins by discussing the MAGPIE generator; then various laser probing diagnostics are described; and, in the final two sections, the X-Ray/XUV diagnostic capability is outlined.

2.1 The MAGPIE Generator

MAGPIE is a Mega-Ampere class pulsed power generator, run by the plasma physics group at Imperial College. The facility was commissioned in the 1990s and was originally designed to study the radiative collapse of deuterium fibres. This was a fusion energy concept at the time. A drawing of the facility is shown in figure 2.1. A key thing to take from this diagram is that MAGPIE is a large, complex machine. It is run and maintained entirely by PhD students and research staff. A significant fraction of my PhD was spent repairing and upgrading various aspects of the facility. The design of the generator were first presented in [Mitchell, 1996] and has subsequently been well described in a number of previous students' theses (for example [Swadling, 2011; Burdiak, 2012]). The overview of the machine which I give here is rather brief by comparison.

MAGPIE consists of four bipolar Marx generators which discharge into individual pulse forming lines (PFLs). These are coupled into a single vertical transmission line (VTL). The PFLs and VTL have a coaxial geometry, with deionised water used as the dielectric. The output to the VTL couples into a vacuum section called the magnetically insulated transmission line (MITL). The transition from the, water filled, lines to the vacuum employs an arrangement known as a diode stack in order to avoid breakdown at the interface. The

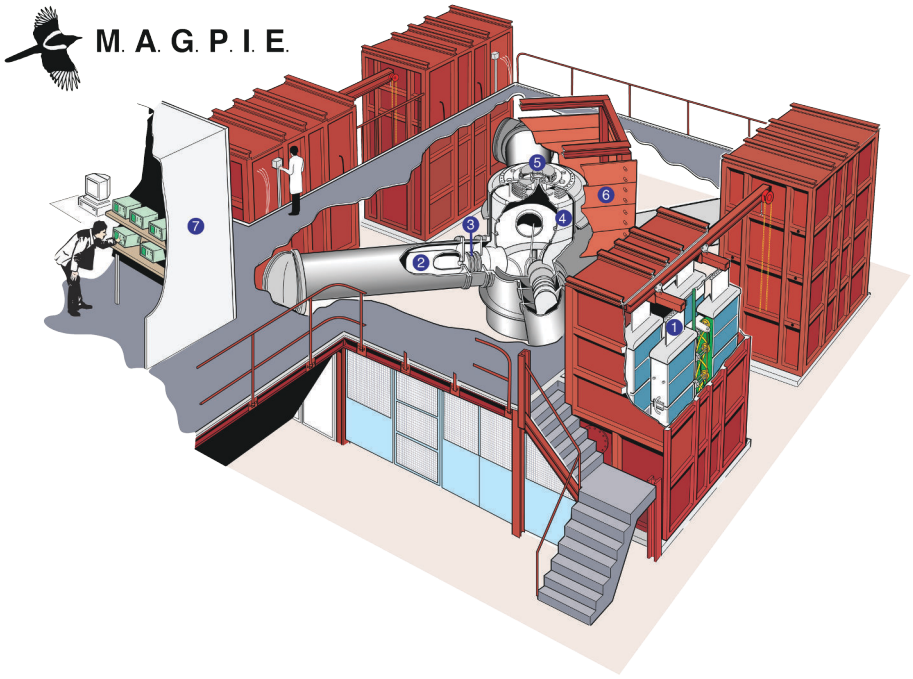

Figure 2.1: A diagram of the MAGPIE generator. *(1):* Marx bank generators. *(2):* Pulse forming lines. *(3):* Trigatron switches. *(4):* Vertical transmission line. *(5):* Diode stack and MITL (magnetically insulated transmission line). *(6):* X-Ray Shielding (or "the iron curtain"). *(7):* Data acquisition room.

MITL is conically shaped to reduce the diameter of the inner conductor from $\sim 1.5\,\mathrm{m}$ at its input (from the VTL) , to $\sim 1\,\mathrm{cm}$ at its output (to the load).

The Marx generators consist of an arrangement of capacitors which are charged in parallel over the course of several minutes and then discharged in series over a timescale on the order of $1\,\mu\mathrm{s}$. The Marxs used on MAGPIE consist of 24 individual capacitors, each with a capacitance of $1.3\,\mu\mathrm{F}$. These are charged to $\pm 65\,\mathrm{kV}$ in parallel. This corresponds to a potential of $\pm 1.5\,\mathrm{MV}$ in the series configuration. The total energy stored in each Marx generator is $66\,\mathrm{kJ}$ and the discharge time is $0.89\,\mu\mathrm{s}$.

The Marxs discharge into the capacitance of the PFLs. The function of the PFLs is to temporally compress the length of the overall voltage pulse produced by MAGPIE. The individual lines act as intermediate voltage storage (between the Marxs and the load section). The discharge of the PFLs is initiated by the simultaneous closure of four 'Trigatron' gas switches. Closing these switches causes a voltage pulse to propagate along each PFL, and MAGPIE's total drive time is largely a function of the transit time for this voltage pulse.

The four lines discharge into the VTL and, at the interface, the geometry of the transmission lines swaps from a 'horizontal' design to a 'vertical' one. This means the axis of the VTL is perpendicular to the floor of the laboratory (whereas the PFLs are parallel to the floor). A vertical geometry is more convenient for load design and diagnostic access.

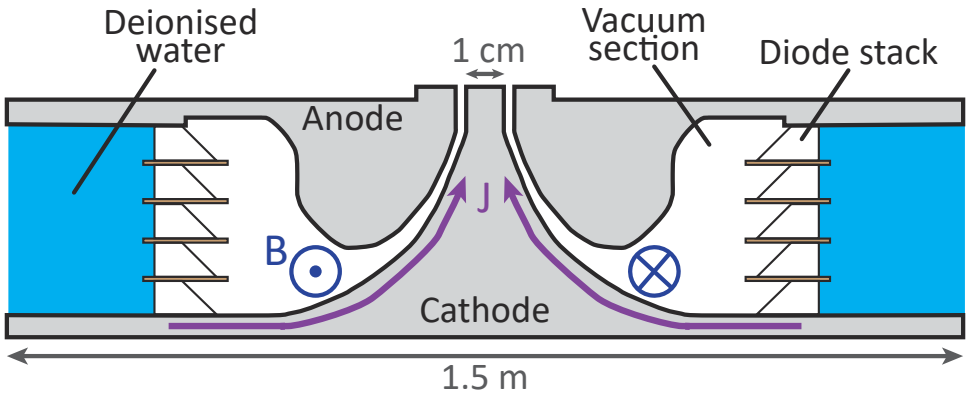

Figure 2.2: A diagram of the diode stack and magnetically insulated transmission line (MITL). The direction of current flow through the cathode is labelled J. The magnetic field induced by current flow through the cathode is labelled B.

2.1.1 Magnetic Insulation

A diagram of the final section of the generator (the MITL) is shown in figure 2.2. The function of this section of the generator is two fold. Firstly it serves as a transition from water filled transmission lines, to a vacuum section. Secondly it reduces the diameter of the inner conductor in order to concentrate the power delivered by the generator to the spatial scale of the load. Transmitting very high voltages through a vacuum is problematic because the strength of the electric field on the surface of the cathode is strong enough to rip electrons from the conductor. These electrons accelerate across the gap, causing the transmission line to breakdown. This can be overcome through the use of magnetic insulation. The magnetic field induced by the flow of current through a coaxial vacuum line causes the emitted electrons to gyrate. A line is said to be magnetically insulated when the induced magnetic field is large enough for the cyclotron orbit of electrons to be less than the vacuum gap. When this criteria is met, the emitted electrons are unable to cross the cap. The geometry of the MITL is designed to ensure that this criteria is met, along its entire length, until the very late into the generator's current pulse.

In addition to the MITL, figure 2.2 shows the diode stack at the boundary between air and water in the machine. The stack consists of concentric rings which alternate between being made of metal and plastic. These serve tp shape the electric field along the axis of the stack in order to prevent the failure of the generator due to avalanche breakdown along its surface.

2.1.2 The MAGPIE Current Pulse

The current pulse produced by MAGPIE is well approximated by a function of the form

$$J(t) = J_p \sin^2\left(\frac{\pi(t-t_0)}{2\tau_r}\right), \tag{2.1}$$

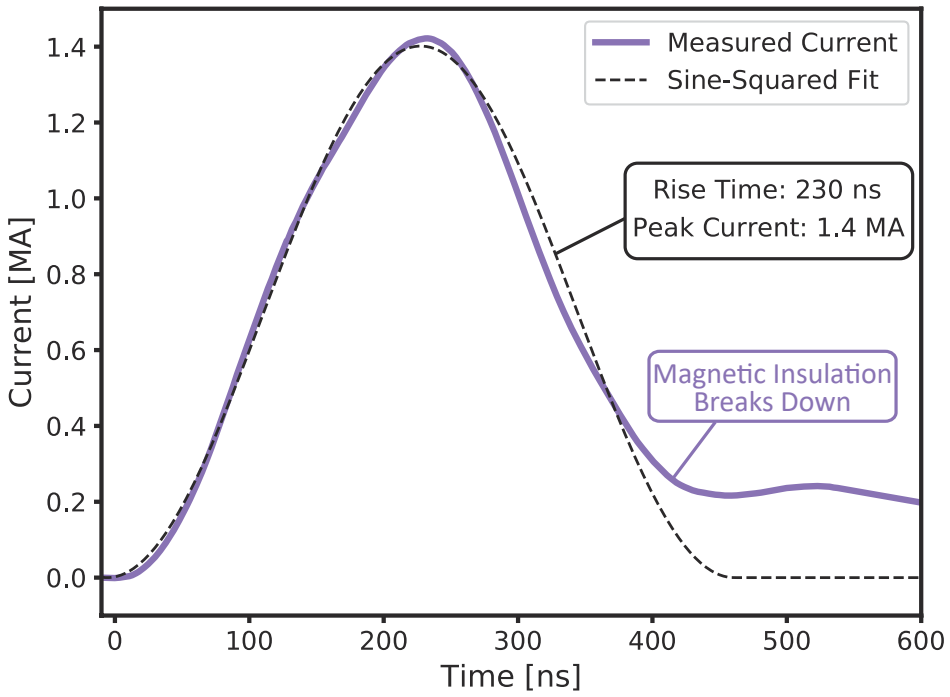

Figure 2.3: A typical current pulse achieved in a reconnection experiment on MAGPIE compared to a Sine-squared fit.

for values of t in the range $t_0 \leq t \leq (2\tau_r + t_0)$, and $J(t) = 0$ otherwise. Here, J_p is the peak current; τ_r is the generator's rise time; and t_0 is the current start time.

Figure 2.3 shows an experimentally measured current pulse with this fit applied to it. The fit parameters obtained were $J_p = 1.4\,\mathrm{MA}$ and $\tau_r = 230\,\mathrm{ns}$.

One thing to note in the figure is that at late time the current pulse deviates from the sine-squared fit. This is something which is usually attributed to the break down of the magnetic insulation at late times, either in the MITL or the experimental load. That said, issues such as this fall broadly under the umbrella of what is called 'power flow' in the field of pulsed power science. Obtaining a detailed understanding of the power flow problem is still very much an area of research which is in its infancy.

An unusual aspect of MAGPIE when compared to most pulse power generators is the fact that it a relatively high impedance generator. This is an artefact of the fact that the deuterium fibres the machine was designed to drive were an exceptionally inductive load. Practically this means that MAGPIE is a very flexible machine – the shape of the current pulse does not change dramatically as a function of load impedance. It also allows for exceptional diagnostic access.

2.1.3 Rogowski Probes

The current pulse delivered to the load fielded on a pulsed power generator is an important quantity to diagnose because it acts as an indication of the power delivered to the experi-

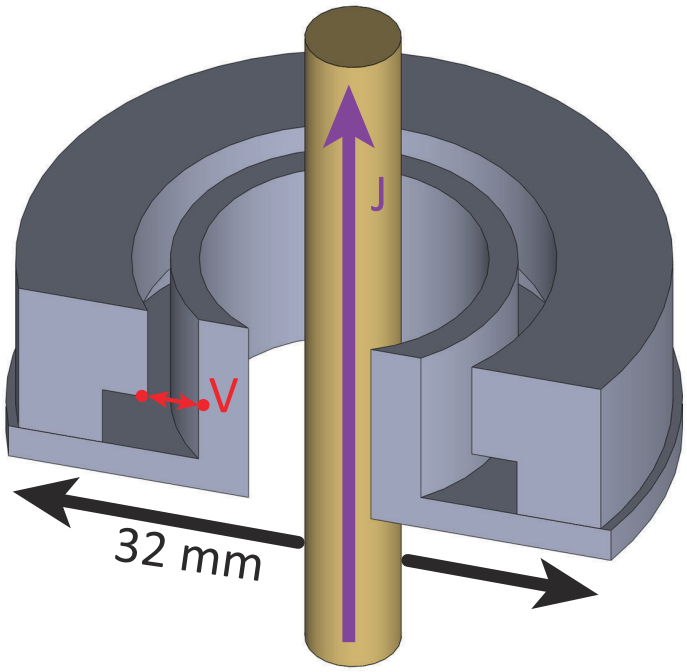

Figure 2.4: A three dimensional render of a Rogowski probe used for experiments on MAGPIE is drawn in grey, with a current carrying rod drawn in gold. The direction of current flow is shown in purple, and the point across which probe voltage is measured is shown in red.

ment during the course of a current pulse. In order to measure this quantity experiments on MAGPIE use a form of probe known as a single turn Rogowski coil. Figure 2.4 is a three dimensional render of a Rogowski coil used on MAGPIE. It consists of a concentric conductor through which a groove is cut. A time varying current induces a voltage across this groove. This voltage is recorded using an oscilloscope and can be used to recover the current pulse.

Figure 2.5 is a schematic digram illustrating the operating principle behind a Rogowski coil. The black outline in the diagram is a cross section of the lower part of the probe across which a voltage is measured. The diagram shows an off-axis current carrying rod. However, in the first instance, I will assume that the rod is centred on the axis and so the magnetic field induced a distance r from the axis of symmetry is given by

$$B_\phi(r,t) = \frac{\mu_0 J(t)}{2\pi r}, \tag{2.2}$$

where $J(t)$ is the current carried by the rod, and all other symbols have their usual meaning[1].

By the application of Faraday's law, the time derivative of the current is related to the

[1] Formally this statement is only true in a magneto-static case, however the fastest timescale of interest for experiments is $\sim 1\,\text{ns}$. By contrast, the propagation time for electromagnetic fluctuations goes as $10\,\text{mm}/c \sim 10\,\text{ps} << 1\,\text{ns}$, and so the static solution is valid.

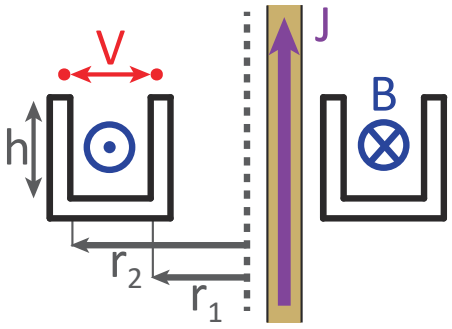

Figure 2.5: A diagrams to illustrate the operating principle behind a single turn Rogowski coil. In the diagram, current flow is shown in purple; the induced electric field is shown in blue; and the measured voltage is shown in red. The black outline indicates a cross section through the volume of the probe.

voltage induced across the groove by the equation

$$\frac{dJ(t)}{dt} = \frac{2\pi V(t)}{\mu_0 h \ln(r_2/r_1)}, \tag{2.3}$$

where r_1, r_2, and h are the dimensions of the probe shown in figure 2.5. This result holds for slight deviations from axial symmetry since, on the nano-second timescale, the induced voltage is constant around the conductor's azimuth and so the variation arising from asymmetry is averaged out.

Rogowski Probes Used on MAGPIE

As shown in figure 2.4, the Rogowski probes used for experiments on MAGPIE are manufactured with a groove of variable width. The thinner section of the groove is used to locate the conductor which relays the voltage to a scope, whilst the thicker section of the groove provides most of the cross sectional area responsible for the induction of voltage . The calculation presented above can be adjusted to include the contribution from the thinner groove however this correction is negligible.

In reality, the probes are shielded by a plastic cover. This acts to prevent the probe from directly coupling to the voltage produced by the generator, and shields the probe from intense UV radiation which is produced by the experiments. In the absence of this shielding, UV emission from the plasma would produce photoelectrons and these would cause the probe to short circuit .

Experiments on MAGPIE typically use two Rogowski coils which are placed on return posts in the load hardware. Two coils are used to determine weather the return current is azimuthally symmetric. Combining of the two signals also allows one to verify that the probe measurements is not adversely effected by capacitive pickup: Assuming the probes

are oppositely oriented, one can calculate the quantity

$$V_{combined}(t) = \frac{V_+(t) - V_-(t)}{2}, \tag{2.4}$$

where $V_+(t)$ and $V_-(t)$ are the signals from the two probes. Since the contribution from capacitive coupling will have the same sign for both orientations of probe, whilst the inductive voltages will have the opposite signs, this procedure eliminates the capacitive contribution.

For reference, the standard Rogowski probes used for MAGPIE experiments have the dimensions $r_1 = 9\,\text{mm}$, $r_2 = 13\,\text{mm}$, and $h = 3.5\,\text{mm}$. Appling these values to equation 2.3 and integrating yields the result

$$J(t) = 3.9 \times 10^{-6} \left[\frac{\text{MA}}{\text{nsV}}\right] \int_0^t V(t')dt'. \tag{2.5}$$

Typically the voltage integration process is performed numerically as a post processing step (rather than using a passive electrical integrator).

2.2 Laser Probing Diagnostics

A variety of different plasma properties can be inferred via the use of laser probing diagnostics. This is a good way to measure plasma conditions primarily because lasers are monochromatic and can produce sub nanosecond pulses of radiation. Their monochromatic nature is useful because it means they are able to overcome self emission from the plasma in a spectrally localised region without carrying enough energy to perturb the background plasma. Short pulse lengths are beneficial since they provide a means to time-gate experimental measurements.

2.2.1 Electromagnetic waves in a plasma

To describe the operation of laser probing diagnostics , it is instructive to consider the nature of electromagnetic waves in a plasma. Begin by considering

$$\partial_t \mathbf{B} = -\nabla \times \mathbf{E}, \tag{2.6}$$

and Ampere's law

$$\nabla \times \mathbf{B} = \mu_0 \mathbf{j} + \frac{1}{c^2}\partial_t \mathbf{E}, \tag{2.7}$$

where $\mathbf{B}$ is magnetic field; $\mathbf{E}$ is electric field; μ_0 is the vacuum permeability; $\mathbf{j}$ is current density; and c is the speed of light in a vacuum. Differentiating equation 2.6 with respect to time, and applying the identity

$$\nabla \times (\nabla \times \mathbf{A}) = \nabla \cdot \mathbf{A} - \nabla^2 \mathbf{A}, \tag{2.8}$$

yields the wave equation

$$\nabla^2\mathbf{E} - \nabla\cdot\mathbf{E} = \mu_0\partial_t\mathbf{j} + \frac{1}{c^2}\partial_t^2\mathbf{E}. \tag{2.9}$$

Consider the propagation of a plane wave polarized in the $\hat{\mathbf{x}}$ direction and moving in the $\hat{\mathbf{z}}$ direction, which is described by

$$\mathbf{E} = E_x \exp[i(kz - \omega t)]\hat{\mathbf{x}}. \tag{2.10}$$

Substituting equation 2.10 into 2.9 and differentiating produces the result

$$-k^2E_x = \mu_0\partial_t j_x - \left(\frac{\omega}{c}\right)^2 E_x. \tag{2.11}$$

If we take into account that the medium through which the wave is propagating is a plasma and it is assumed that ω is much larger than the frequencies associated with thermal fluctuations; particle collisions; and magnetic gyromotion, then the current which is induced in the plasma by the wave is given by

$$j_x = en_e(Zu_{i,x} - u_{e,x}), \tag{2.12}$$

where ne is electron density; Z is the average level of ionisation; u_i is the induced ion velocity; and u_e is the induced electron velocity. The equations of motion for electrons and ions moving under the influence of E_x are

$$m_e\partial_t u_{e,x} = -eE_x, \tag{2.13}$$

$$m_i\partial_t u_{i,x} = eZE_x. \tag{2.14}$$

Substituting these into equation 2.11 gives the result

$$\omega^2 = \mu_0 e^2 n_e c^2\left(\frac{Z^2}{m_i} + \frac{1}{m_e}\right) + k^2c^2, \tag{2.15}$$

and, since $m_i/Z^2 >> m_e$, this is reduces to the dispersion equation

$$\omega^2 = \frac{\mu_0 e^2 n_e c^2}{m_e} + k^2c^2 = \omega_{p,e}^2 + k^2c^2, \tag{2.16}$$

where $\omega_{p,e}$ is the electron plasma frequency. A plot of the form of this dispersion function is shown in figure 2.6, plotted against the vacuum E-M wave dispersion function. Two features are immediately obvious from this plot:

- Electromagnetic waves with a frequency below ω_p will not propagate through the medium
- The phase-speed of an electromagnetic wave propagating through a plasma is always

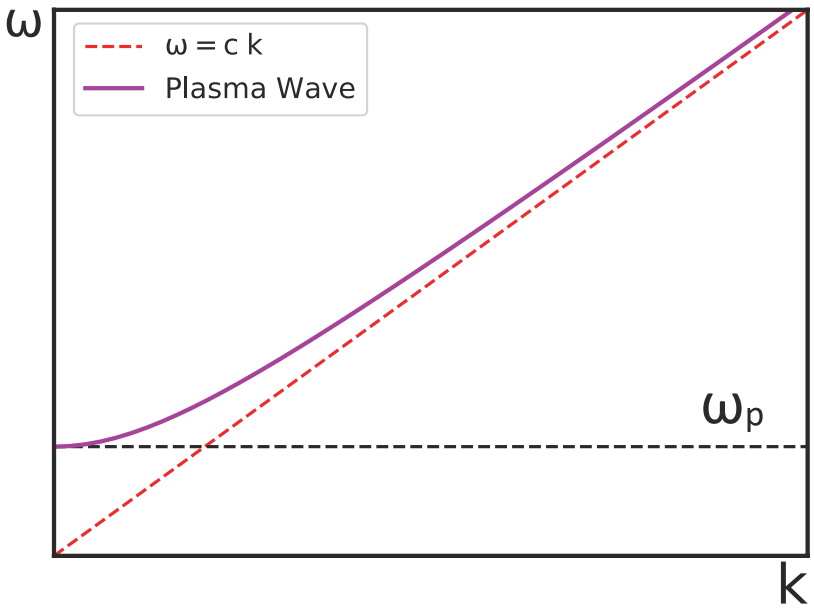

Figure 2.6: A plot of the dispersion function specified by equation 2.16.

larger than c

The second feature implies that the refractive index of a plasma is negative.

2.2.2 Laser Interferometry

Imaging interferometry provides a means to make spatially resolved measurements of line integrated electron density. The technique has been employed widely in the context of HEDP experiments on both high powered laser[Howard, 2018; Patankar, 2015] and pulsed power [Banasek, 2018; Swadling, 2014] facilities. The basic principle underlying the diagnostic is that a measurement of the additional phase applied to a laser probe by the plasma is measured, and this phase offset is proportional to the line integrated electron density along the path of the probing laser.

This follows from the fact that the phase obtained by a plane wave as it travels through a plasma is given by

$$\theta_p = \int \mathbf{k} \cdot d\mathbf{l}, \tag{2.17}$$

and, from equation 2.16, this is equal to

$$\theta_p = \int \sqrt{\frac{\omega^2 - \omega_p^2}{c^2}} dz \approx \int \frac{\omega}{c} \left(1 - \frac{\omega_p^2}{2\omega^2}\right) dz, \tag{2.18}$$

where the approximate result follows from a Taylor expansion of the integrand in $(\omega_p/\omega)^2$,

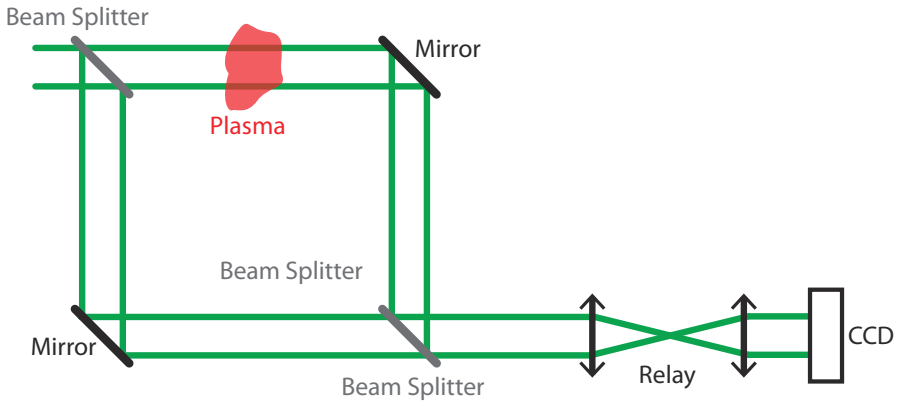

Figure 2.7: A Diagram of an imaging Mach-Zander interferometer.

and so assumes that $\omega >> \omega_p$.

The difference in phase between a wave which has passed through the plasma, and one which has propagated over the same length in a vacuum is given by

$$\Delta\theta = \theta_p - \int \frac{\omega}{c} dz = -\int \frac{\omega_p^2}{2c\omega} dz = -\frac{e^2\lambda}{4\pi c^2 \epsilon_0 m_e} \int n_e dz. \tag{2.19}$$

So by measuring the difference in phase between a laser beam travelling through the vacuum and a beam passing through the plasma, it is possible to infer the line integrated electron density.

The interferometric diagnostics fielded on MAGPIE typically use an imaging Mach-Zander configuration, which is shown in figure 2.7. This setup involves splitting a laser beam into two 'arms', a probe and a reference. The probe is passed through the plasma and the reference is propagated over a similar length in air. Both beams are collimated as they propagate. The two beams are re-combined and a two lens relay is employed to image the object onto a CCD camera.

A slight misalignment between the probe and reference beams is introduced and so, in the absence a plasma object, the instrument produces a linear fringe pattern. The maxima and minima in this pattern can be interpreted as contours in the phase of the probe beam. By comparing an interferogram captured during an experiment with a background interferogram, captured immediately before the experiment, it is possible to infer the additional phase shift applied to the probe by the plasma.

An illustration of this process is given in figure 2.8. The top left image shows a grey-scale interferogram which was obtained just before an experiment on MAGPIE, and the top right image shows the interferogram obtained with the same diagnostic during an experiment. Raw interferograms are processed by (manually) tracing the fridge minima and maxima, then interpolating to produce a phase map. The red lines on the raw interferograms indicate the position of traced fringes, and the lower two panels in the plot show the interpolated

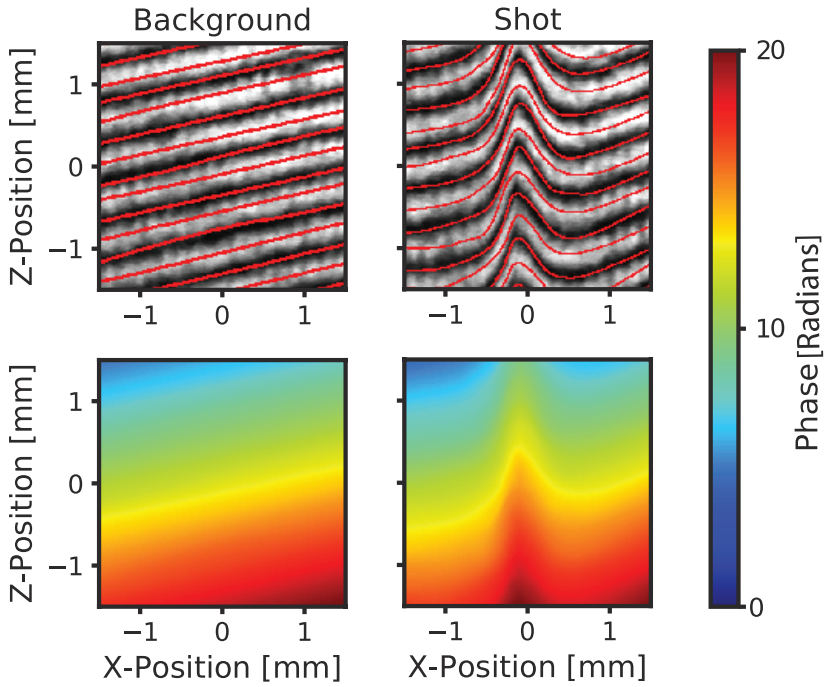

Figure 2.8: Plots showing the data analysis process which is used to obtain electron density maps from raw interferograms. The top two panels are raw interferometry data, with fitted fringe maxima and minima indicated in red. The lower two panels show phase maps which are produced by interpolating between the traced fringes.

phase map. Details of the interpolation process are beyond the scope of this thesis but the method is well described in [Hare, 2019].

By subtracting the background phase map from the one obtained during the experiment one can obtain a spatially resolved map of $\Delta\theta$ and this can be applied to equation 2.19 to obtain a map of line integrated electron density. The electron density map obtained from the raw data discussed previously is shown in figure 2.9.

Implementation of interferometry in MAGPIE experiments

Experiments on MAGPIE use a pulsed solid state lasers as probes for interferometry. Probe beams with wavelengths of 1053 nm, 532 nm, and 355 nm are available. These all have a pulse length of less than 1 ns and time gating is provided by the laser pulse – CCD shutters are held open for the duration of the experiment. There is typically no need for laser energies to surpass ~ 200 mJ, as this energy is sufficient to overpower self emission from the plasma during the course of the experiment. Laser line filters are used to cut self emission far from the probe wavelength from captured images. Commercial CCD cameras are used as these are more robust and have a larger sensitive area than scientific CCDs. Our current preferred model is the Cannon EOS 500D, which can be relatively easily modified in order to make them sensitive to UV and IR light.

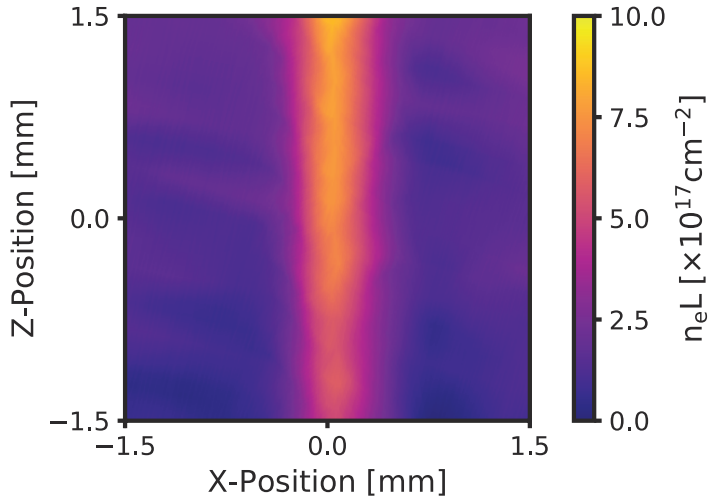

Figure 2.9: An electron density map produced using the data shown in figure 2.8.

2.2.3 Faraday Rotation Imaging

The dispersion relation derived in section 2.2.1 was not exact in the sense that it ignored the anisotropy introduced by the magnetic field in a plasma. A full three-dimensional treatment, taking into account the effects of magnetic anisotropy is presented in [Hutchinson, 2002, p. 104]. This shows that the presence of a magnetic field acts to rotate the polarization of an initially linearly polarized electromagnetic wave by an angle α, which is known as the Faraday Effect. Provided the frequency of the wave (ω) is much larger than the electron gyrofrequency (Ω_e) and the plasma frequency (ω_p), the rotation angle is given by

$$\alpha[\text{deg}] = \frac{e^3\lambda^2}{8\pi^2\epsilon_0 m_e^2 c^3}\int n_e \mathbf{B}\cdot d\mathbf{l}, \tag{2.20}$$

where the line integral runs along the path followed by the wave [Swadling, 2014]. A rough estimate of the value of α which might be obtained in an experiment is given by

$$\alpha[\text{deg}] \sim 2.62\times 10^{-24}\,(\lambda[\text{nm}])^2 \times \bar{n_e}[\text{cm}^{-3}] \times \bar{B}[\text{T}] \times L[\text{cm}], \tag{2.21}$$

where $\bar{n_e}$ represents average electron density; $\bar{B}$ is the average strength of the magnetic field parallel to the probing laser; and L is the system size.

In typical MAGPIE experiments, values of these parameters are in the region:

- $\lambda \sim 1\,\mu\text{m}$
- $\bar{n_e} \sim 5\times 10^{17}\ \text{cm}^{-3}$
- $\bar{B} \sim 1\,\text{T}$
- $L \sim 1\text{cm}$

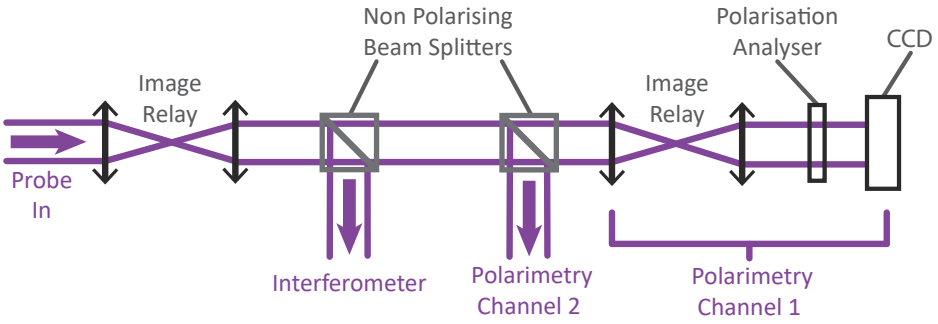

Figure 2.10: A schematic representing optical elements in an imaging Faraday rotation diagnostic.

and this implies that rotation angles are $\sim 1\,\text{deg}$. This is very small, but just about measurable rotation.

A diagram of the optical setup which is used to make measurements of α and to infer the average magnetic field strengths obtained in an experiment is shown in figure 2.10. The diagnostic employs a linearly polarised laser beam which is passed through a plasma. The probe is then split into three separate components. One of these is used to perform interferometry, which provides a spatially resolved map of $n_e L$, as described above. The other two channels are directed through polarization analysers before being imaged onto CCD cameras. The polarisation analysers consist of linear polarisers mounted on stepper motors. Two polarimetry channels are used in order exclude error introduced by plasma self emission. The polarisers are positioned at angles $\pm\beta$ from extinction, where β is typically around 2 deg.

In order to obtain magnetic field maps from this data, background images are taken with the two polarisation channels just before the shot. The exposure on a given pixel in these images is given by

$$S_{B\pm}(x,y) = s_{\pm}(x,y) I_B(x,y) \sin^2(\beta), \tag{2.22}$$

where x and y index pixels in the image; $s_{\pm}(x,y)$ is the response of the pixel; and $I_B(x,y)$ is the intensity distribution in the probe beam. Another two images are taken with the polarisation channels during the experiment, and the signals in these images are given by

$$S_{E\pm} = s_{\pm}(x,y)\left[I_E(x,y)\sin^2(\alpha(x,y) \pm \beta) + \frac{1}{2} I_{SE}(x,y)\right], \tag{2.23}$$

where $I_E(x,y)$ is the intensity in the intensity distribution in the probe beam; and $I_{SE}(x,y)$ is the intensity distribution resulting from plasma self emission. The contribution from self emission is assumed to be unpolarised, and so 1/2 of the total signal gets through the polariser regardless of the angle β.

In order to obtain rotation maps from these images, the difference between relative signals, denoted $D(x,y)$, is calculated. It can be shown [Swadling, 2014] that this quantity is related

to $\alpha(x, y)$ by the equation

$$D(x, y) = \frac{I_{E+}}{I_{B+}} - \frac{I_{E-}}{I_{B-}} = \frac{I_E}{I_B} \frac{2\sin(2\alpha)}{\tan\beta}. \tag{2.24}$$

In general the intensity profile for the probe beam is relatively repeatable and so $I_E/I_B \approx 1$. It therefore follows that

$$\int n_e \mathbf{B} \cdot d\mathbf{l} = \frac{k}{\lambda^2}\alpha(x, y) = \frac{k}{2\lambda^2} \sin^{-1}\left(D(x, y) \times \frac{\tan\beta}{2}\right), \tag{2.25}$$

where

$$k = \frac{8\pi^2 \epsilon_0 m_e^2 c^3}{e^3}. \tag{2.26}$$

Since the diagnostic includes a separate channel which is devoted to interferometry, it is possible to independently measure the value of

$$n_e L = \int n_e dl, \tag{2.27}$$

along the same path as for the polarogram. This means that, by dividing the value of equation 2.25 by equation 2.27, one obtains spatially resolved maps of

$$\frac{\int n_e \mathbf{B} \cdot d\mathbf{l}}{\int n_e dl}, \tag{2.28}$$

which is a weighted average of the component of magnetic field parallel to the path of the probing laser.

This seems relatively simple, but it is important to acknowledge that Faraday rotation is a difficult diagnostic to implement. The main reason for this is that the rotation angles induced by the effect are relatively small ($\sim 1\,\text{deg}$ for MAGPIE experiments), and so requirements in terms of signal to noise are quite high. To obtain good quality Faraday data the diagnostic setup on MAGPIE includes several important features.

The first of these is to use a probe with $\lambda = 1\,\mu\text{m}$. This is a compromise – the induced rotation scales with λ^2, so a longer wavelength induces a larger rotation angle. However, if the wavelength is pushed too high then glass becomes very absorptive and so refractive optics cease to be viable. 1 µm is about the largest wavelength for which optical components are readily available. In addition to this, the CCD detectors used for polarimetry channels are 16-bit astrophotography cameras. This bit-depth translates to a larger dynamic range in measurments when compared to images taken with more conventional 8-bit CCDs.

The laser used for Faraday rotation measurements is amplified to 10 J – most of this energy is dumped in neutral density filters, positioned upstream of the CCDs, but the high energy in the probe means that the relative contribution from plasma self emission is reduced. The seed laser for the probe is provided from an external laboratory (the Cerberus laser facility) . Having access to this laser is invaluable since the facility is staffed by a dedicated team

of photonics experts so the beam quality and pulse-to-pulse repeatability are exceptional – both of which are really crucial for high quality Faraday rotation measurements.

2.2.4 Thomson Scattering

Fundamentally, Thomson scattering describes a process in which a photon elastically scatters off a free electron . This process is non-relativistic, which requires $\hbar\omega << m_e c^2$ (where ω is the frequency of the incoming wave). The equivalent high energy (inelastic) scattering process is known as Compton scattering.

For a single electron, the spectral and angular distribution of scattered radiation are functions of the motion of the charge relative to the observer. For an ensemble of charges (such as the electron population in a plasma), spectral and angular distributions of radiation can be related to some average over the probable motions of the ensemble. By measuring the spectral distribution of light from a probing laser which has been Thomson scattered by a laboratory plasma, it is possible to infer some properties of the plasma in the region from which the light was scattered. Thomson scattering is widely used as a plasma diagnostic. In the context of high energy density physics experiments, it is used frequently on both laser [Katz, 2013] and pulsed power [Byvank, 2019; Swadling, 2014] driven experiments.

The equations describing the conservation of energy and momentum for Thomson scattered photons are given by

$$\omega = \omega_s - \omega_i \tag{2.29}$$

$$\mathbf{k} = \mathbf{k_s} - \mathbf{k_i}, \tag{2.30}$$

where $\omega_i/\mathbf{k_i}$ are the frequency/wave vector of the incident wave; $\omega_s/\mathbf{k_s}$ are the frequency/wave vector of the incident wave; an $\omega/\mathbf{k}$ are the frequency/wave vector describing a mode of the ensemble which couples the incident and scattered photon in the interaction. From the momentum conservation equation it follows that

$$k^2 = k_i^2 + k_s^2 - 2k_i k_s \cos\theta. \tag{2.31}$$

In this equation, θ denotes the angle between $\mathbf{k_i}$ and $\mathbf{k_s}$ which is shown in figure 2.11.

A concise derivation for the spectrum of scattered light is given in [Hutchinson, 2002, p. 293]. Heuristically one begins by showing that the intensity of scattered light is proportional to the Fourier transform of electron density over space and time. This quantity is called the spectral density function and is denoted $S(\mathbf{k}, \omega)$.

In contrast to the approach adopted to derive equations for interferometry, here one needs to consider fast fluctuations in density which occur due to thermal fluctuations in the plasma [2]. In order to obtain an expression for the electron density including these

[2] This is true because Thomson scattering is an inelastic process so electrons do not loose much energy in the interaction, implying that $\omega << \omega_i$ and $k << k_i$

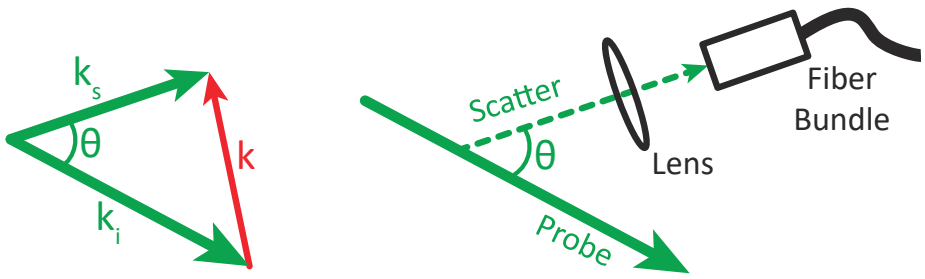

Figure 2.11: *Left:* A vector diagram showing the incident and scattered wave vectors for a Thomson scattering setup. *Right:* A schematic showing the experimental setup used used for Thomson scattering experiments on MAGPIE.

fluctuations considers velocity distributions of the form

$$f_q = f_{0j} + f_{1j} \tag{2.32}$$

where f_{0j} is the ensemble averaged velocity distribution for the species index by j; and f_{1j} is a first order perturbation. At this point an important assumption is introduced – that is the ensemble averaged velocity distributions are Maxwellian-Boltzmann distributed. Electrons and ions may still have different characteristic temperatures and also drift with respect to one another. In general it is possible to derive spectral density functions for a different choice of velocity distribution however distinguishing between Maxwellian and non-Maxwellian distributions from experimental data is usually quite hard.

The assumed velocity distributions are then used as an input to the Klimontovich equations. To simplify the result it is assumed that there are no collisions, and that $\mathbf{B} = \mathbf{0}$. The first assumption is valid in the limit $2\pi\nu_e << \omega_i$ where ν_e is the electron collision frequency. In this limit, electrons are unlikely to collide on the timescale of the Thomson scattering interaction. The second assumption seems odd in the context of MAGPIE experiments, however, it turns out the perturbations introduced by including magnetised modes are negligible for almost any reasonable choice of scattering geometry[Froula, 2011, p. 277].

The result which is eventually obtained states that the spectral density function is given by the equation

$$S(\mathbf{k},\omega) = \frac{2\pi}{k}\left[\left|1 - \frac{\chi_e}{1+\chi_e+\chi_i}\right|^2 f_{e0}\left(\frac{\omega}{k}\right) + \left|\frac{\chi_e}{1+\chi_e+\chi_i}\right|^2 Z f_{i0}\left(\frac{\omega}{k}\right)\right]. \tag{2.33}$$

In this equation the contribution to susceptibility from the species j is denoted χ_j; the ensemble averaged velocity distribution for the species j (assumed to be Maxwellian) is denoted $f_{j0}(v)$; and Z is the ion charge number.

The form of a Maxwellian velocity distribution function is

$$f_{0j} = \sqrt{\frac{1}{\pi v_{j,t}}} e^{-\left(\frac{v_j}{v_{j,t}}\right)^2}, \tag{2.34}$$

where $v_{j,t}$ is the thermal speed of the species j. This is given by

$$v_{j,t} = \sqrt{\frac{2k_B T_j}{m_j}}, \tag{2.35}$$

where T_j is the temperature of the species j; m_j is the mass of the species j; and k_B is Boltzmann's constant.

The contribution to the susceptibility from ions is

$$\chi_i = \frac{-\alpha^2 Z T_i}{2T_e} \mathcal{Z}' \left(\frac{\omega/k}{v_{i,t}}\right), \tag{2.36}$$

and the expression for the ion contribution is

$$\chi_e = \frac{-\alpha^2}{2} \mathcal{Z}' \left(\frac{\omega/k}{v_{e,t}}\right). \tag{2.37}$$

Here α is a often referred to as something like "the alpha parameter of Thomson scattering", and is given by

$$\alpha = \frac{1}{k\lambda_D}, \tag{2.38}$$

where λ_D is the Debye length.

Returning to the susceptibility equations, $\mathcal{Z}(x)$ is the plasma dispersion function, and $\mathcal{Z}'(x) = d\mathcal{Z}(x)/dx$. I am not going to go into any details about this function but its general significance is described in [Schekochihin, 2020, p. 38] and techniques for evaluating it numerically are discussed in [Froula, 2011, p. 433].

This treatment neglects the influence of plasma motion on Thomson scattering spectra. The effects of bulk plasma motion and electron drift can be included by making the substitutions

$$\frac{\omega/k}{v_{i,t}} \rightarrow \frac{\omega/k - \mathbf{v_i} \cdot \hat{\mathbf{k}}}{v_{i,t}}, \tag{2.39}$$

$$\frac{\omega}{v_{e,t}} \rightarrow \frac{\omega/k - (\mathbf{v_i} + \mathbf{v_e}) \cdot \hat{\mathbf{k}}}{v_{e,t}} \tag{2.40}$$

to the equations described above[3]. Here, $\mathbf{v_i}$ denotes the bulk motion of the plasma, and $\mathbf{v_e}$

[3] This substitution disagrees with the calculation of the Thomson form factor detailed in [Froula, 2011, p. 433]. In this reference, a similar substitution is made to the arguments of the velocity distributions but only the contribution of electron drift is included in the calculation of $\chi_{e/i}$. It is correct to include the substitution in the calculation of susceptibility since what matters is the response of the plasma at the Doppler shifted frequency.

is the electron drift velocity so, when $\mathbf{v_e} = \mathbf{0}$, the electrons move together with the ions.

Overall there is a significant amount of complexity underpinning the use of Thompson scattering as a diagnostic. A key detail to draw out of this is that there exist three separate contributions to the spectral density function which is shown in equation 2.33. There are two terms proportional to f_{e0} and one which is proportional to f_{i0}. The first term which is proportional to f_{e0} has no dependence on χ_e or χ_i and this means it has no dependence on the alpha parameter. The magnitude of the second electron distribution term and the ion distribution term both increase as α increases.

Physically α can be interpreted as being a measure of the extent to which electrons exhibit collective behaviour within the length scale of the Thomson scattering interaction. When $\alpha = 1/(k\lambda_D) << 1$, the electrons are effectively free within the interaction length so thermal fluctuations of the plasma do not get involved and the scattering process is incoherent . When alpha is large the influence of thermal fluctuations becomes dominant.

Phenomenologically the first electron distribution term is the result of incoherent scattering. The second electron distribution term and the ion distribution term arise from coherent scattering processes. The coherent electron distribution term arises from electron plasma waves (EPWs) and the associated dispersion relation is $\omega \approx \omega_{pe}$. The ion distribution term arises from ion-acoustic waves for which the dispersion relation is $\omega = C_S k$, where C_S the sound speed ($C_S = \sqrt{(ZT_e + T_i)/m_i}$, assuming an ideal gas equation of state).

The Thompson scattering setup used on most MAGPIE experiments is designed to diagnose the ion-acoustic feature and so subsequent discussion in this section will be limited to the use of the ion feature as a plasma diagnostic.

Thomson Scattering on MAGPIE

Figure 2.11 shows a (rather high level) schematic of the Thomson scattering setup which is used for experiments on MAGPIE. The setup consists of a probe laser which is directed as a focussed beam and passed through the experimental chamber. Thomson scattered light is collected by a lens outside of the experimental chamber and imaged onto a linear array of fiber optics. The setup collects Thomson scattered light from the points along the chord which is defined by the path of the focussed beam as it propagates through the chamber. The size of each scattering volume is defined by the waist of the focussed beam in one dimension, and the size of the region which is imaged onto each fiber in the other two dimensions. The fibers relay scattered light to the entrance slight of a spectrometer. The fiber arrays used for most experiments consist of 14 fibers, with a separation of 450 µm between their centres, and a core diameter of 100 µm. The spectrometer used for Thomson scattering experiments is an Andor SR 5001-A which is coupled to an intensified CCD detector. The gate used on the detector is ~ 4 ns in most experiments. The probe delivers 1 J to the target chamber in a 7 ns pulse with a wavelength of 532 nm (ND:YAG at 2ω).

An experimental detail which is important to consider is the contribution to broadening in the measured spectrum which is introduced by the finite resolution of the spectrometer.

For experiments on MAGPIE, the spectral width of the probing laser pulse is significantly smaller than the resolution of the spectrometer, and so the spectral response function can be taken from the shape of the un-scattered probe beam (measured before a shot). The calculated spectral density function is then convolved with this spectral response in order to obtain the fitting function which is applied to experimental data. In the discussion below we will see that the width of the ion feature is of order 5 Å in conditions relevant to MAGPIE experiments. This is really quite narrow – we are working at the limit of what can be achieved with a commercial spectograph in the visible. The implication is that the contribution to broadening from spectral response should not be neglected. If it is neglected, this will lead to a significant systematic error in measured plasma parameters.

Sensitivity of the Ion Feature to Different Plasma Parameters

Below, plots of a few synthetic Thomson scattering spectra will be discussed in order to demonstrate which plasma parameters may be diagnosed via a measurement of the ion feature. The spectra do not include the effect of instrumental broadening. Unless another value is stated in the figure legend, the spectra are generated with an average ionic charge of 6; an atomic weight of 6; $T_e = T_i = 70\,\mathrm{eV}$; and $n_e = 5 \times 10^{17}\,\mathrm{cm}^{-3}$. The scattering angle was set to be $\theta = 45\,\mathrm{deg}$. These values were chosen to be indicative of conditions which are typical for MAGPIE experiments.

Figure 2.12 shows the sensitivity of the form factor to changes in electron and ion temperature. The spectra consists of two symmetric peaks, centred on the probe frequency. The two peaks can be attributed to oppositely propagating ion acoustic waves. In a qualitative sense, the plot shows that increasing the ion temperature increases the width of the two peaks. Increasing the electron temperature increases the septation between peaks. In fact, it turns out that the ion feature is only sensitive to the product of ion charge number and electron temperature (ZT_e). In order to obtain independent values of Z and T_e, a lookup tables of Z as a function of T_e is used. These tables were generated using the atomic physics code SPK, developed at Imperial [Chittenden, 2016] which uses a collisional radiative equilibrium treatment. In general, average ionisation state depends n_e as well as T_e but MAGPIE experiments are in a relatively low density regime ($n_e \sim 5 \times 10^{17}\,\mathrm{cm}^{-3}$), where dependence on density is fairly weak and all of tables are calculated at a fixed electron density.

Figure 2.13 shows how the form factor changes in response to bulk motion. The spectrum is offset from the probe wavelength due to a Doppler shift in the scattered light. The effect of electron drift is not shown, but this induces an asymmetry between the intensity of the two ion acoustic peaks due to Landau damping.

Figure 2.14 shows how the form factor changes in response to increasing electron density. The ion feature is relatively insensitive to variations in electron density so, in experiments on MAGPIE, the density is typically determined from interferometry measurements and not left as a free parameter in fitting the form factor.

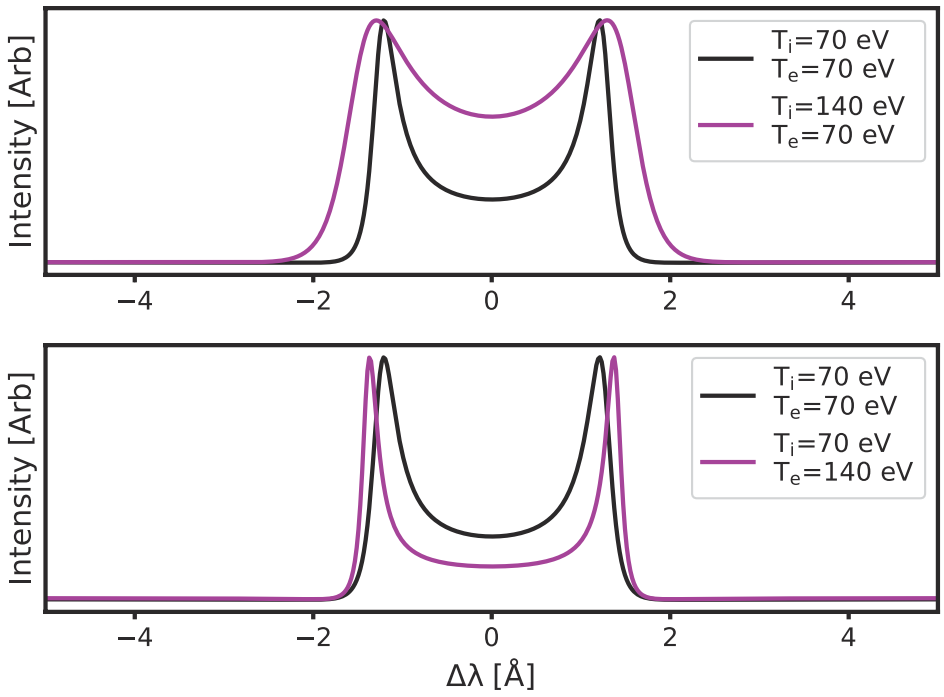

Figure 2.12: Sensitivity of the ion feature to changes in electron and ion temperature.

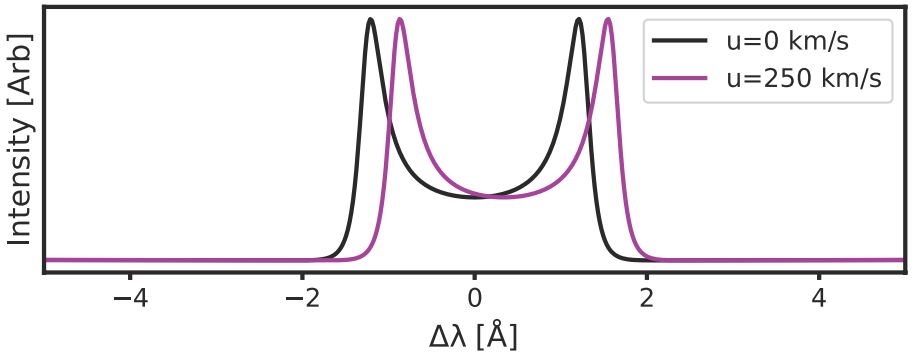

Figure 2.13: Doppler shift of the ion feature in response to bulk plasma motion.

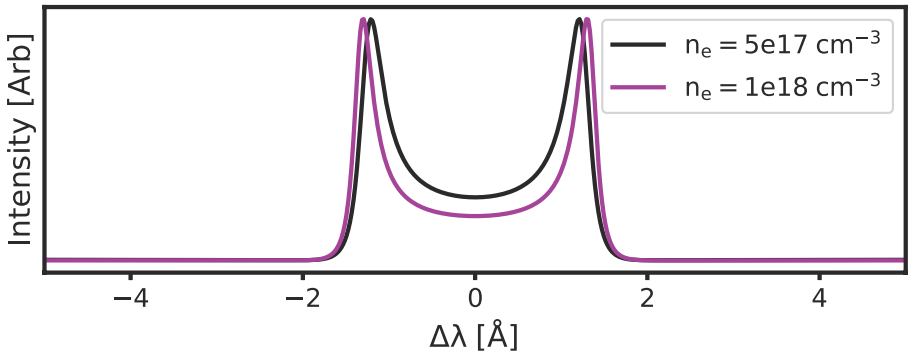

Figure 2.14: Sensitivity of the ion feature to changes in electron density.

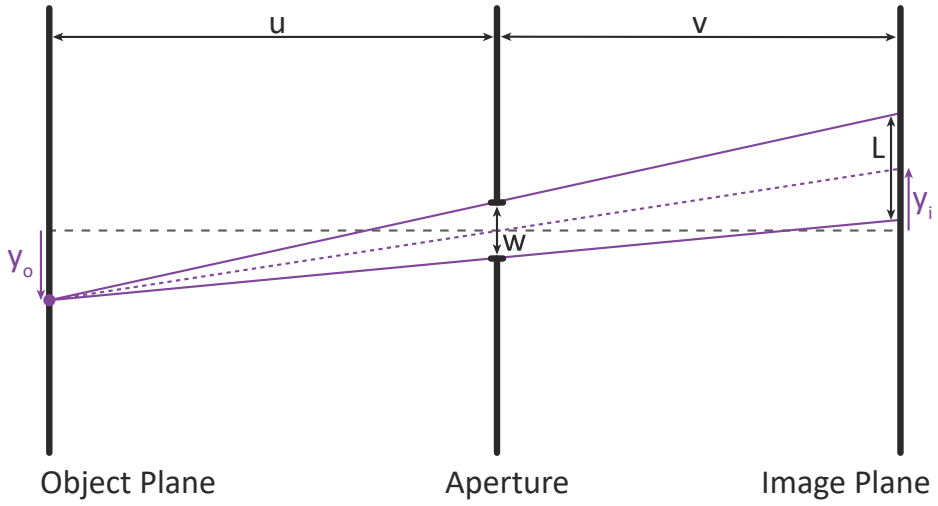

Figure 2.15: A diagram showing the position and size of an image cast by a point source offset from the optical axis.

2.3 X-Ray and XUV Self Emission Diagnostics

X-Ray and XUV based measurement techniques are usually employed to diagnose plasmas which are too hot/dense to be diagnosed using laser probing diagnostics. In this section I discuss the various X-Ray and XUV diagnostics available for experimental campaigns on MAGPIE.

2.3.1 Pinhole and Slit Imaging Systems

A simple technique to image XUV or X-Ray emission is to use an X-Ray aperture as an imaging optic. In spite of (or perhaps because of) its simplicity, pinhole imaging is used fairly widely in HED science [Bland, 2004; Theobald, 2018; McPherson, 2016].

The principle behind this technique is demonstrated in figure 2.15. This is a ray diagram which shows the position and extent of a region on an image plane which is illuminated by light cast from a point source on the object plane, offset from the optical axis by a distance y_o. The diagram shows that the centre of the region which is illuminated by the point source is also offset from the optical axis, by a distance y_i, which is a function of the geometry of the imaging system and the distance y_o. This implies that the system images light from the object plane onto the image plane. The magnification is defined as the ratio y_i/y_o, and from the diagram it is clear that this is given by

$$M = \frac{y_i}{y_o} = \frac{v}{u}, \tag{2.41}$$

where u [or v] is the perpendicular distance between the object plane [or image plane] and the aperture.

The diagram also shows that a point source illuminates light over a finite region of the

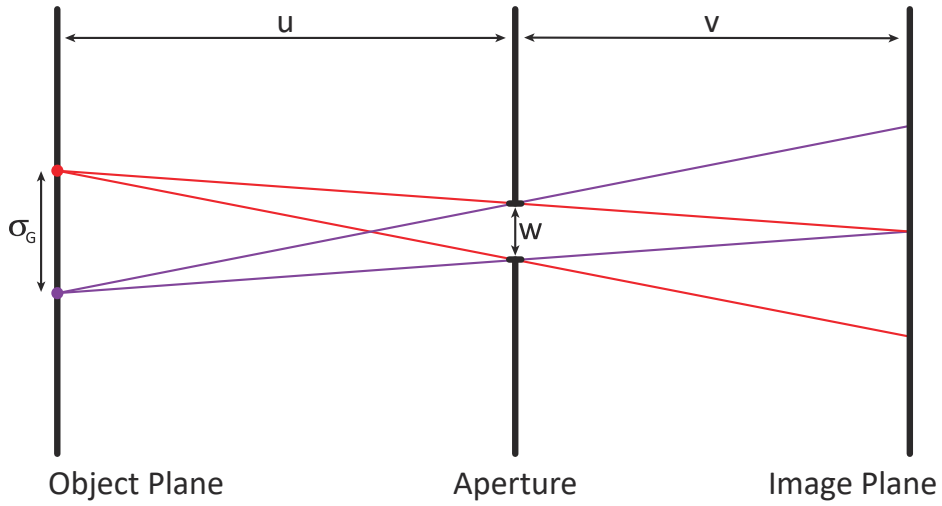

Figure 2.16: A diagram showing the size and position of the images cast by two point sources offset symmetrically from the optical axis.

image plane, of size L, when imaged by an aperture of size w. This finite aperture effect imposes a limit on the resolution of the imaging system which is based entirely upon its geometry. Figure 2.16 illustrates this point. It shows the region on the image plane which is illuminated by two point sources, offset symmetrically from the optical axis, and separated by a distance σ_G. This is the distance required for the regions illuminated by the two sources to *just* overlap on the image plane. From the diagram, it can be shown that this distance is given by

$$\frac{\sigma_G}{w} = \frac{u+v}{v} = \frac{1+M}{M}. \tag{2.42}$$

The distance σ_G is the minimum offset required to allow one to distinguish between the two sources so is a measure of the resolution of the imaging system, referred to as the system's geometric resolution.

Another limit on imaging resolution is the minimum distance between two sources before they are indistinguishable due to the diffraction of light through the aperture. For a circular aperture, this limit is usually defined via the Rayleigh criterion: the two images are just resolved when the centre of the Airy diffraction produced by one source falls on the first minimum of the Airy pattern produced by the second source. In the far field, the minimum distance on the *image plane* is

$$\Delta l = \frac{1.22\lambda v}{w}, \tag{2.43}$$

where λ is the wavelength of light produced by the sources[Hecht, 2016, p. 493]. To be consistent with the definition of geometric resolution stated above, one should really define diffractive resolution in terms of the separation between two sources on the *object plane*.

By applying equation 2.41 to the usual Rayleigh criterion result, one obtains the equation

$$\sigma_D = \frac{1.22\lambda u}{w}, \tag{2.44}$$

where σ_D is the (diffraction limited) resolution of the imaging system. This can be restated as

$$\sigma_D\ [\text{mm}] = \frac{1.51 \times u\ [\text{mm}]}{w\ [\mu\text{m}] \times \varepsilon\ [\text{eV}]}, \tag{2.45}$$

where ε is photon energy, and the various units are chosen to be convenient for experimental work.

All of the pinhole imaging data presented in this thesis operated in a regime where geometric effects were dominant but in general it is important to acknowledge that both factors may contribute to the resolution of a given instrument.

In general, the apertures used for X-Ray imaging are either circular or rectangular in shape. Circular apertures are referred to as pinholes, and rectangular ones are called slits. By considering the extension of figure 2.15 to a two dimensional system, it can be shown that a pinhole images features in two dimensions whereas a slit images features in one dimension and is spatially integrating in the other (so long as the width of the slit is much smaller than its length).

Designing X-Ray Imaging Systems

It is often useful to combine several X-Ray imaging systems into a single diagnostic. One reason this is the case is because different spectral filters might be applied to the images in order to infer details about the spectral character of plasma emission. Alternatively, a system could be used with independent time gated detectors to obtain time resolved measurements of X-Ray emission.

In order to determine the geometry of a diagnostic which involves multiple imaging systems it is useful to construct a simple model of the design in computer aided design (CAD) software. A screen shot of such a model is shown in figure 2.17. As can be seen in the image, an imaging system can be reduced to four components:

1. The object plane
2. A large aperture (often called a baffle)
3. The imaging aperture (in this case a pinhole)
4. The image plane

The figure shows four rays which intersect with the centre of the pinhole and the four corners of the baffle. These are extended to the image and object planes in order to determine the extent of the region which is imaged and the size of the image formed on the detector. The purpose of the baffle is to eliminate crosstalk between different imaging systems which

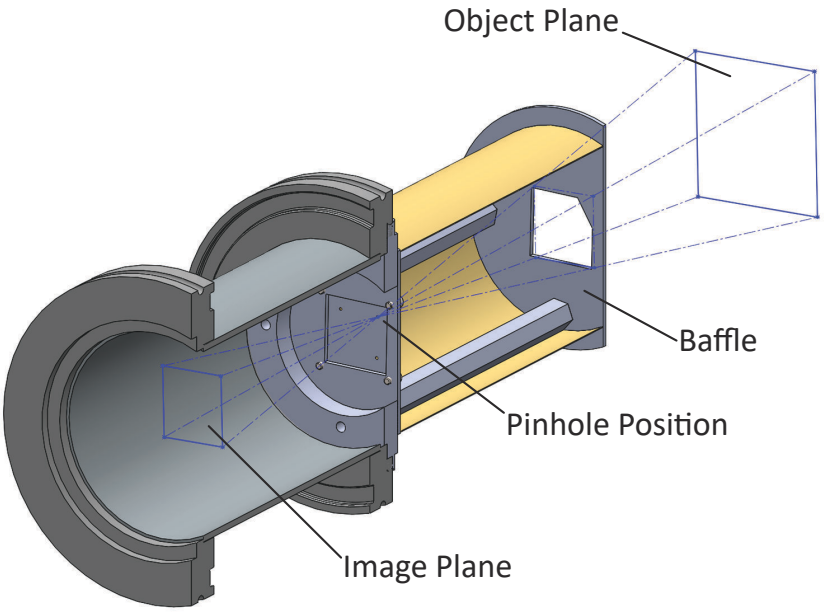

Figure 2.17: A ray-trace through a CAD model of a pinhole camera which shows the object plane, baffle, pinhole, and image plane.

are fielded in the same diagnostic. This concept is illustrated in figure 2.18 which shows a ray trace of an imaging system which uses four pinholes to produce independent image on the detector. The size and position of the baffle is chosen to ensure that the separate images do not overlap.

The setup shown in figure 2.18, is a standard design used to obtain some of the data presented later in this thesis. It was setup with $u = 220\,\text{mm}$, and $v = 100\,\text{mm}$, implying a magnification of 0.45.

2.3.2 X-Ray Spectroscopy With Spherically Bent Crystals

A common technique in X-Ray spectrometry is to exploit Bragg Scattering in a single crystal to disperse an X-Ray spectrum. Bragg's reflection law states that, for a grazing angle θ,

$$n\lambda = 2d\sin\theta, \tag{2.46}$$

where d is the separation between lattice planes; and n is an integer which indexes the order of reflection [Dyson, 1990, p. 149].

Whilst a flat crystals are sometimes used, it is quite common to spherically bend the planes of an X-Ray crystal to form an optic which provides both imaging and dispersion. An instrument which uses a spherically bent crystal is termed a 'Focussing Spectrograph With Spatial Resolution' (FSSR). The geometry is advantageous because it increases the

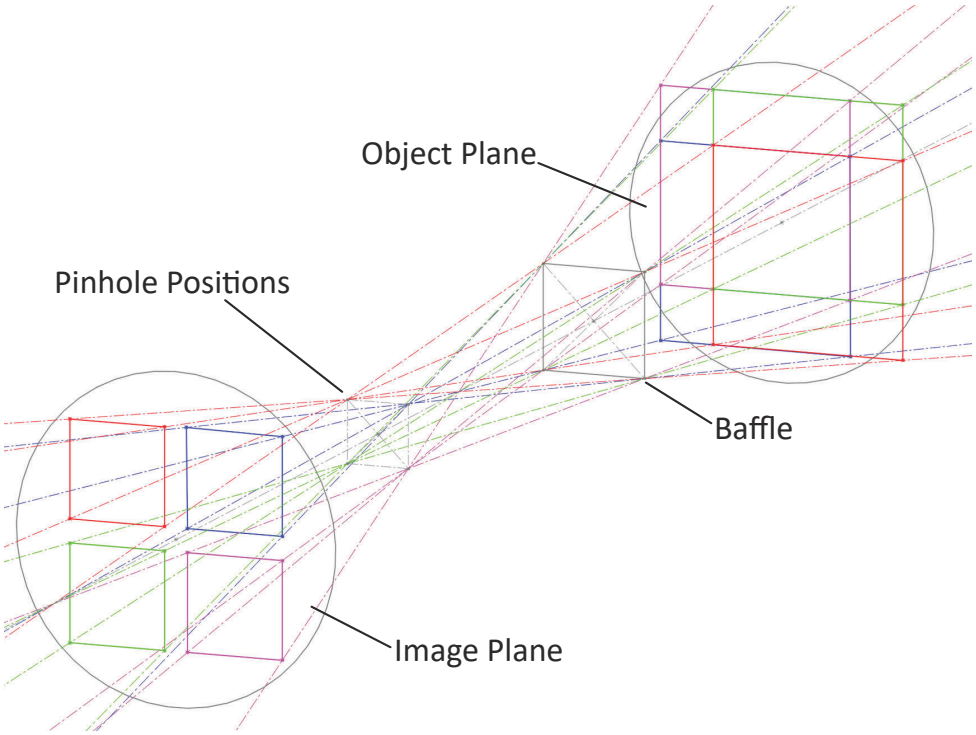

Figure 2.18: A drawing a the ray trace for a four frame pinhole camera. The interdependent imaging systems are indicated in different colours. The CAD model of the physical setup is hidden for simplicity.

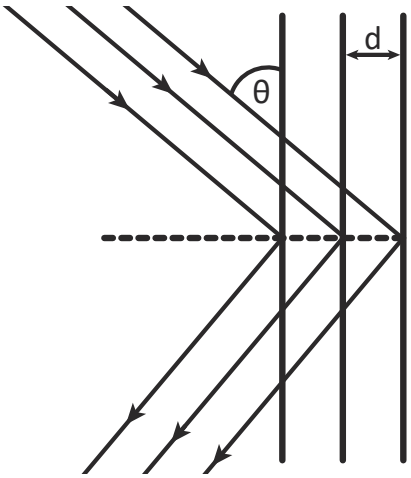

Figure 2.19: An illustration of Bragg Reflection.

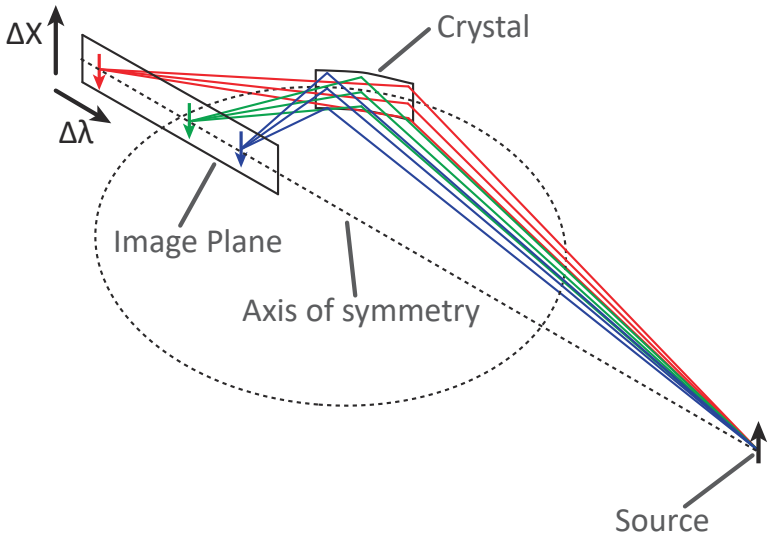

Figure 2.20: A diagram illustrating how an FSSR works. The circle indicated with a dotted line is constructed by extending the arc obtained from the intersection between the crystal and the meridional plane. The axis of symmetry is line which bisects this circle and is coincident with the position of the source.

X-Ray fluence on the detector, and provides spatial resolution. FSSRs are commonly used to study a wide variety of sources including Z-Pinches [Hall, 2006; Sinars, 2006], X-Pinches [Pikuz, 2015], laser produced plasmas [Gamboa, 2011], and magnetically confined plasmas [Bertschinger, 2004].

Figure 2.20 is a 3D drawing of an FSSR setup. It shows a source which emits X-Rays of three separate wavelengths. On the image plane the different wavelengths are spectrally dispersed along one axis, and the source's spatial structure is imaged along the perpendicular axis. The plane which is normal to the spatial axis of the image plane, and is coincident with the centre of the source, is called the *meridional plane*. The circle drawn with a dotted black line lies in the meridional plane, and it is the extension of the radius of curvature of the crystal. The line labelled axis of symmetry bisects this circle and is coincident with the position of the source. The focal length of the crystal is given by

$$f = \frac{r}{2}, \tag{2.47}$$

where r is the radius of curvature of the crystal and this implies that the image which is formed by the crystal is focussed on this axis of symmetry.

To increase X-Ray fluence FSSRs often do not use a spectral slit, and instead the size of an image in the spectral direction is limited by positioning the image plane so that light

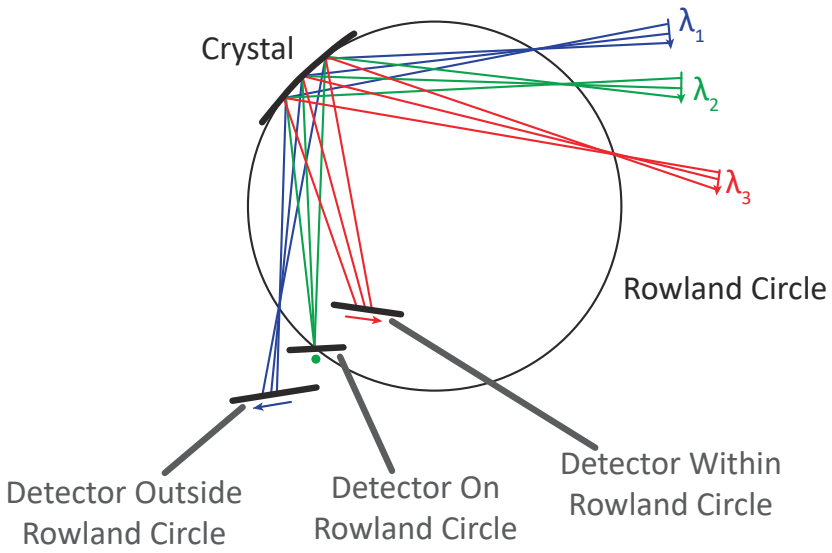

Figure 2.21: A diagram looking down onto the meridional plane in an FSSR setup. Three possible detector positions are shown. When the image formed does not intersect with the Rowland circle, the crystal is imaging in the spectral direction.

is perfectly focussed in the spectral direction, at some wavelength which is particularly interesting. To illustrate this concept it is useful to introduce a construction called the *Rowland circle*. This lies in the meridional plane; has a radius of $r/2$; and intersects with the crystal at the reflection point for a particular wavelength. The final condition (rather confusingly) implies that there exists a different Rowland circle for each wavelength emitted by a source at a particular location.

Figure 2.21 which shows the meridional plane geometry for an FSSR setup which images three sources of different wavelengths onto different detector positions. The positions of the sources are set such that they all share a common Rowland circle. The figure shows that when the object is imaged onto a position which lies on the Rowland circle, then an exact focus is achieved in the spectral direction (implied by equation 2.47). For the other two cases a defocused image is formed in the *spectral* direction. The image is inverted if an image is formed inside the Rowland circle, and is not inverted if an image forms outside of it.

An elegant approach to calculating the spectral band function, magnification, and dispersion for an FSSR setup is presented in [Pikuz, 2008]. What follows is an outline of the authors' argument.

Figure 2.22 shows the meridional plane geometry of an FSSR setup. From triangles ABD and AOD in this diagram,

$$a \sin \varphi = l \sin \omega \tag{2.48}$$

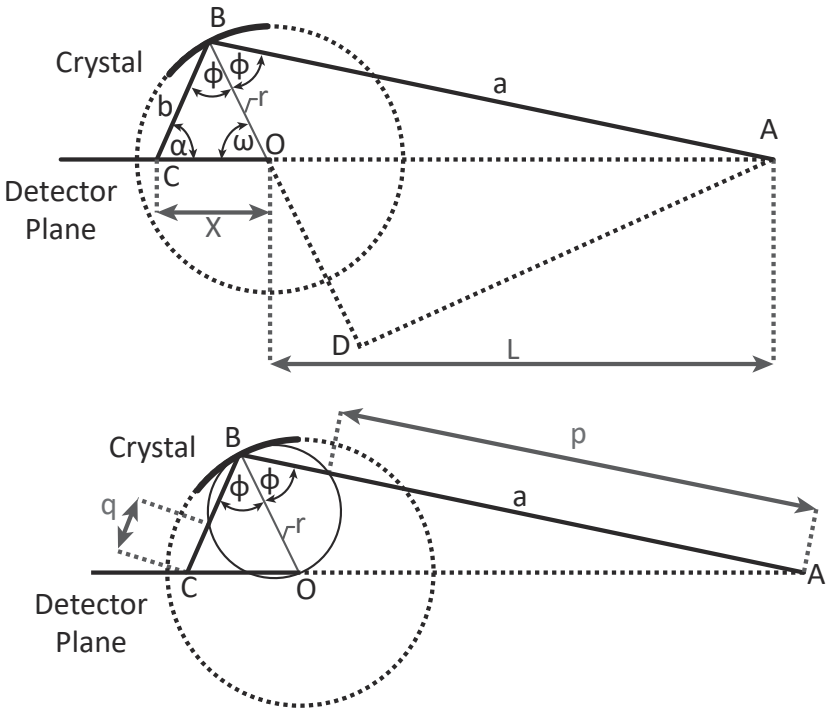

Figure 2.22: Diagrams showing the meridional plane geometry of an FSSR with and without the Rowland circle. Adapted from [Pikuz, 2008] with permission.

where applying the cosine rule to triangle BOA implies that

$$a = \sqrt{l^2 + r^2 - 2lr\cos(\pi - \omega)} = \sqrt{l^2 + r^2 + 2lr\cos\omega}, \tag{2.49}$$

and combining these two results yields

$$\varphi = \sin^{-1}\left(\frac{l\sin\omega}{\sqrt{l^2 + r^2 + 2lr\cos\omega}}\right). \tag{2.50}$$

By applying the sine rule to triangle BOC, it can be shown that

$$x\sin\alpha = r\sin\varphi, \tag{2.51}$$

and

$$b\sin\alpha = r\sin\omega. \tag{2.52}$$

Both of these equations can be refactored, using the property $\alpha = \pi - (\varphi + \omega)$, to yield

$$x = \frac{r\sin\varphi}{x\sin(\varphi + \omega)}, \tag{2.53}$$

and

$$b = \frac{r\sin\omega}{x\sin(\varphi + \omega)}. \tag{2.54}$$

From the diagram it can be seen that

$$p = a - r\cos\varphi, \tag{2.55}$$

and

$$q = b - r\cos\varphi. \tag{2.56}$$

The spatial magnification is given by

$$M_y = \frac{b}{a}, \tag{2.57}$$

and the spectral magnification is

$$M_\lambda = \frac{q}{p}. \tag{2.58}$$

The linear dispersion is given by

$$D_\lambda = \frac{dx}{d\lambda}. \tag{2.59}$$

The angle φ is related to the grazing angle by the equation $\varphi = \frac{\pi}{2} - \theta$, and so Bragg's reflection law as a function of φ is given by

$$n\lambda = 2d\cos\varphi. \tag{2.60}$$

In order to treat the output of a spectrograph, you need to know the spectral form function – that's to say position on the image plane as a function of $n\lambda$. It is also helpful to obtain the form of the functions $M_\lambda(n\lambda)$, $M_y(n\lambda)$, and $D_\lambda(n\lambda)$.

The approach taken by Pikuz *et al* was to note that the equations presented above give the form of all these as a function of either φ, or φ and ω. Since equation 2.50 gives the form of $\varphi(\omega)$, one can calculate the form of the functions numerically by varying ω whilst holding l, r, and d fixed.

The FSSR which was fielded on MAGPIE used a Mica crystal ($2d = 19.88\,\text{Å}$), with $r = 186\,\text{mm}$, and $l = 458\,\text{mm}$. Figure shows the form of the spectral band, magnifications, and linear dispersion for this setup.

2.3.3 X-Ray Filtering

In order to spectrally filter X-Rays for a FSSR or pinhole imaging diagnostic, it is common to use thin metal foils or plastic films. These are typically placed on the pinhole for an imaging setup or at the position of the (spatial) focus point for an FSSR. In the context of a crystal spectrograph, filters are useful to eliminate the contribution from low energy background emission which might be imaged by the crystal at lower orders of Bragg reflection.

The fraction of X-Ray energy which is absorbed by the filter material is spectrally dependent, and is described by a quantity known as the linear mass absorption coefficient, denoted $\mu_a(\varepsilon)$ and typically expressed in $\text{cm}^2\,\text{g}^{-1}$. The fractional transmission through a

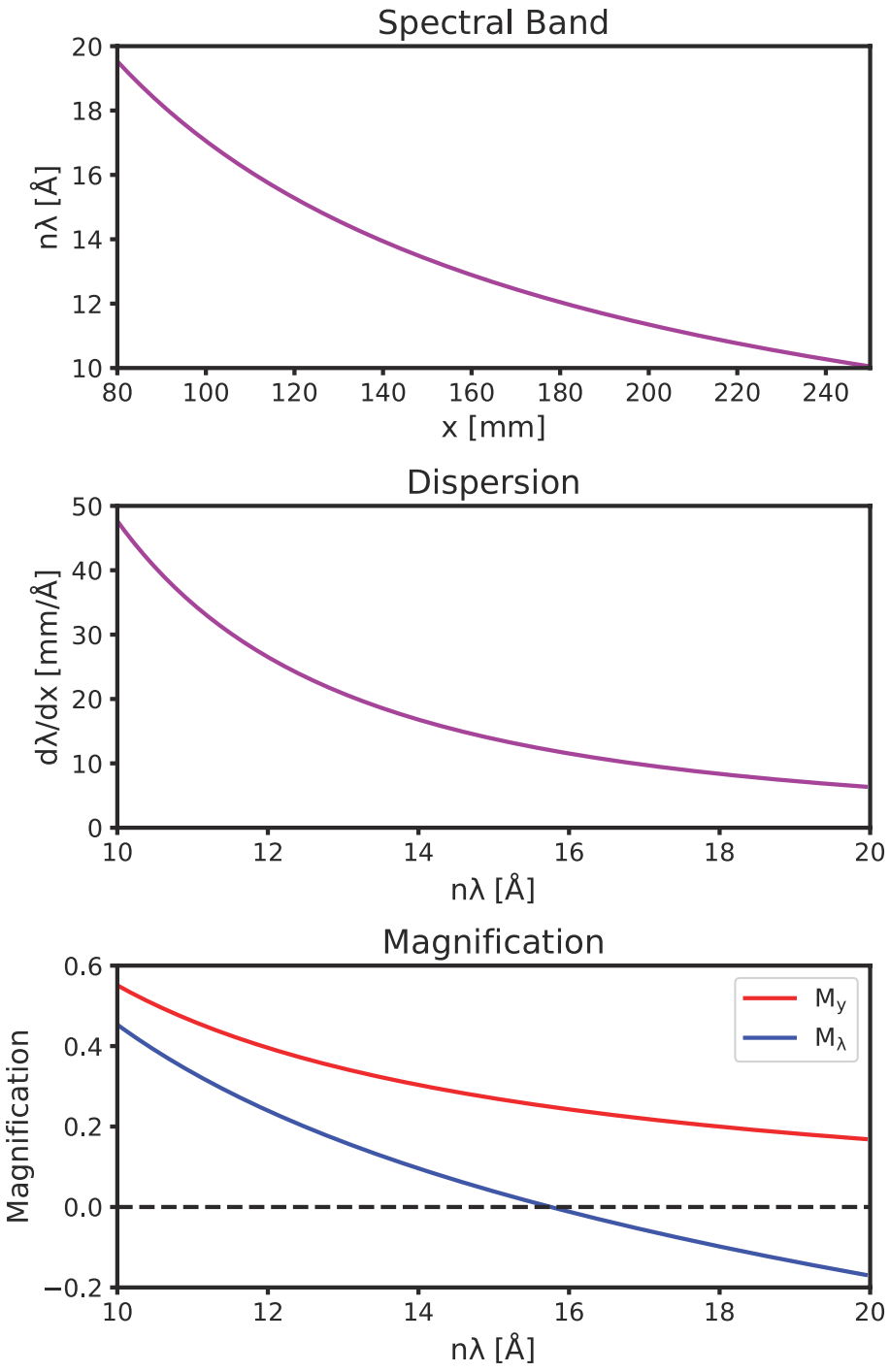

Figure 2.23: Plots of the spectral band function, magnification, and dispersion for an FSSR with $2d = 19.88\,\text{Å}$, $r = 186\,\text{mm}$, and $l = 458\,\text{mm}$. The range in $n\lambda$ which the plots cover corresponds to the range of values which could be accessed using the instrument.

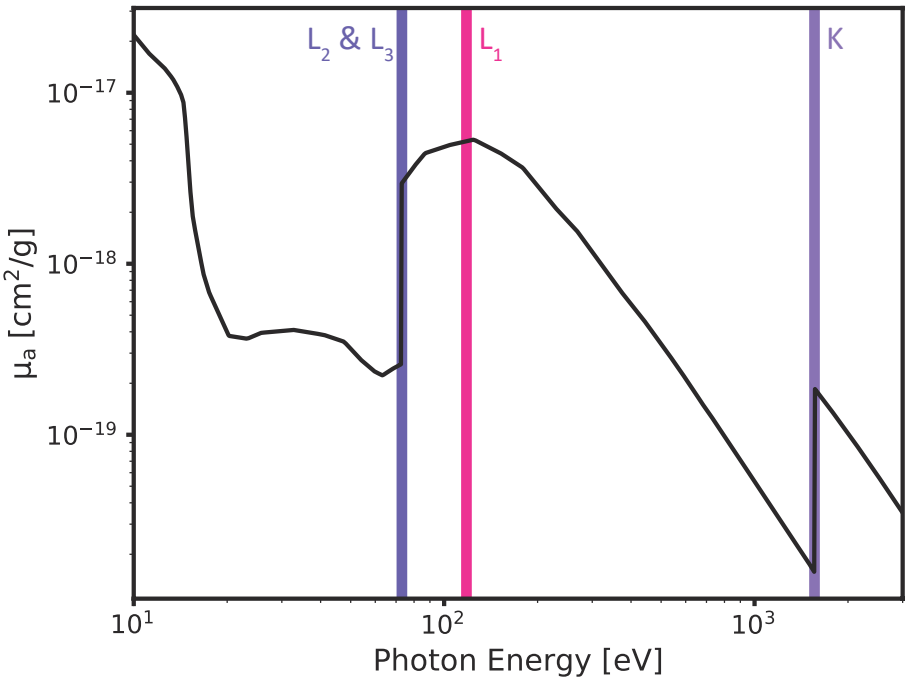

Figure 2.24: A plot of the photon energy resolved mass absorption coefficient for aluminium. Values in the range $10 - 100$ eV are taken from [Gullikson, 1994] and in the rest of the range values are taken from [Henke, 1993]. The positions of the K, L_1, L_2, and L_3 electron binding energies are marked with horizontal lines.

filter is given by

$$\mathcal{T}(\varepsilon) = \mathrm{e}^{-\mu_a(\varepsilon)\rho d}, \tag{2.61}$$

where ρ is the mass density, and d is the thickness of the filter [Henke, 1993].

The form of $\mu_a(\varepsilon)$ for aluminium is shown in figure 2.24. In general the spectral dependence is complicated, although prominent increases in μ_a occur at the position of the aluminium K and L shell electron binding energies. The analysis presented in this thesis relies on tabulated values of $\mu_a(\varepsilon)$, these were taken from [Henke, 1993] for all of the elements discussed except aluminium. The form of μ_a for aluminium used values from [Henke, 1993] for photon energies above 100 eV. At lower photon energies, values were taken from [Gullikson, 1994]. A convenient online interface [4] to obtain plots and tabulated values of transmission curves is maintained by E. Gullikson and hosted by The Lawrence Berkeley National Laboratory.

Transmission curves for 1 µm and 3 µm aluminium foil are shown in figure 2.25. A key thing to note from the figure is that, because μ_a is multiplied by d in the exponent, the form of $\mathcal{T}(\varepsilon)_{Al,3\,\mu\mathrm{m}} \neq k \times \mathcal{T}(\varepsilon)_{Al,1\,\mu\mathrm{m}}$, where k is an arbitrary constant. This means that comparing the transmission through filters made of the same material but with different thicknesses can provide information about the spectral character of the transmitted X-Rays.

[4] `http://henke.lbl.gov/optical_constants/`, accessed on 17th Jan 2020.

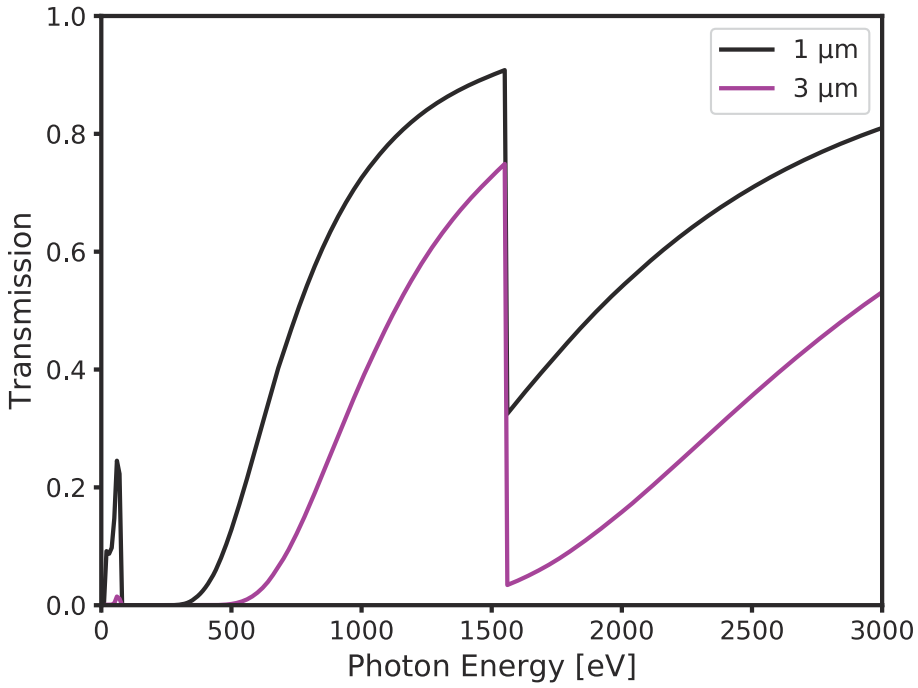

Figure 2.25: Transmission through 1 µm and 3 µm thick aluminium filters, calculated from the values of μ_a shown in figure 2.24.

Since the position of absorption features changes for different elements it is also possible to compare the transmission through filters made of different materials in order to estimate the spectral character of an X-Ray signal.

For lower photon energies (below around 100 eV), it is important to note that low-Z filter contaminants can have significant effect on the filter transmission curves. Such containments include the formation of an oxide layer on the outer surfaces of foils, and the deposition of hydrocarbons on the surface of both foils and films.

Figure 2.26 illustrates that the formation of a 85 Å thick aluminium oxide (Al_2O_3) layer reduces transmission through an 1 µm aluminium foil by a non-negligible amount for photon energies in the range $10 < \varepsilon < 100$ eV. This choice of oxide layer thickness was chosen based on values quoted in [Gullikson, 1994] – it is difficult to know if the oxide layers formed on filters used in this investigation were of comparable thickness but it seems unlikely that the thicknesses will be different by more than a factor ~ 2.

2.4 X-Ray Detection Technology

The discussion in the previous section focussed on X-Ray imaging techniques. In this section I will discuss various X-Ray detection technologies – that is to say technologies which are used to convert an X-Ray fluence or X-Ray dose to a voltage signal which is then applied to an ADC in order to create a digital representation of the signal measured in an experiment.

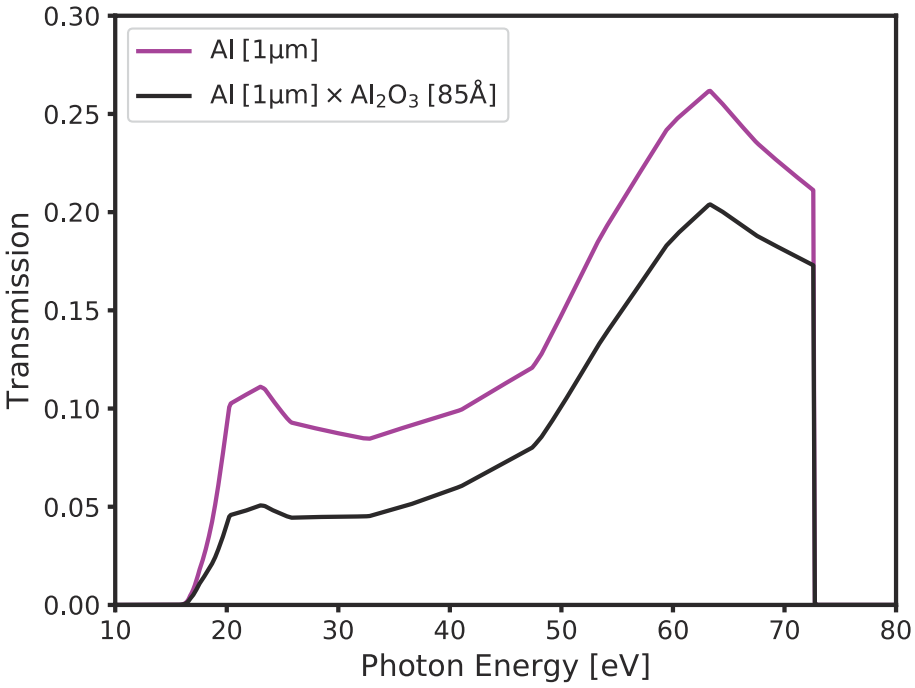

Figure 2.26: A plot demonstrating the influence of the presence of an 85 Å oxide layer on the transmission curve for a 1 µm aluminium filter.

2.4.1 Fujifilm Imaging Plate

Fujifilm Imaging Plate is a time integrating X-Ray detector, so measures the total X-Ray dose incident upon the plate during the course of an experiment. Image plates are comparatively cheap, reusable, and have an extraordinarily large dynamic range. That said, the way they work is rather complex, and there are a few pitfalls which are often encountered when working with them. The following discussion is rather lengthy because I think it important to acknowledge that the technology should not be treated as a black box.

Image plates consist of a flexible substrate onto which a storage phosphor ($CsBr : Eu^{2+}$) is deposited. A schematic of the energy level structure in the phosphor is shown in figure 2.27. The schematic shows that an incident X-Ray (or XUV) photon may promote an electron to the conduction band, leaving a hole in the valance band. There is some chance that the electron may fall into a so called 'electron trap', leaving the hole in an associated 'hole trap'. The phrase 'trap' is just industry specific jargon referring to a meta-stable excited state of the system.

By exposing the system to visible light ($\lambda \sim 600\,\text{nm}$), the trapped electron can be excited to a higher energy state which is not stable, causing it to recombine with the trapped hole. This recombination causes the system to occupy a further excited state, which decays, emitting 390 nm light in the process. The final excitation, and subsequent decay, are not shown in the diagram for the sake of simplicity. The induced decay process is referred to

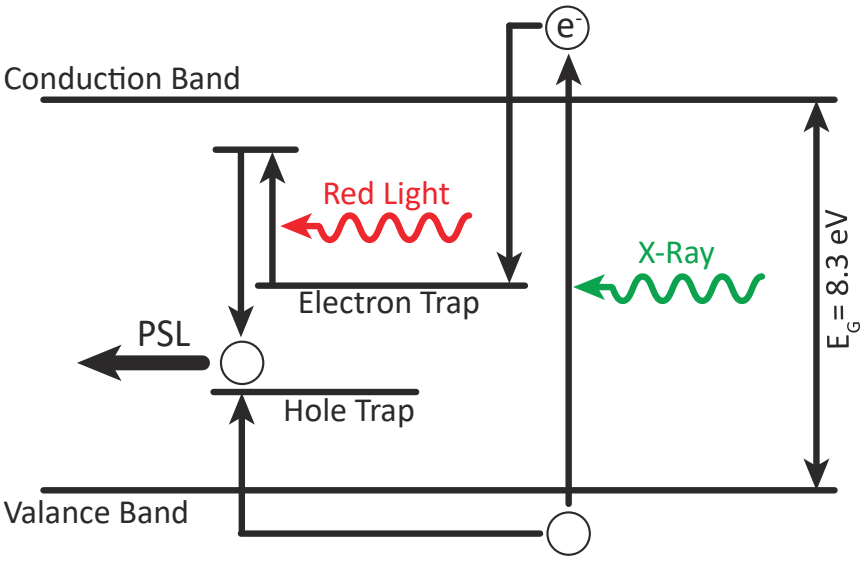

Figure 2.27: A schematic showing part of the energy level structure in CsBr : Eu^{2+} which is responsible for the photo-simulated luminescence process.

as Photo-Stimulated Luminescence (PSL) [Leblans, 2011].

Fujifilm manufacturer commercial scanners in order to readout the information stored on Image Plate. These contain a diode laser (typically $\lambda = 635\,\text{nm}$) and a Photo Multiplier Tube (PMT). The laser is used to illuminate small regions on the surface of the image plate, and the stimulated luminescence is recorded by the PMT.

The maximum dose which can be measured by the combined image plate and scanner system is limited by the maximum voltage which can be produced by the PMT. The maximum number of electrons which can be trapped by the storage phosphor tends not to limit the maximum dose which can be measured. This means a saturated plate may be scanned multiple times. With each scan, a fraction of the trapped electrons are able to relax, until the PMT is able to operate in a linear regime. It is difficult to relate the intensity of signals from multiple scans to those obtained in a single scan, but the spatial distribution of emission can still be recovered.

Three different specifications of image plate are widely used in the HEDP community. These are:

- Storage Phosphor Screen BAS-IP Tritium Screen (BAS TR)
- Storage Phosphor Screen BAS-IP Multipurpose Standard (BAS MS)
- Storage Phosphor Screen BAS-IP Super resolution (BAS SR)

In the BAS MS and BAS SR plates, the storage phosphor is covered by a $C_{10}H_8O_4$ layer. This is designed to protect the plate but also strongly absorbs X-Rays below about 1 keV. The BAS SR plates have a pixel size of $25\,\mu\text{m}^2$. The BAS TR and BAS MS plates have a pixel size of $50\,\mu\text{m}^2$ [Meadowcroft, 2008]. For BAS TR, the effective resolution of image

plate has also been measured to be a factor of around two times larger than the pixel size [Fiksel, 2012] – worth being aware of [5].

BAS TR imaging plate is recognisable because it is blue (rather than white) in colour. The colouring comes from an anti halo layer, which is placed under the storage phosphor, but because of this, BAS TR plates are often referred to as blue image plates by experimental physicists.

Conversion Between Quantum Levels and PSL units

The unit in which image plate data ought to be interpreted are referred to as PSL by Fuji. This is confusing as PSL also describes the the atomic process which is used to readout data from image plates, but it is a wide spread convention. In this context, the PSL value is proportional to the energy absorbed within a pixel on the plate (i.e. X-Ray dose). When analysing image plate data it is important to be aware that the data produced by a Fujifilm scanner is not stored as a bit-wise representation of PSL. Instead the raw bits in image plate data (referred to as quantum levels) have to be input to the equation

$$P\ [\mathrm{PSL/mm^2}] = \left(\frac{R[\mu\mathrm{m}]}{100}\right)^2 \times \frac{4000}{S} \times 10^{L\left(\frac{Q}{2^b-1}-\frac{1}{2}\right)}, \tag{2.62}$$

where P is the PSL value of a pixel; R is the resolution of the scan; S is referred to as the sensitivity of the scanner; L is the latitude applied to the scan; Q is the quantum level value of a pixel; and b is the bit depth of the scan.

The sensitivity and latitude are fixed for a given scanner, but may change between different models of scanner. The data is stored in this representation because the measurement of the voltage across the PMT which is made by the scanner has a much larger dynamic range than can be encapsulated by a linear 16-bit representation of intensity, and using quantum levels is a way to compress this information into a manageable file size. The word 'quantum' indicates that the bit levels are digitally quantised – it is not supposed to allude to anything relating to quantum mechanics [Dewar, 2019].

Relaxation time for stored electrons

It is notable that, for a plate kept at room temperature, the trapped electrons have a limited excited state lifetime [Leblans, 2011]. This means the PSL value which is measured from the plate will reduce depending on how long the plate is left between exposure and scanning. In [Meadowcroft, 2008], the authors quantify the relaxation process using the equation

$$P(t) = P_0 \mathrm{e}^{-t/\tau} + c, \tag{2.63}$$

[5] This publication also measured the spatial resolution of BAS SR ("Super Resolution") to be comparable to that of BAS TR and BAS MS which is rather amusing.

where t is the time between exposure and scanning; and the values P_0 and c are constants. For the exposures obtained in their experiment and BAS TR image plate, Meadowcroft *et al* found that $\tau = 36\,\text{min}$. This is quite a short timescale – something which definitely worth keeping in mind when working with image plate.

Low Energy X-Ray and XUV Response of Image Plate

Experimental data on Image plate response in the low energy limit, which (in the context of this discussion) I define as $5\,\text{eV} < \varepsilon < 1\,\text{keV}$, is fairly sparse. In [Meadowcroft, 2008], measurements of image plate response 2 keV – 100 keV are discussed. For energies below around 8 keV the response was measured to be linear with photon energy. There is also evidence in the literature that BAS TR image plate has response down to very low photon energies [Reader, 2000]. In the work I present here, it is assumed that image plate response is linear with photon energy above the bandgap in the phosphor, and exhibits no response below this threshold. This puts the cut-off at around 8 eV [Leblans, 2011]. The response model which is used simply represents my best guess based on what information is available and should be treated with a very high degree of uncertainty.

2.4.2 X-Ray Diodes

Silicon p-n junction photodiodes have a bandgap energy and X-Ray absorption characteristics which make them suitable for X-Ray fluence measurements. The principle is simple: X-Ray (or XUV) radiation falls on the surface of the diode and this induces the flow of current through it. The current is passed through a terminating resistor. The voltage across this is measured with an oscilloscope, and the measurement is used to infer the magnitude of the original X-Ray fluence on the surface of the diode.

Opto Diode produce a line of silicon diodes which they call Absolute Ultra Violet (AXUV) Silicon Photodiodes. They are sold for XUV intensity measurements and are suitable for this purpose because they are manufactured using a process which prevents the formation of a dead layer of silicon on their front surface . In conventionally manufactured diodes, the presence of a dead layer reduces XUV response to near zero as silicon is strongly absorbative to XUV radiation.

In the context of this work, they were an attractive technology but not because of their XUV response characteristics. They were used because their photon resolved response is known to be relatively consistent from diode to diode, meaning that they can be used to make absolute intensity measurements (with a degree of reliability) without having to absolutely calibrate each individual detector.

The photon energy resolved response curve for AXUV series photodiodes provided by the manufacturer is shown in figure 2.28, plotted along with the response model that was used for the work presented in this thesis.

An experimental detail which it is important to bear in mind when working with diodes

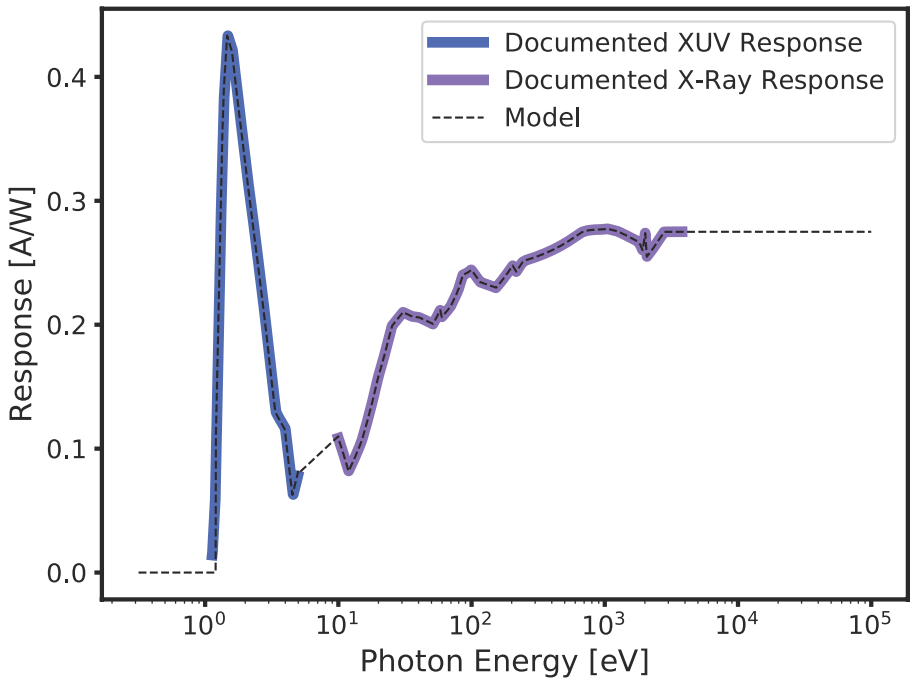

Figure 2.28: The Opto Diode AXUV series response curve for XUV and X-Ray radiation (taken from [OptoDiode, 2017]) plotted with the diode response model which was used for work presented in this thesis.

is their rise time – that's to say how quickly measured voltage $[V(t)]$ responds to a step change in the flux upon their surface. Unbiased diodes tend to have rise times on the order of micro-seconds due to their intrinsic capacitance. This can be reduced by applying a bias voltage, which reduces the width of their depletion region and hence their capacitance.

The biasing scheme used for the work presented in this thesis is shown in figure 2.29. The diode's anode was biased to $-9\,\mathrm{V}$, and a low pass filter (resistor and capacitor marked in red on the figure) was used to reduce electrical noise produced by the generator during an experiment. The $50\,\Omega$ terminating resistor, shown in purple, is what the oscilloscope measured voltage across.

The rise time of the system was empirically determined to be $\sim 1\,\mathrm{ns}$ by measuring how $V(t)$ responded to radiation from a $200\,\mathrm{ps}$ pulsed laser (AXUV diodes have a low-level response in the visible). The discharge time for the capacitor is around $50\,\Omega \times 220\,\mathrm{nF} = 11\,\mu\mathrm{s}$ so the bias is unlikely to be significantly depleted on the timescale of an experiment, which is less than $0.5\,\mu\mathrm{s}$.

2.4.3 Micro-Channel Plate Detectors

Micro-Channel Plate (MCP) detectors consist of an array of miniature photomultiplying channels, arranged in a parallel to form a plate, as shown in figure 2.30. The diameter of individual channels varies from $10 - 100\,\mu\mathrm{m}$, depending on the manufacturing technique

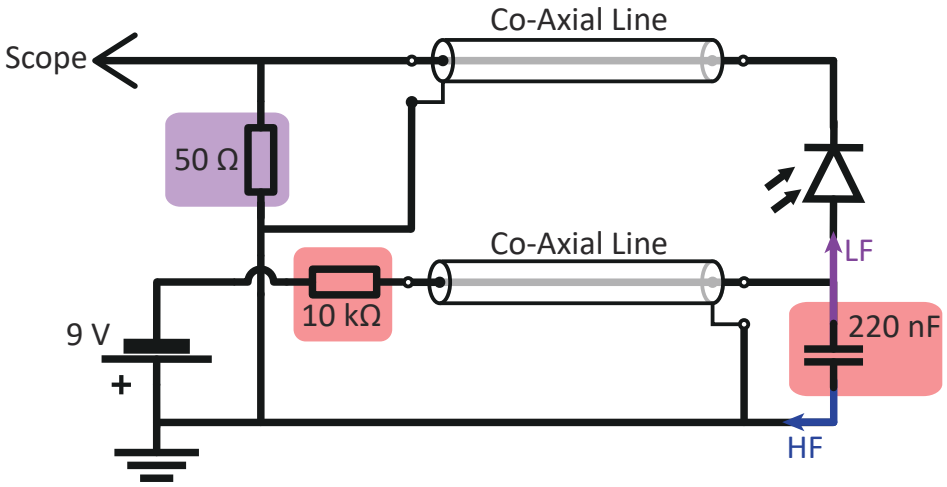

Figure 2.29: A circuit diagram showing the scheme which was used to bias diodes for the work presented in this thesis.

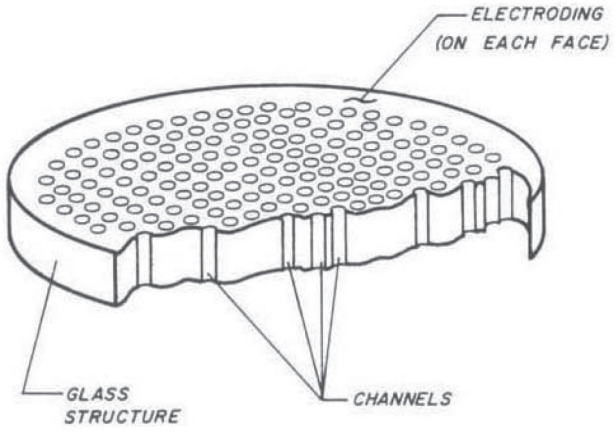

Figure 2.30: A diagram of a microchannel plate, reproduced from [Ladislas Wiza, 1979].

used to produce the plate.

A scematic of a single photomultiplying channel is shown in figure 2.31. These consist of a tube drawn from lead glass, which is treated to make its surface semiconducting and to enhance the emission of secondary electrons. A voltage $\sim 1\,\mathrm{kV}$ is applied to each channel – causing it to work as a photomultiplier. The region of the tube nearest its entrance acts as a photocathode, and the remainder acts as a continuous dynode. The output electrons from each channel are then accelerated across a further potential difference (typically of order $4\,\mathrm{kV}$) and then strike a phosphorescent screen, causing it to fluoresce in the visible. This emission is imaged using either a CCD camera, or film placed directly on the surface of the phosphor. Since the intensity of emission recorded in the image is proportional to the local number of photomultiplying channels which were active during the exposure, the device produces spatially resolved image of radiation intensity incident to the front surface

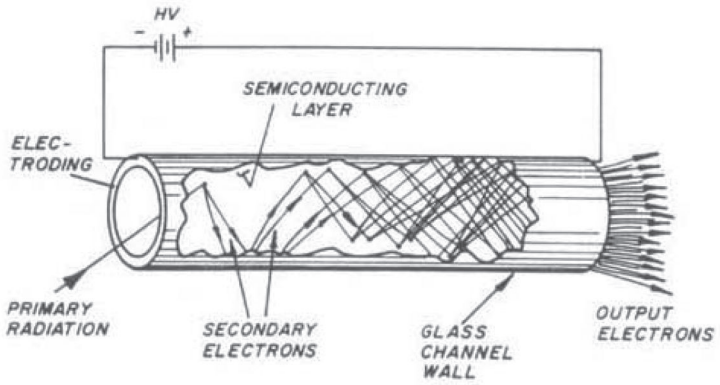

Figure 2.31: A diagram of a single MCP photomultiplying channel. Figure reproduced from [Ladislas Wiza, 1979].

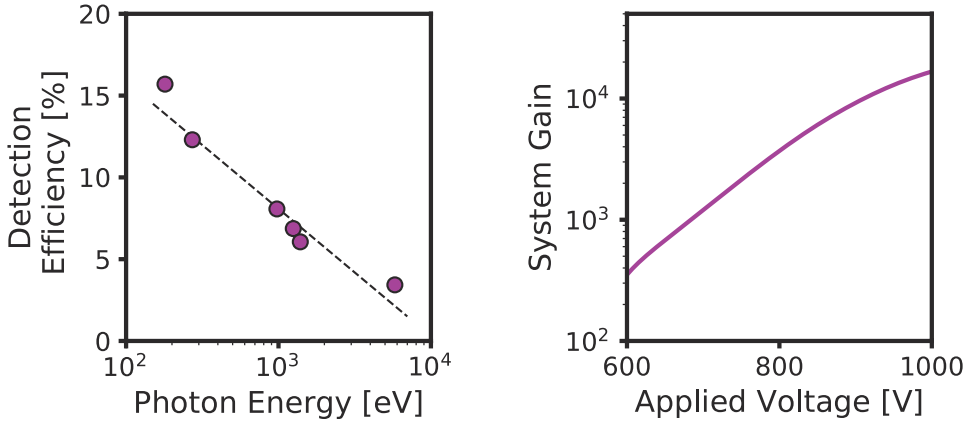

Figure 2.32: *Left:* A plot of X-Ray detection efficiency for an uncoated MCP using data from [Parkes, 1970]. *Right:* MCP gain against applied voltage, using data taken from [Ladislas Wiza, 1979].

of the plate.

MCPs are sensitive to photons with energies in the range $10-10^6$ eV with varying degrees of detection efficiency [Ladislas Wiza, 1979; Parkes, 1970]. Figure 2.32 shows a typical X-Ray response curve. The response for photons with energies $\sim 10\,\text{eV}$ is not shown. In this energy range,detection efficiency is usually around $5-15\%$, but may be enhanced by the vacuum deposition of a high yield photocathode material near to channel entrances.

Figure 2.32 also shows a plot of MCP gain verses applied voltage for a particular configuration, and the general trend which is seen is highly non linear. The precise form of this curve will change between different MCP configurations, but the non-linearity is very typical. This is something which it is useful to bear in mind because a small change in the voltage applied to a plate can cause a detector to move from a regime in which it is completely saturated, to one in which it does not register a signal.

The detectors have been used for XUV/X-Ray imaging in astronomy [Ertley, 2018], as

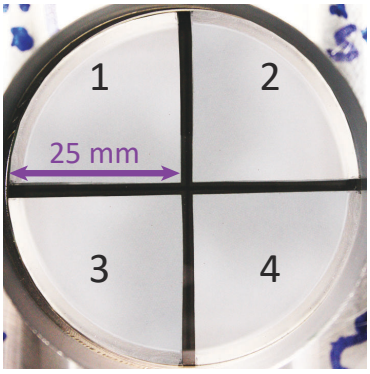

Figure 2.33: A photograph of phosphorescent screen on the rear surface of a four-fame MCP used for experiments on MAGPIE.

well as in HED experiments [Bland, 2004]. To resolve dynamics on the timescales generated in pulsed power driven HED experiments, the MCP bias voltage can be pulsed (width $1 - 50\,\text{ns}$), which provides time gating.

When working with pulsed MCPs, you often run into problems with the dynamic range of measurements. This is the case since photomultiplying channels are fairly resistive – meaning the bias voltage can easily become depleted in response the flow of a photocurrent as the recharge time for a channel is on the same order as the voltage pulse duration. The implication is that the photocurrent induced in the channel is non-linear with respect to number of photons (to the extent where channels almost operate in a regime where they are either inactive or the induced photocurrent is saturated). The intensity on a pixel in the image of the phosphor is therefore set mostly by the number of channels which are active in the region which is imaged onto it. The channel density is low and this limits dynamic range of the measurement.

Micro-Channel Plates Used on MAGPIE

Figure 2.33 shows the phosphorescent screen on the rear surface of an MCP used to diagnose experiments on MAGPIE. As can be seen in the photograph, the plate is divided into four quadrants. These are electrically isolated and can be individually triggered, allowing four time gated images to be captured in a single experiment. The applied voltage pulse duration is 5 ns. The front surface of the plate is coated with a gold layer. The primary purpose of this is to maintain a constant bias voltage across the entire plate however this is likely to also increase the detection efficiency of the device in the $10 - 100\,\text{eV}$ region to some degree. Figure 2.34 is a photo of an assembled MCP detector – this unit is mounted directly to the MAGPIE vacuum chamber during experiments.

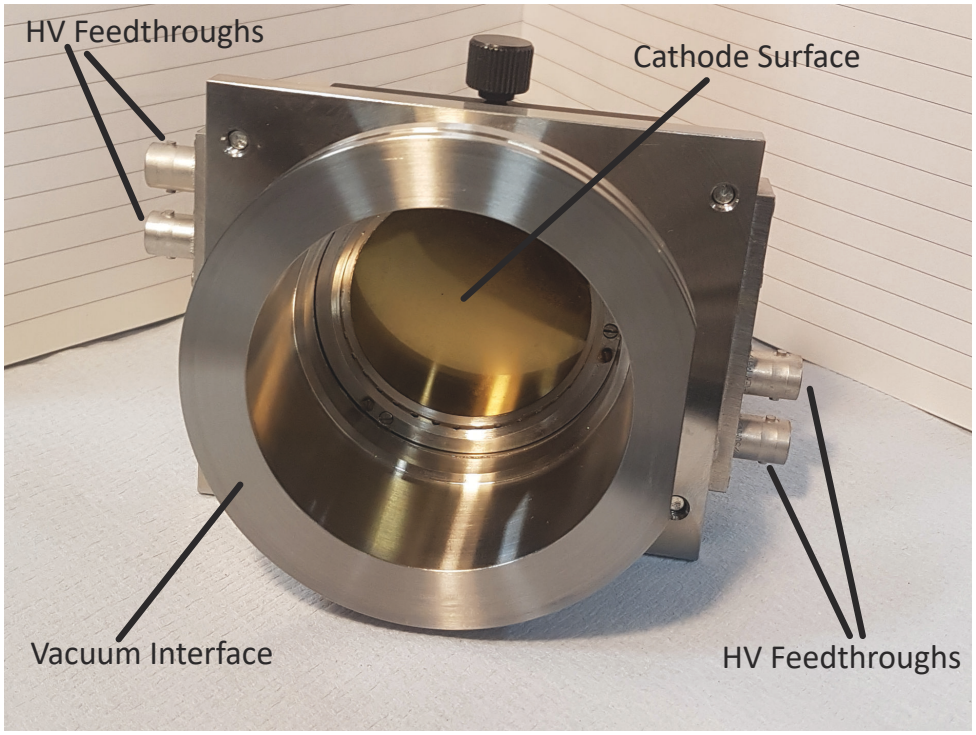

Figure 2.34: A photograph of an assembled MCP detector used for experiments on MAGPIE, showing the vacuum interface used to couple the device to the experimental chamber; the gold coated cathode surface; and the high-voltage (HV) BNC feedthroughs which are used to deliver the voltage pulse to the four quadrants of the detector.

3 Characterisation of Magnetic Reconnection Experiments with Laser Probing Diagnostics

In this chapter I will describe the experimental setup used to study magnetic reconnection on MAGPIE, and give an overview of some key findings which have been made about the system using various optical diagnostics. These measurements will be used to motivate some discussion about the possibility of particle acceleration within the reconnection layer.

3.1 Experimental Setup

Schematically, the experiments make use of two inverse wire arrays which are driven in parallel to produce a system in which magnetic reconnection occurs. This section begins by describing the properties of a single inverse array, and then explains the how fielding two parallel arrays produces reconnecting plasma flows.

3.1.1 The Inverse Wire Array

Figure 3.1 shows a CAD model of an inverse (or exploding) wire array. This is a cylindrical array of wires surrounding a central conductor. The current from a pulsed power generator is directed up through the wires in the array and returns to ground through a central conductor. A measurement of dI/dt is made using Rogowski, positioned on return posts below the array, as shown in the CAD model of the setup.

When a current flows through the array, the wires are resistively heated to form a coronal plasma around each wire core. Simultaneously, the current flowing through the central conductor generates a global, azimuthal magnetic field. The ablated plasma experiences a $\mathbf{J} \times \mathbf{B}$ force due to this magnetic field, and this acts to drive the plasma radially outwards. As the plasma moves, it carries a fraction of the azimuthal magnetic field out with it, frozen into the flow. Hence the array acts as a radially diverging source of plasma which carries an azimuthal magnetic field. The plasma flows persist for the duration of the generator's current pulse (500 ns for experiments on MAGPIE).

The inverse array load geometry was originally used to study the ablation phase of the wires in the array. Historically this was of interest because imploding wire arrays were also known to ablate material for a period before the entirety of the wires' mass imploded onto

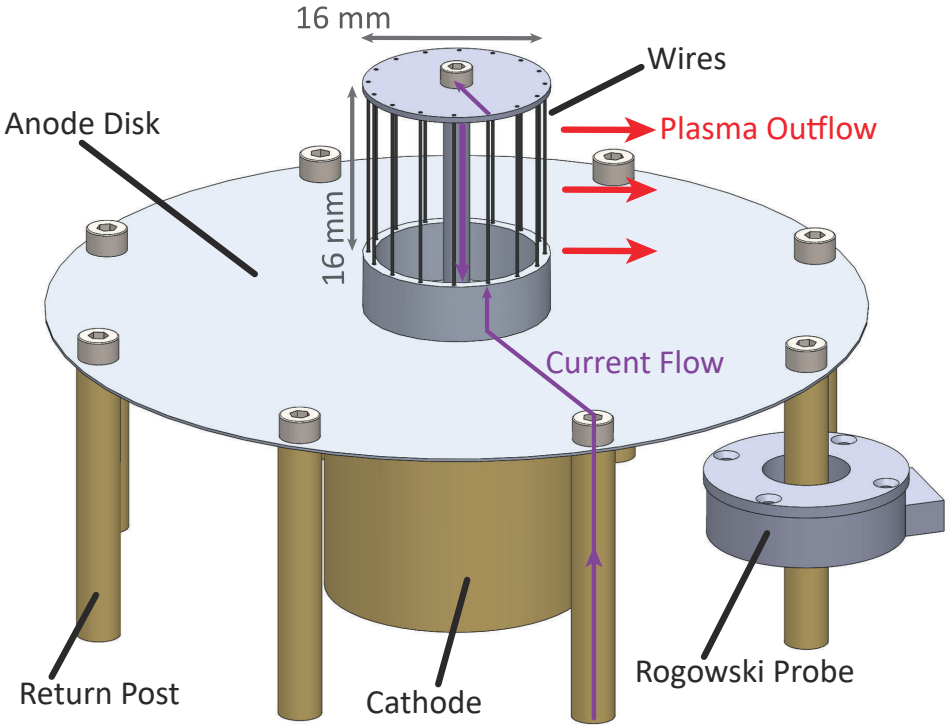

Figure 3.1: A CAD model of an inverse wire array showing the path taken by the current; the direction of plasma outflow; and a Rogowski probe (used to measure the current delivered to the load).

the axis. The ablation has the effect of redistributing material radially before the implosion, and imposes axial perturbations on the stagnated column of plasma – reducing the quality of the X-Ray pulse produced by the implosion.

For the work which is presented here, the wires in inverse arrays were over massed, and this caused the ablation phase to persist for the duration of the driving current pulse. This is an important point – the plasma conditions described here relate to fast but relatively low density plasma outflows produced during the ablation phase of the array. These conditions are very different to the dense, hot plasmas which are produced during the implosion phase in conventional wire arrays.

The radial density profile produced by the ablation phase of an inverse array is well described by the rocket model. This states that

$$n_e(r,t) = \frac{\mu_0 Z}{4\pi v_{out}^2 N_W m_i L_Z}\left[J(t) - \left(t - \frac{r - R_0}{V_{out}}\right)\right]^2, \tag{3.1}$$

where r is distance from the axis; Z is the ionisation of the outflowing plasma; v_{out} is the outflow velocity; N_w is the number of wires in the array; m_i is the mass of ions; L_z is the axial extent of the array; $J(t)$ is the driving current pulse; and R_0 is the radius of the array.

Typical plasma parameters obtained using inverse wire arrays for experiments carried out on Mega-Ampere class pulsed power generators are $n_e \sim 10^{17}-10^{18}$ cm^{-3}, $V_{out} \sim 50$ km s^{-1},

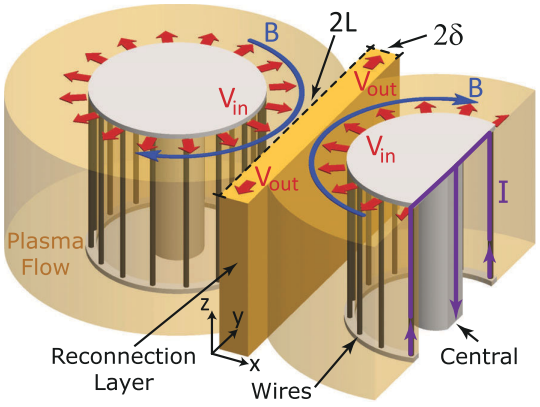

Figure 3.2: Illustration of a pulsed power driven magnetic reconnection experiment. The direction of current flow is drawn in purple; the orientation of magnetic fields are drawn in blue; and the direction of velocities are drawn in red. Figure reproduced from [Hare, 2017b] with permission.

and $B_\phi \sim 1\,\mathrm{T}$. Here B_ϕ is the azimuthal magnetic field frozen into the outflowing plasma.

In summary, inverse wire arrays are radially outflowing sources of high energy density plasma which persist for hundreds of nanoseconds and carry frozen in azimuthal magnetic fields.

3.1.2 Magnetic Reconnection with Two Parallel Wire Arrays

For reconnection experiments, two inverse wire arrays are fielded wired in parallel, to create the configuration shown in figure 3.2. In this setup, the plasma flows from the two arrays collide in a central region and, where they meet, the flows carry oppositely directed embedded magnetic fields. These fields reconnect to from a well defined reconnection layer, where magnetic energy has been observed to be dissipated – heating and accelerating plasma flows in the process. The setup is quasi-2D, but extended in the axial direction, as shown in the figure. The experimental results obtained using this setup are referenced to a co-ordinate system where X denotes the inflow direction; Y denotes the outflow direction; and Z denotes the perpendicular direction (the direction in which the system is broadly invariant).

The setup allows the ion species in plasma flows to be adjusted by changing the material used for the wires in the arrays. This has the effect of changing the rate of radiative cooling, which effects the Lundquist number associated with the system. To date a large number of experiments have been performed using aluminium [Suttle, 2016], and carbon [Hare, 2017b; Hare, 2017a]. The work presented in this thesis was carried out using carbon for the wire material, and so I will limit the discussion in this section to a summary of observations from experiments with carbon wires.

The design of this experimental setup allows for diagnostics to be fielded along two lines of sight. Historically these are referred to as the 'end on' and 'side on' probing directions. In the context of reconnection work, the 'end on' line of sight resolves structure in the reconnection plane, which shown in figure 3.3. The magnetic field lines run parallel to this

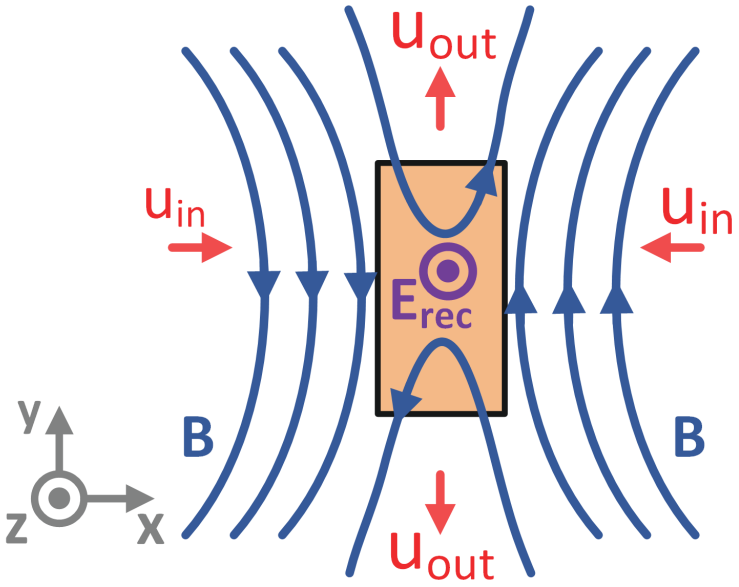

Figure 3.3: Illustrative diagram of the reconnection plane in a pulsed power driven experiment. Diagnostics which are fielded 'end-on' resolve structure within this plane.

plane.

The 'side on' line of sight resolves structure in, what I will refer to as, the perpendicular plane. This is shown in figure 3.4, and is the plane which magnetic field lines are perpendicular to.

3.2 Optical Self Emission Imaging Data

A montage of optical emission images, are shown in figure 3.5. These images were obtained in the same shot and resolve structure in the reconnection plane (shown schematically in figure 3.3). The time for each exposure was 5 ns and the separation between frames

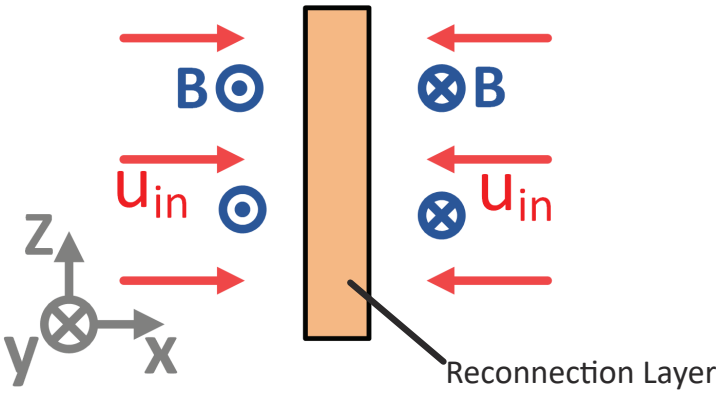

Figure 3.4: Illustrative diagram of the perpendicular plane in a pulsed power driven experiment. Diagnostics which are fielded 'side-on' resolve structure within this plane.

was 20 ns. The time (after current start) for each exposure is indicated in the top left hand corner of each image. When the first image was taken (190 ns after current start) emission is concentrated in jets originating from each wire core, and plasma from the two arrays has not yet collided in the central region. By $t = 250$ ns, the plasma has filled the central region to form a well defined reconnection layer. It is notable that this layer is violently unstable and breaks up to form blobs of plasma which are advected out of the reconnection layer. These have been shown to be plasmoids [Hare, 2017b], and there presence in these conditions is consistent with the semi collisional plasmoid instability [Loureiro, 2016]. In-situ magnetic probe measurements have demonstrated that the plasmoids have an 'O-point' magnetic field topology, and laser interferometry shows that their electron density is enhanced when compared to the rest of the plasma in the layer. From the self emission images, it can be seen that the reconnection layer persists until $t = 410$ ns, with a larger number of plasmoids produced at later times.

3.3 Measurements of Electron Density

Figure 3.6 shows an end on interferogram and the inferred electron density map from a carbon reconnection experiment. The data resolves structure in the reconnection plane (which is shown schematically in figure 3.3). It was captured 240 ns after current start. Laser interferometry is a line integrated diagnostic and the map shown in the figure represents average density, calculated by dividing the areal electron density by the length of the arrays (16 mm). The data shows that the density of plasma in the is initially modulated, due to the fact that the ablation streams originate from individual wire cores, however these modulations have smoothed out by the time plasma reaches the reconnection layer. The average electron density is around $3 \times 10^{17}\,\mathrm{cm}^{-3}$ in the inflow region and $6 \times 10^{17}\,\mathrm{cm}^{-3}$ in the reconnection layer.

The reconnection layer has a uniform structure, with a width of 1.2 mm. The signature of a plasmoid is visible as a blob of plasma with a larger width and enhanced electron density at $y = 5$ mm. In general, the structure seen in this interferogram was reproduced in a large number of reconnection experiments however, whilst plasmoids were observed in every experiment, the time and position of plasmoid formation appeared to be stochastic in nature.

A further (rather striking) feature in the interferometry data is the presence of a region of depleted electron density on the outer edges of the reconnection layer (at $x = \pm 0.7$ mm). The mechanism which supports this depletion region is the subject of ongoing investigation.

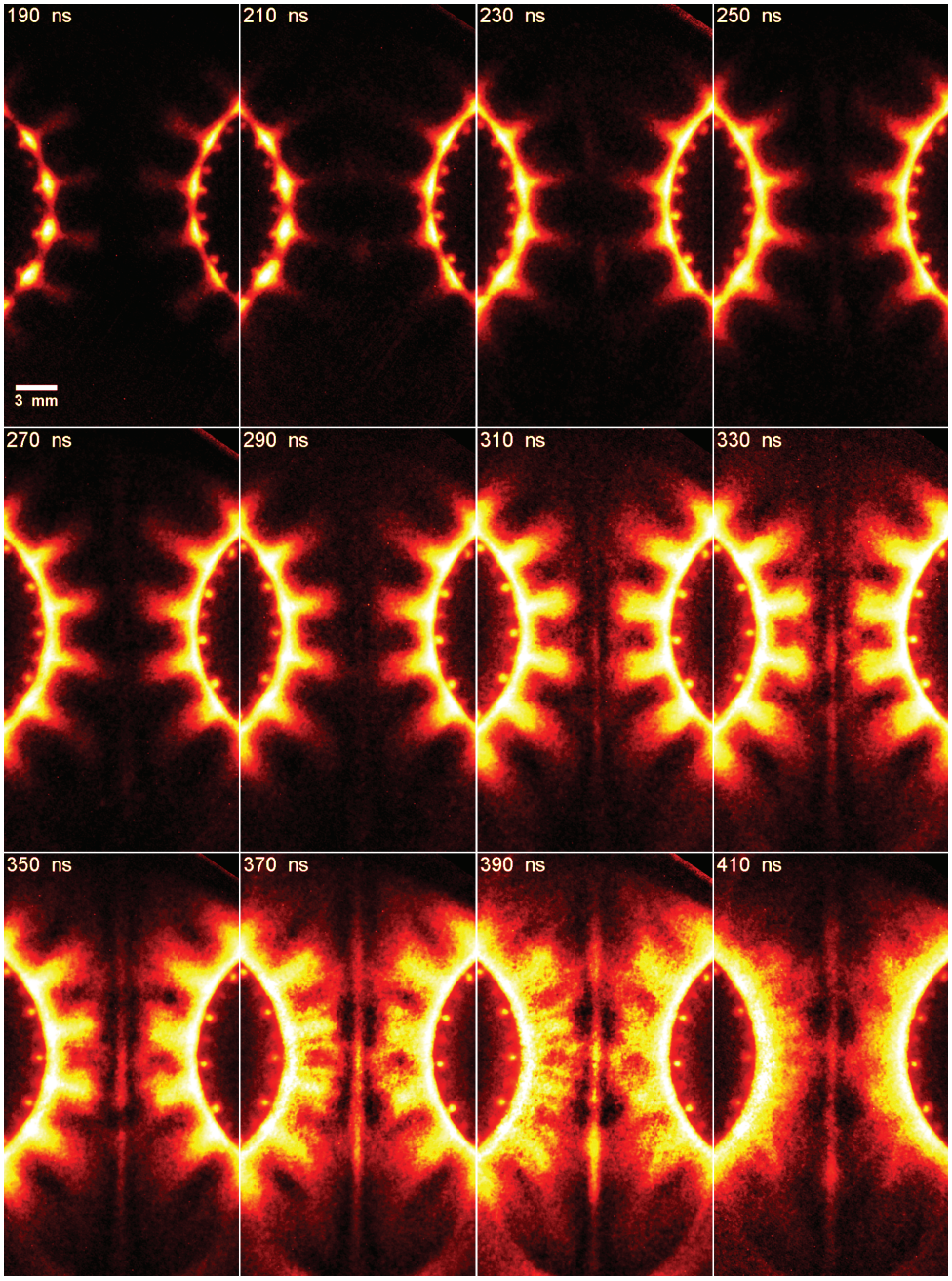

Figure 3.5: A montage of visible self emission images which were captured with a fast framing camera fielded end-on. The images are time integrated over 5 ns, and resolve structure in the reconnection plane. The times shown in the top left of each image indicates the start of the interval over which emission was integrated. An 3 mm scale bar is shown in the first image.

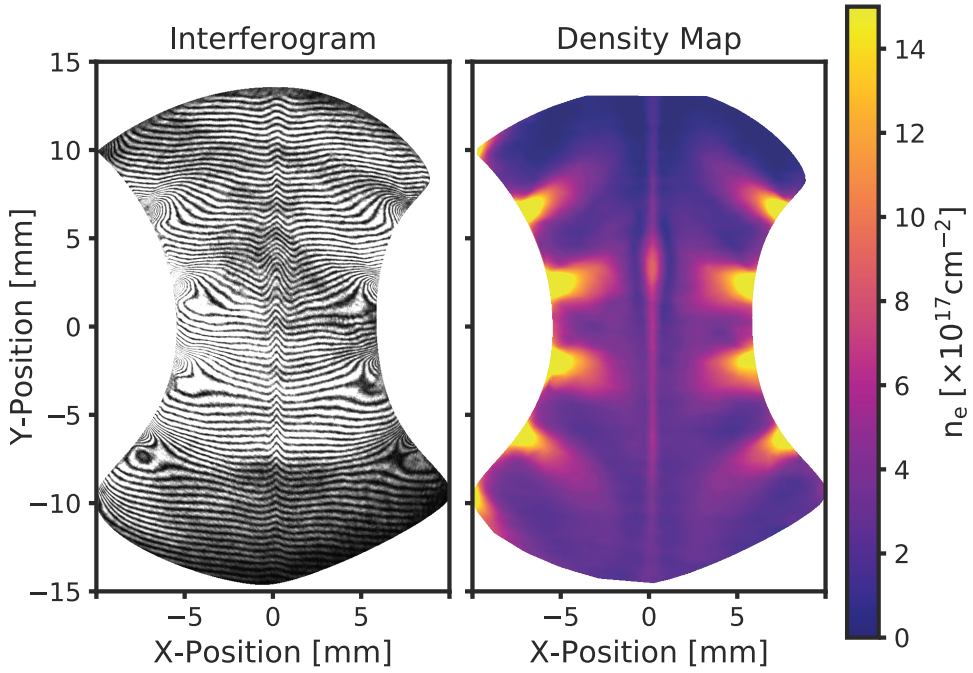

Figure 3.6: End on interferometry data showing average electron density in the reconnection plane. The interferogram was captured 240 ns after current start.

3.4 Temperature and Velocity Measurements

In order to diagnose temperatures and velocity profiles within the reconnection plane, optical Thomson scattering measurements of the ion-acoustic feature were performed. The scattering geometry used for these measurements is shown in figure 3.7. As the figure shows, the focussed Thomson probe was passed through the experiment at 22.5 deg to the reconnection layer. Two linear fiber arrays were used to collect scattered light from 14 collection volumes. The bundles were positioned at 45 deg and 135 deg to the probe. Observing scattered light from two orientations meant that two separate velocity components could be inferred from the data. The temperatures measured from different observation directions were also cross checked to ensure consistency.

The central panel in the image shows raw data from the spectrometer's CCD. Scattered light from the 14 fibers are visible as separate spectra, dispersed along the spatial axis of the spectrometer. Example profiles of scattered light are shown in the right hand panel of the figure. The top plot shows a profile from the inflow region and the bottom plot is from a volume located in the reconnection layer. The fitted Thomson scattering profile is shown in red. Both of the spectra are dominated by the ion acoustic feature however the typical double peak structure one usually associates with this feature is not seen. This is indicative of the fact that ions are significantly hotter than electrons in this experiment.

Figure 3.8 shows plasma parameters obtained from Thomson scattering spectra as a function of the X coordinate of each scattering volume. The top plot shows values of

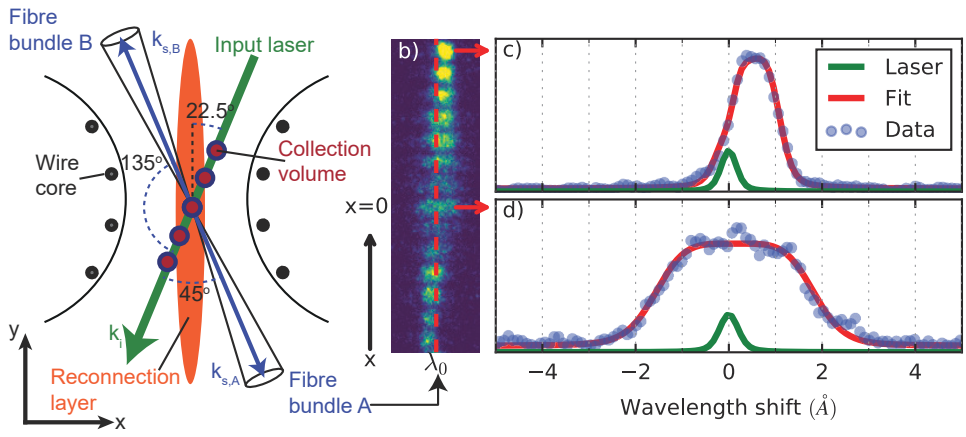

Figure 3.7: *Left:* Diagram showing the scattering geometry used to obtain the Thomson scattering data presented below. As described previously, scattered light is imaged onto a linear array of fiber optics, so data from 14 spatially resolved scattering volumes is captured in each experiment. Light was collected simultaneously from two scattering directions using separate fiber arrays. *Center:* Raw data from the Thomson scattering spectograph. The spectra is spatially resolved in the vertical direction and light from the 14 of the 28 fibers can be seen at different locations. *Right:* A Thomson scattering spectrum from the inflow region is shown in the upper plot, and a spectrum from the reconnection layer is shown in the lower plot. Figure reproduced from [Hare, 2017a] with permission.

T_i and ZT_e and the bottom plot shows values of the measured inflow velocity (i.e. the X component of velocity). Self consistent values of Z and T_e were calculated from the Thomson scattering data using the atomic physics code SpK, and the inferred electron temperatures are shown in figure 3.9.

The trend which is seen in Thomson scattering data is that the inflow velocity is around $50\,\mathrm{km\,s^{-1}}$ far from the layer, but reduces to zero near the layer's centre. Although this is not shown in the plot, the outflow velocity (i.e. Y component of velocity) is small in the inflow layer but increases to $130\,\mathrm{km\,s^{-1}}$ within the layer. This acceleration of bulk plasma flow is a a signature of the reconnection process. The plasma in the inflow region is relatively cold ($T_e = 15\,\mathrm{eV}$, $T_i = 50\,\mathrm{eV}$) but plasma in the reconnection later is heated to much larger temperatures ($T_e = 100\,\mathrm{eV}$, $T_i = 600\,\mathrm{eV}$). This plasma is heating is a further signature of magnetic reconnection – magnetic energy is being converted into energy associated with degrees of freedom within the plasma.

The measured parameters puts the equilibration time between electron and ion species ($\tau^E_{e/i}$) at 100 ns in the inflows and 600 ns in the reconnection layer so in some sense the separation between electron and ion temperatures is something which can be supported by the system. The physical reason for preferential ion heating is the subject of ongoing work. It is interesting to note that, in the layer, $T_i \approx ZT_e$ so the plasma ends up in a state where thermal energy is equally divided between the two species.

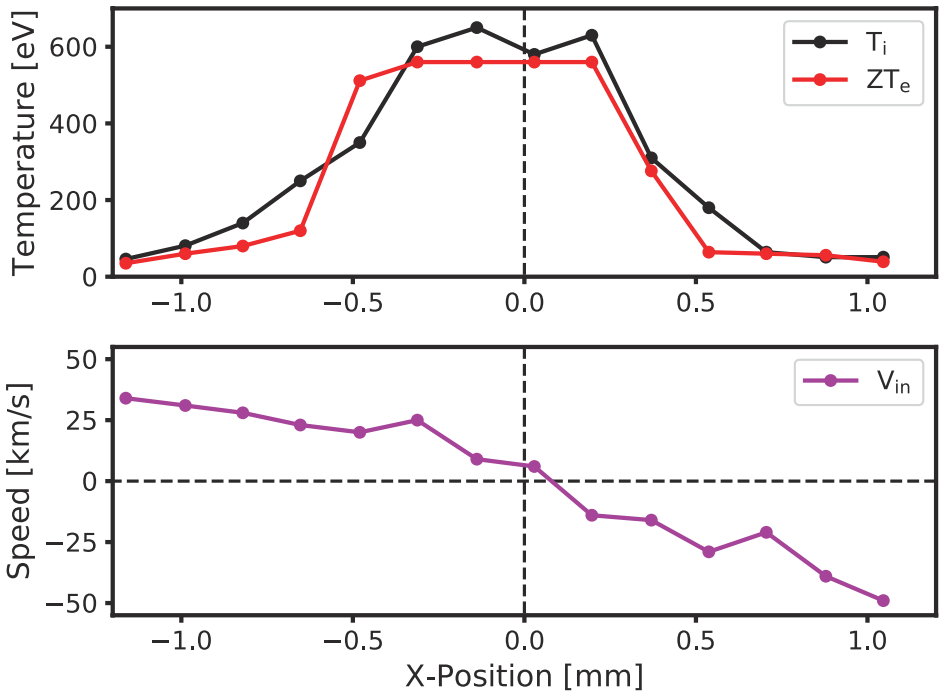

Figure 3.8: Plasma parameters obtained from Thomson scattering data. The top plot shows measured values of ZT_e and T_i. The bottom plot shows the measured inflow velocity, denoted V_{in}.

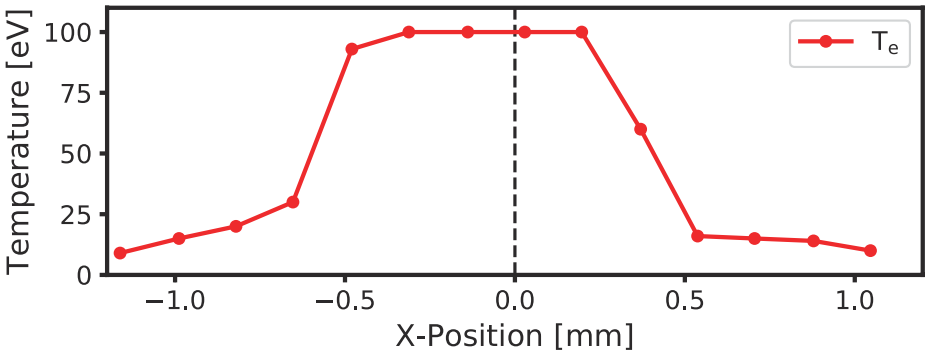

Figure 3.9: Values of T_e inferred from the measured values of ZT_e and n_e, using the atomic physics code SPK [Chittenden, 2016]. The charge state is around 4 in the inflow region, and 6 in the reconnection layer.

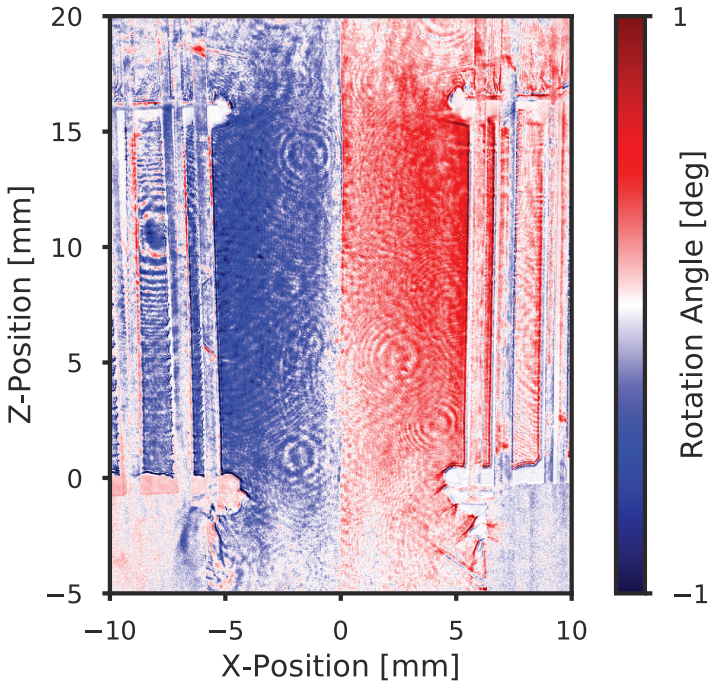

Figure 3.10: A side on polarogram, showing the rotation applied to a linearly polarised laser beam by magnetic fields embedded in the plasma inflows. The applied rotation is in opposite directions for the two inflows which is indicative of the fact that they carry oppositely directed magnetic fields.

3.5 Measurements of Magnetic Field Strength

The MAGPIE Faraday rotation diagnostic probes experiments side on so, for a reconnection experiment, structure is resolved in the perpendicular plane (shown schematically in figure 3.4). Figure 3.10 is a polarogram from a reconnection experiment, captured 251 ns after current start. The outline of the two wire arrays are visible at $x = \pm 5$ mm. In the region of the plasma inflow, a maximum rotation of ± 0.8 deg is applied to the probe beam. The plasma ablated from the two arrays acts to rotate the light in opposite directions and this is indicative of the fact that the inflowing plasmas carry oppositely directed magnetic flux.

The picture shown in the polarogram can be made more quantitative by using the information provided with an interferometer that uses the same probing laser beam. It is worth restating that this gives you measurement of a *weighted* average magnetic field strength:

$$B_{y,\,\mathrm{av}}(x,z) = \frac{\int B_y(x,y,z) n_e(x,y,z) dy}{\int n_e(x,y,z) dy}. \tag{3.2}$$

Figure 3.11 shows a profile of weighted average magnetic field obtained from the polarogram in figure 3.10. The experimental data was fit with a Harris Sheet model, under which B_y

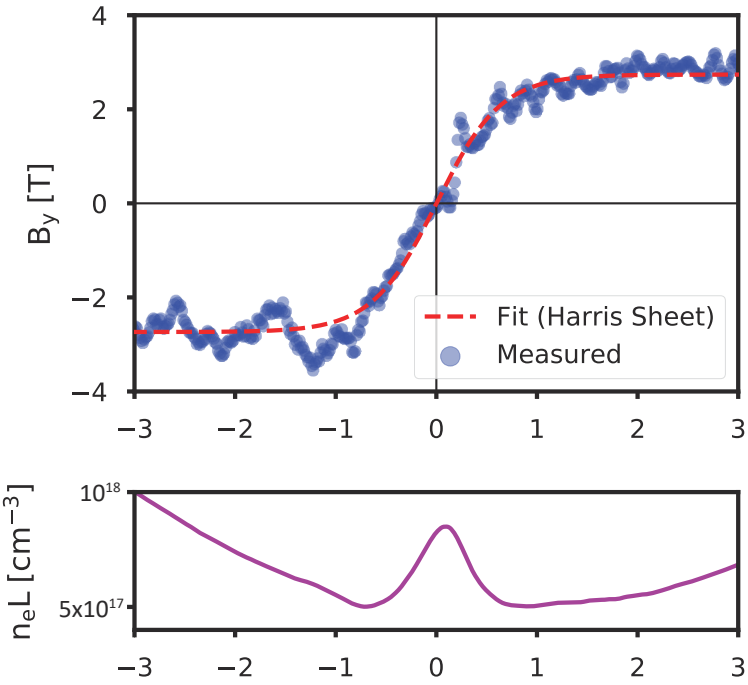

Figure 3.11: *Above:* Weighted average magnetic field profile obtained from simultaneous polarimetry and interferometry data, showing that magnetic flux is annihilated within the layer. *Below:* Line integrated electron density profile obtained from interferometry data.

(the y-component of magnetic field is given by)

$$B_y(x) = B_0 \tanh\left(\frac{x}{\Delta}\right), \tag{3.3}$$

where B_0 is the inflow field strength and Δ is the half-width of the layer. The values of these parameters obtained from the fit were $B_0 = 3\,\mathrm{T}$ and $\Delta = 0.6\,\mathrm{mm}$.

3.6 Summary of Conclusions Drawn from Experimental Measurements

A summary of the key results from the measurements which are presented in this section are shown in table 3.1. Values of a few quantities which are relevant to the physical interpretation of these results are shown in table 3.2. For these derived quantities the system length scale, (L) was taken to be 16 mm which is the twice the radius of magnetic curvature in the inflows.

The values show that the dynamic plasma beta (β_{ram}) in the inflows is ~ 1, and that plasma inflows are subsonic. The observation of plasmoid formation in these conditions is constant with the semi-collisional regime theory, as described in [Loureiro, 2016].

Parameter	Inflow Region	Reconnection Layer
B_y	3 T	0 T
n_e	$3 \times 10^{17}\,\mathrm{cm}^{-3}$	$6 \times 10^{17}\,\mathrm{cm}^{-3}$
V_{in}	$50\,\mathrm{km\,s}^{-1}$	–
V_{out}	–	$130\,\mathrm{km\,s}^{-1}$
T_e	15 eV	100 eV
T_i	50 eV	600 eV
$\bar{Z}$	4	6

Table 3.1: Summary of plasma parameters measured in carbon reconnection experiments.

Parameter	Inflow Region	Reconnection Layer
Alfvén Speed $[V_A]$	$50\,\mathrm{km\,s}^{-1}$	–
Sound Speed $[C_S]$	$30\,\mathrm{km\,s}^{-1}$	$85\,\mathrm{km\,s}^{-1}$
Alfvén Time $[\tau_A]$	100 ns	–
Ion inertial length $[c/\omega p, i]$	–	2 mm
Lundquist Number $[S]$	120	–
Thermal Beta $[\beta_{th}]$	0.4	–
Dynamic Beta $[\beta_{ram}]$	1	–

Table 3.2: Summary of quantities derived from measured plasma parameters.

3.6.1 Particle Acceleration and Collisionality

The results presented in this section can be used to make some basic statements about the possibility of generating fast particles in reconnection experiments.

If it is assumed that the reconnection process is steady state, and the geometry of the system is two dimensional then a spatially invariant, in out of plane electric field is required to support the reconnection processes [Priest, 2000, p. 121]. Ohm's law states

$$\mathbf{E} + \mathbf{V} \times \mathbf{B} = \eta \mathbf{j}, \tag{3.4}$$

where $\mathbf{E}$ is the electric field; $\mathbf{V}$ is plasma velocity; $\mathbf{B}$ is the magnetic field; η is the plasma resistivity; and $\mathbf{j}$ is the current density. If the plasma inflows are ideal[1], then in the inflow region the reconnecting electric field is supported entirely by the motional term in Ohm's law and so is given by

$$\mathbf{E}_{\mathrm{rec}} = -\mathbf{V_{in}} \times \mathbf{B_{in}}. \tag{3.5}$$

The electric field in the centre of the current sheet is supported entirely by current flow, but is of equal magnitude. Using the values of $\mathbf{B_{in}}$ and $\mathbf{V_{in}}$ shown in table 3.1 yields $E_{\mathrm{rec}} = 1.5\,\mathrm{kV\,cm}^{-1}$.

As discussed in section **??**, a proposed mechanism for particle acceleration in reconnection is the direct acceleration of electrons by the reconnecting electric field. The idea behind

[1] This is a valid assumption for MAGPIE reconnection experiments as the Lundquist number (which is the same thing as the inflow magnetic Reynolds number) is much greater than unity.

this mechanism is that electrons in the inflow region are magnetised and so are localised in the Z-direction. As they move into the reconnection layer, the in-plane magnetic field drops to zero and so they become magnetised. This means they are no longer localised in the axial direction and so may be accelerated by E_{rec}. In the absence of collisions, the energy gained is given by $eE_{\text{rec}}L_Z$, where L_Z is the total distance an electron travels. Side on interferometry measurements show that in reconnection layer has a perpendicular length of 1.6 cm, and so one expects the fastest accelerated electrons to have an energy of 2.4 keV.

This result assumes that electrons do not experience collisions within their period of acceleration. As discussed previously, the Dreicer treatment [Dreicer, 1959] provides a means to estimate the fraction of electrons that have an initial speed which is large enough for this assumption to be valid, assuming an initially Maxwellian electron velocity distribution. The fraction of electrons which are fast enough is given by

$$f = \exp\left(-\frac{E_D}{2E_{rec}}\right), \tag{3.6}$$

where E_D is the Dreicer field, given by

$$E_D = \frac{Ze\ln\Lambda}{4\pi\epsilon_0\lambda_D^2}. \tag{3.7}$$

Here Z is ionisation state; λ_D is the Debeye length; and $\ln\Lambda$ is the Colomb logarithm [Priest, 2000, p. 466]. Using the expression for $\ln\Lambda$ given in [Richardson, 2019], and the measured plasma parameters quoted above yields $E_D = 71\,\text{kV}\,\text{cm}^{-1}$. This implies that the fraction of accelerated particles, $f = 5 \times 10^{-11}$.

From measurements of electron density, inflow velocity, and layer morphology; the total flux of electrons into the reconnection layer is around $8 \times 10^{15}\,\text{ns}^{-1}$. The fraction of these which a Dreicer treatment suggests will be accelerated is $4 \times 10^{5}\,\text{ns}^{-1}$. If the characteristic energy of a fast electron is taken to be 2 keV, then the total power carried by the fast electron current is 0.1 W. The total energy carried by fast electrons during the current pulse ($t = 500$ ns) is 50 nJ. By comparison, the power carried in the magnetic fields within the inflow region, calculated from the measured magnetic field strength, inflow velocity, and experimental setup geometry is around 20 MW.

These results suggest that any contribution from fast particles ought to be both energetically insignificant and undiagnosable. However, as I will discuss in the following section, early experimental observations suggested that an energetic electron was occurred in the reconnection layer. Furthermore, the argument outlined above assumed that the reconnection process was in steady state but experimental measurements had demonstrated that the current sheets produced with the setup were plasmoid unstable and so the local strength reconnecting electric field had the potential to differ significantly from the steady state value quoted above. Therefore a series of experiments which were focussed on diagnosing fast particles generated by magnetic reconnection. It was hoped that the results from these

experiments would be helpful to obtain insight about the fundamental processes underlying particle acceleration in magnetic reconnection.

4 Experimental Results

In the earliest reconnection experiments which were performed on MAGPIE, it was observed that the anode plate (positioned beneath the experiment) sustained a pattern of damage which correlated with the position and size of the reconnection layer. An example of what we seen is shown in figure 4.1. This image was obtained in a later experimental campaign where a tungsten witness plate was positioned below the arrays, however similar damage was caused to stainless steel hardware in earlier experiments. The figure shows that the damaged region is extended in the Y-direction; centred on $X = 0$ mm; and has a characteristic width of order 1 mm. Members of the MAGPIE team had previously observed similar patterns of wear in hardware which was placed in the path of electron beams with characteristic energies in the range $1 - 10$ keV, generated in imploding wire array Z-pinch experiments.

It was hypothesised that the damage observed in reconnection experiments was also caused by an electron beam and that this beam was generated by the direct acceleration of thermal electrons in the reconnection layer by the reconnecting electric field, which would direct electrons towards the anode.

In order to investigate the possibility of electron acceleration more quantitatively, a series of experiments were performed in which X-Ray self emission from witness plates positioned below the reconnection layer was diagnosed by a variety of different diagnostics. As shown in figure 4.2, if an electron beam was generated then it would strike this target, producing a X-Ray spectrum characteristic of the target material. By diagnosing spectra it was hoped that it would be possible to determine if an electron beam was produced, and if so, infer beam properties such as characteristic energy and hot electron current.

4.1 Spectrally resolved measurements of X-Ray emission from an angled target

To make spectrally resolved measurements of emission from the target, a focussing spectrograph with spatial resolution (FSSR) was fielded. This used a spherically bent Bragg-Crystal made from Mica (R = 186 mm, 2d = 6.687 Å) – more details can be found in section 2.3.2. The instrument's spatial axis was aligned with the Z-axis of the experiment, such that the spectral axis corasponded to the X-axis of the experiment. It was used in conjunction with a spectral target which was angled at $\sim 30°$to the X-Y plane of the experiment, as shown in figure 4.3, in order for the target to present some surface area to the diagnostic. For all of the experiments in which a spectrometer was fielded, the target material

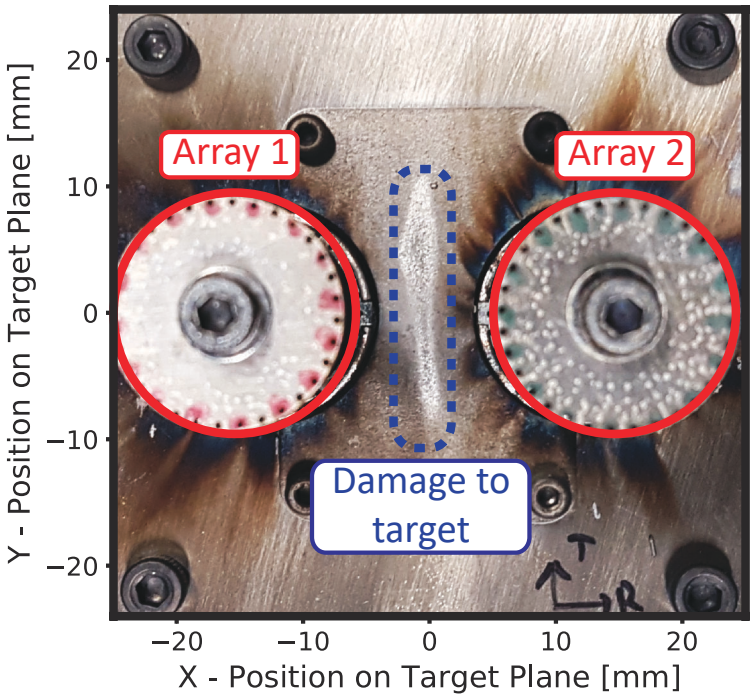

Figure 4.1: Photograph of a tungsten witness plate positioned below the two wire arrays in a pulsed power driven magnetic reconnection experiment. The image was taken after a shot, and shows damage to a region of the target which is extended in the Y-direction and is centred on the line $X = 0$. The width of the damaged region is of order 1 mm. The appearance and position of this region are consistent with the damage caused by an electron-beam generated in the reconnection layer.

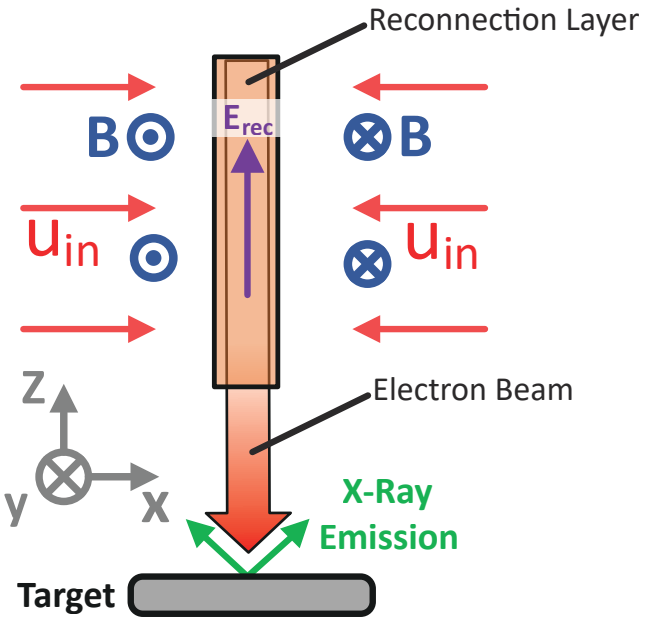

Figure 4.2: Diagram of an experiment designed to diagnose electrons accelerated by the reconnecting electric field, showing the direction of magnetic fields and velocities of the inflowing plasma; the direction of the reconnecting electric field; and the position of a metal target which emits a characteristic X-Ray spectrum.

was aluminium. This material was chosen because the characteristic energy of aluminium $K\alpha$ emission is 1.4 keV, which is simmilar to the expected energy of accelerated electrons (~ 2 keV).

Figure 4.4 shows the meridional plane geometry of the FSSR setup used in experiments. The orientation of the crystal was set to so that the centre angle (denoted φ_c in the figure) was 34°. This angle was chosen satisfy the Bragg condition for aluminium $K\alpha$ emission in the second order ($\lambda_c = 8.34$ Å and $n = 2$, where λ_c is the central wavelength). As shown in the figure, the point on the image plane where λ_c was imaged lay *inside* the Rowland circle and so the setup resolved spatial features in the spectral direction (albeit with significant demagnification). It would have reduced ambiguity in the interpretation of data if λ_c was imaged *onto* the Rowland circle but the spectrometer was designed to be as compact as possible in order to allow it to be fielded alongside other diagnostics, at a small cost to the quality of the experimental data.

The FSSR recorded time integrated spectra onto image plate (Fujifilm BAS-TR). The data was scanned using a BAS-1800 II image plate scanner. An example of a spectrum obtained in a reconnection experiment is shown in figure 4.5. Similar results were obtained repeatably in 5 separate reconnection experiments.

The spectrum contains three prominent spectral features. The first of these is a single peak which is indicated with a dashed red line in the figure. This was identified as the

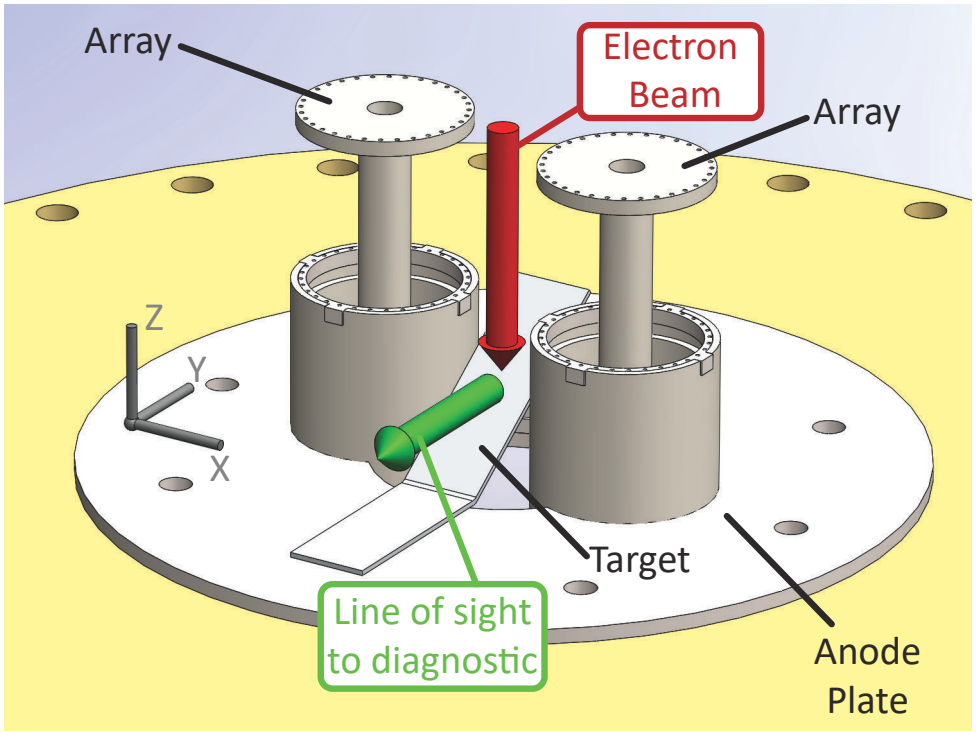

Figure 4.3: CAD drawing of the load hardware used for experiments in which a FSSR was fielded, showing the position of wire arrays; an angled target; the orientation of the electron beam; and the direction of the spectrometer's line of sight. The wires in the exploding arrays are not shown.

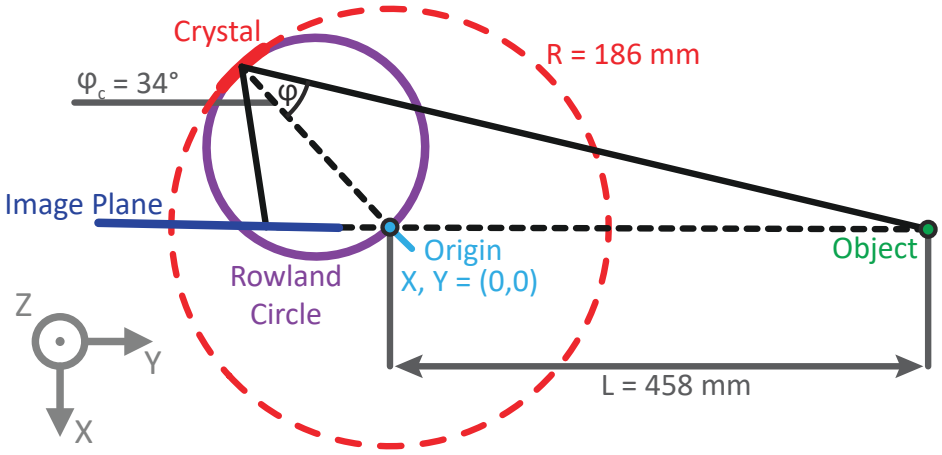

Figure 4.4: Diagram looking down onto the meridional plane of the FFSR, corresponding to the X-Y plane of the experiment. The Bragg crystal was made from spherically bent Mica (R = 186 mm); the length L (distance between the object and the origin) was 458 mm; and the central angle [φ_c] was 34°. Figure adapted from [Pikuz, 2008].

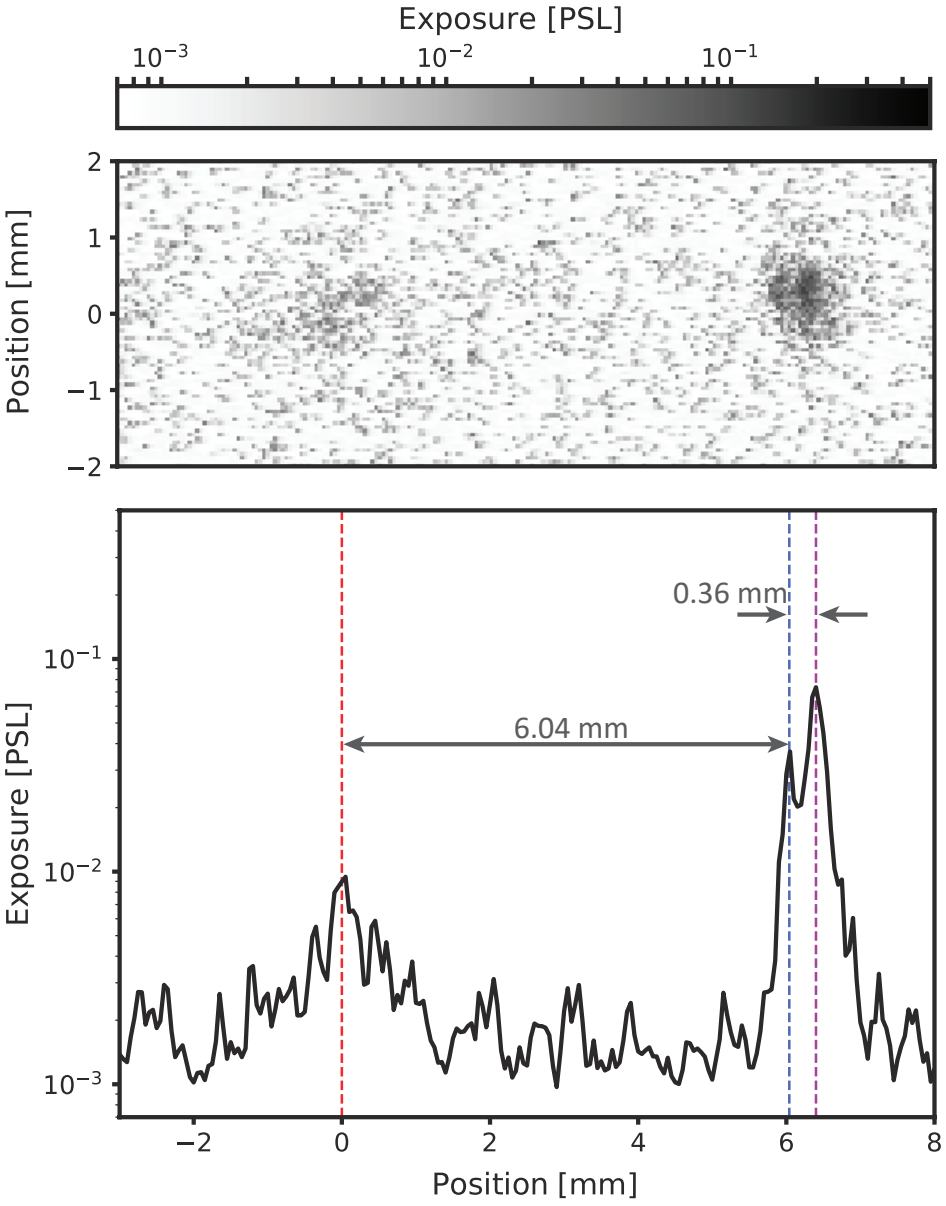

Figure 4.5: *Above:* Raw image plate data showing data from the FSSR in s0517_17. The X-axis corresponds to the spectral axis of the instrument. The Y-Axis corresponds to its spatial axis. *Below:* A profile line along $Y = 0\,\text{mm}$, with a width of $0.5\,\text{mm}$ from the image plate data shown above. The spectrum contains aluminium and chromium $K\alpha$ emission lines. For aluminium, the $\Delta\lambda$ between the $K\alpha_1$ and $K\alpha_2$ lines is below the resolution of the spectrometer and the position of their combined peak is indicated with a dashed red line. For chromium, the position of the $K\alpha_1$ peak is indicated with a magenta dashed line and the position of the $K\alpha_2$ peak is indicated with a blue dashed line. On the X-axis, $0\,\text{mm}$ is the position of the red dashed line, and *not* the origin in figure 4.4.

combined emission from aluminium $K\alpha_1$ and $K\alpha_2$ emission from the target. These lines are separated by just 0.002 Å, a difference which was obscured by line broadening and the resolution of the instrument. The other two features were identified as chromium $K\alpha_1$ (indicated with a magenta dashed line) and chromium $K\alpha_2$ (indicated with a blue dashed line).

The presence of spectral features associated with chromium can be explained by the fact that the majority of the load hardware used in experiments was made from stainless steel. This is an iron alloy, with a chromium content $\sim 15\%$ of total mass [Moore, 2009, p. 18]. Because stainless steel was not localised to the region below the reconnection layer, it cannot be determined if the mechanism by which these lines were excited can be associated with energetic electrons produced via magnetic reconnection. If fact, it seems more likely that these features were produced directly by the pulsed power drive.

A potential source of a fast electron beam may be found at the start of the voltage pulse before the establishment of magnetic insulation in the arrays. In the absence of this insulation, electrons emitted by the electrodes are essentially free to accelerate across the anode cathode gap and excite X-Ray emission when they collide with the surface of the anode. When the current flow is established the gap is magnetically insulated and so the X-Ray emission will cease. Members of the MAGPIE team have observed transient X-Ray emission from load at early times in historic experiments with imploding wire arrays and have attributed their presence to this effect. The presence of chromium lines in recorded spectra proved beneficial as a fiducial to line up the spectral axis of image plates from different experiments.

The treatment outlined in [Pikuz, 2008] was used to calculate the spectral band function of the spectrometer numerically. Figure 4.6 is a plot of this function. It shows that the expected separation between the two chromium $K\alpha$ peaks is 0.35 mm which is in excellent agreement with the separation of 0.36 mm which was seen in the measured spectrum.

The expected separation between the aluminium $K\alpha$ lines and the chromium $K\alpha_2$ line is 6.68 mm, which is larger than the measured separation by 0.64 mm. This discrepancy can be explained in part by the relatively large uncertainty in the position of the aluminium $K\alpha$ peak position, of around 0.5 mm, due to the poor signal to noise ratio. The remainder of the disagreement can be attributed to the result of a slight misalignment of the Bragg crystal in the setup, which would alter the form of the spectral band function.

There is no meaningful way to compare the intensity of aluminium and chromium $K\alpha$ features because the reflectivity of mica changes significantly between different orders of reflection, and these changes are not well documented [Pikuz, 2016]. Figure 4.7 shows the measured chromium $K\alpha$ doublet plotted on a linear intensity scale in order to highlight the intensity ratio between the two peaks. As can be seen in the figure, the ratio $K\alpha_2$ to $K\alpha_1$ intensity is given by $0.037/0.074 = 0.50$. This is in good agreement with the expected $K\alpha$ intensity ratio for chromium, which is also 0.5 [Dyson, 1990, p. 79].

In summary, results obtained from a FSSR fielded on magnetic reconnection experiments

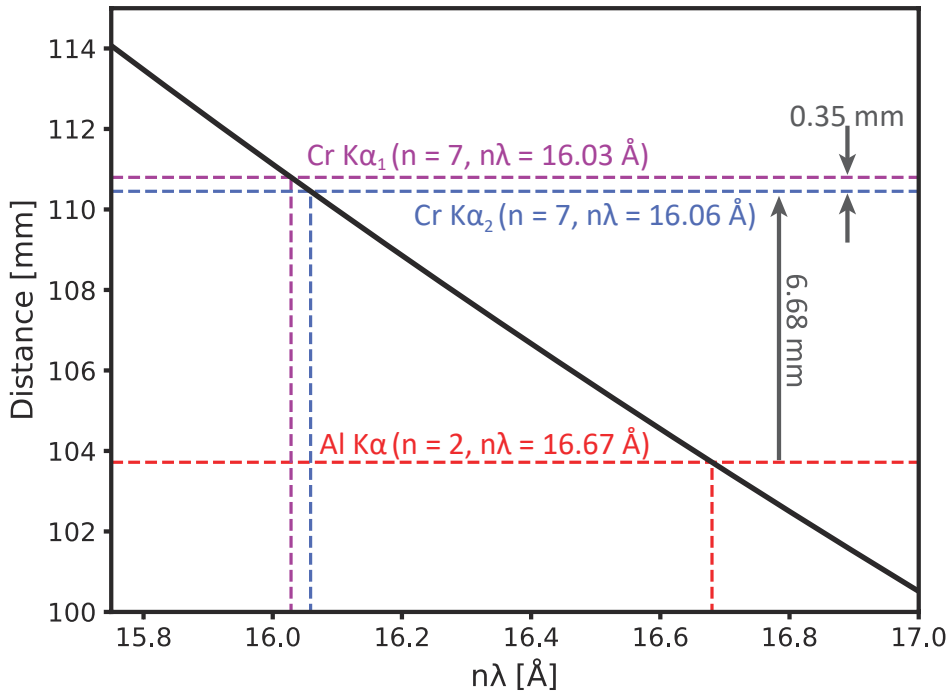

Figure 4.6: Plot showing distance from the origin in figure 4.4 as a function of nλ in the range $15.8 - 17.0$ Å. The points on the curve cosponsoring to the Al $K\alpha$, Cr $K\alpha_1$, and Cr $K\alpha_2$ emission lines are shown in red, blue, and magenta respectively.

showed signatures of aluminium $K\alpha$ emission from an angled aluminium target placed below the reconnection layer and chromium $K\alpha$ emission which was not localised to the region below the reconnection layer and was assumed to be a signature of the pulsed power drive.

The presence of aluminium $K\alpha$ features in the measured spectra was interesting because it indicated that energetic electrons produced in the reconnection layer were colliding with the target and collisionally ionising aluminium K-Shell electrons. As discussed in section **??**, this requires that electrons have kinetic energies $1 - 4$ times the aluminium K-shell ionisation energy, which is 1.6 keV. In section **??**, it was shown than Thomson Scattering measurements of the reconnection layer indicated that typical electron temperatures were an order of magnitude smaller at around 100 eV. Therefore the presence of aluminium $K\alpha$ emission in the measured spectra suggested that a non-thermal electron population (which Thomson Scattering was insensitive to) existed within the reconnection layer.

4.2 Time integrated self emission images of X-Ray Emission from a flat target

The spectra obtained in experiments with an FSSR were encouraging as they indicated there was an energetic electron population within the reconnection experiment, but quantitatively interpreting these results was problematic: Only a single aluminium emission line was

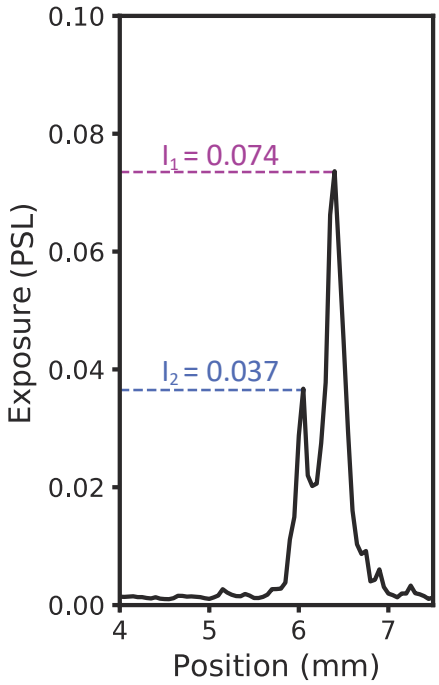

Figure 4.7: The same Chromium $K\alpha$ doublet as in figure 4.5 plotted on a linear intensity scale in order to highlight the intensity ratio between the two peaks. The ratio $I_2/I_1 \approx 0.5$. This is expected for $K\alpha$ emission from mid-Z elements [Dyson, 1990, p. 79].

present in the measured spectra, and it was not clear how to obtain information about the characteristic energy of the hot electrons; or what fraction of the total population was non thermal; or the mechanism by which these particles were accelerated from a single spectral feature. In addition to this, from laser probing measurements, it was known that the reconnection setup produced a system with a complex, spatially varying structure so it was necessary to make measurements which were spatially resolved in order to verify that hot electrons were produced within the reconnection layer and not the plasma inflows.

To address some of these issues, a series of experiments were performed with a four frame, time integrating X-Ray pinhole camera which was fielded to spatially resolve target emission corresponding to structure in the reconnection plane. In these experiments a target was placed below and parallel to the reconnection plane was used, as shown in figure 4.8. The main reason for moving towards a flat target design was a desire to ensure that the position of the target did not change between experiments. These flat targets were much easier to make than the angled targets used for experiments with the FSSR, and so they could be positioned in a more repeatable fashion.

The time integrated pinhole camera experiments recorded data onto Fujifilm BAS-TR image plate. In the period between the time when experiments using the FSSR and the time when the experiments discussed in this section were performed we purchased a Fujifilm FLA-5000 image plate scanner, which was used to scan pinhole imaging data. This significantly improved the signal to noise ratio in the data compared to the FSSR image plate data.

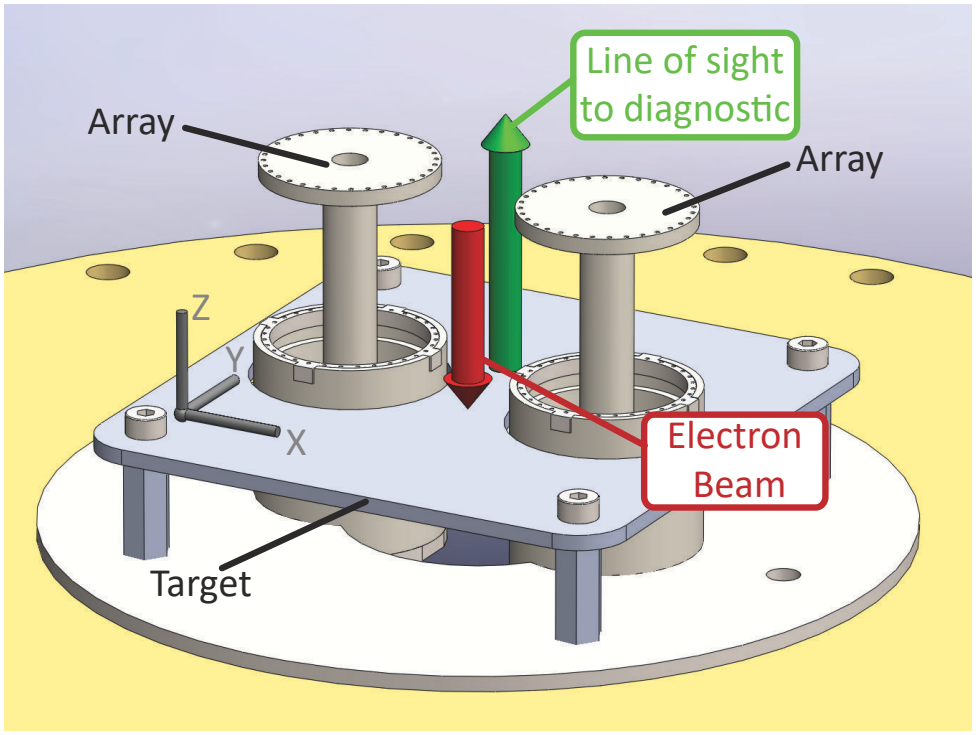

Figure 4.8: A CAD model of the target geometry used for experiments in which end-on X-Ray imaging diagnostics were fielded showing the position of the wire arrays; a flat target; the orientation of the electron beam and the direction of the spectrometer's line of sight. The wires in the inverse arrays are not shown in the

The most successful experiments in this campaign used a composite target which is shown in figure 4.9. This consisted of a 1.5 mm aluminium plate which exposed to the region $y < 0$ mm and a 30 µm thick titanium foil covering the region $Y > 0$ mm. Changing the target material changed its emission spectrum and this was observed as difference in the X-Ray dose measured by the image plate.

Pinhole camera data from an experiment which used a composite (aluminium / titanium) target is shown in figure 4.10. Images with three different filters are shown in the figure. The fourth frame was filtered with 12.5 µm thick aluminium – no signal was obtained for this filter and so the data is not shown. One of the frames which appears in the figure was filtered with 40 µm thick polypropylene film. The other two frames were filtered with 3 µm and 6.5 µm thick aluminium foil.

A very simplistic view of the physics which dictates the signal, $S(u, v)$, seen in a pinhole image is given by

$$S(u,v) = \int\int G\, R(\varepsilon)\mathcal{T}(\varepsilon) \left\{ l_Z P_{\mathrm{rad}}[f_e] + F_T[f_e] \right\} d\varepsilon dt, \tag{4.1}$$

where u and v are coordinates in the image; G is a factor which accounts for the geometry of the imaging system; ε is photon energy; $R(\varepsilon)$ is the response of the image plate; $\mathcal{T}(\varepsilon)$ is transmission through the filter; l_z is the extent of the system in the Z direction; $P_{\mathrm{rad}}[f_e]$

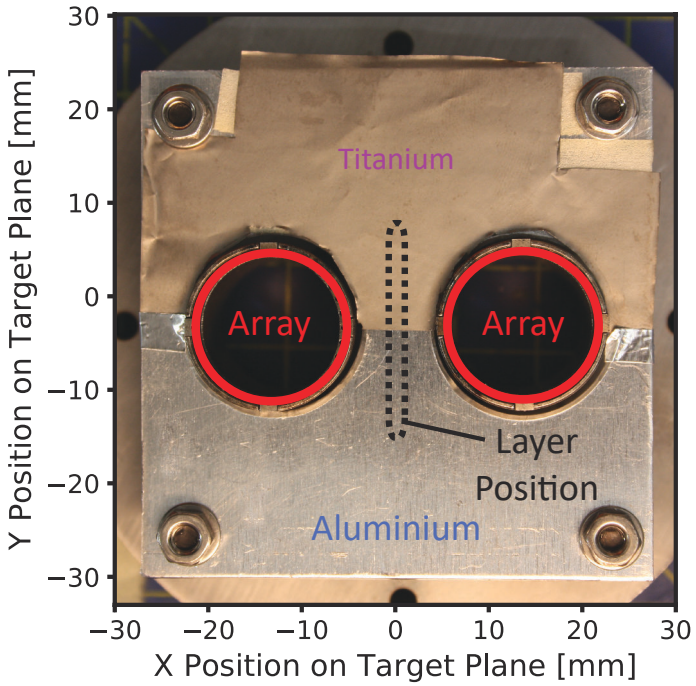

Figure 4.9: A photograph showing a composite target, used for an experiment in which a time integrating pinhole camera was fielded. The image shows that the $Y > 0$ mm region of the target was covered with titanium foil, and the $Y < 0$ mm region was bare aluminium sheet material.

is the radiative power per unit volume emitted by the plasma; $F_T[f_e]$ is the radiative flux from the target; and f_e is the electron velocity distribution function. The functionals P_{rad} and F_T vary in space and time in response to spatial and temporal changes in f_e.

This model clearly misses a fair amount of nuance but serves as a useful conceptual tool to aid in interpreting the data. Electron acceleration would cause f_e to deviate from a Maxwellian. This means that in order to show electron acceleration occurred in experiments it is necessary to identify features in pinhole images which one expects to differ depending on weather or not f_e is a Maxwellian. An important point to note is that one expects some level of emission from the target in response to stimulus from a thermal plasma. This means that demonstrating the signal is dominated by emission from the target is not equivalent to demonstrating the presence of a non thermal electron population in the plasma.

The transmission curves for the filters used to obtain the data in figure 4.10 were calculated using data from [Henke, 1993] and are plotted in figure 4.11. These curves represent $\mathcal{T}(\varepsilon)$ for each of the filters used in the experiment. The plot shows that aluminium has two prominent transmission windows in the 10 eV – 2 keV energy range. The first of these spans the range 15 eV – 75 eV and its falloff can be associated with the aluminium L edge. I will refer to this as the aluminium XUV transmission window. The second window spans the range 500 eV – 1.5 keV and its falloff can be associated with the aluminium K edge. I will refer to this as the aluminium X-Ray transmission window.

Polypropylene also has two transmission windows. The first of these spans the range 250 eV – 300 eV and its falloff can be associated with the carbon K edge. I will refer to this as the polypropylene XUV transmission window. The second window starts at 800 eV and does not falloff. I will refer to this as the polypropylene X-Ray transmission window.

Looking at the plot, the first thing to note is that the X-Ray transmission windows for both materials is around one order of magnitude more transmissive than the XUV window. This is what makes the diagnostic more sensitive to non thermal emission from the target than to thermal emission from the plasma. The second thing to note is that the XUV transmission window in 3 µm aluminium foil is expected to be significantly more transmissive than the polypropylene XUV transmission window.

In figure 4.10, the exposure in the inflow regions is much greater for polypropylene than aluminium. As described in section **??**, electron temperatures measured with Thomson scattering were 15 eV in the inflow regions and 100 eV in the reconnection layer. The fact that the polypropylene image shows more signal in regions associated with colder plasma (where one expects emitted radiation to be colder in spectral character) indicates that in fact, polypropylene is significantly more sensitive to soft radiation than the transmission curves suggest. A possible interpretation is that the signal seen in this image is dominated by low energy photons, below the range considered by Henke *et al* (i.e. below 10 eV).

The use of polypropylene filtered images, in combination with other filters which were designed to preferentially transmit harder X-Rays, generally proved useful. The polypropylene images were not ever used for quantitative analysis of the emission spectrum. Instead they were essentially an alignment aid. They served this purpose because they showed emission from a larger region of the experimental volume – note for example that signatures of the arrays are present as two circular shadows in the polypropylene frame of figure 4.10. This allowed the positions of features in harder X-Ray images to be mapped to positions within the experimental volume because all of the images were captured on the same piece of image plate and the geometry of the pinhole camera was well defined.

Another interesting difference between the aluminium and polypropylene filtered images is that, for aluminium, signal is strongly modulated along the length of the layer. No such modulation is seen for the polypropylene image. The target material changes at the position where the intensity changes in the aluminium filtered image. This implies that the contribution from target emission (i.e. from F_T) is more important for aluminium than for polypropylene .

To quantify this statement, a line-profile of signal on the plate along the length of the layer is plotted in figure 4.12. This shows that the ratio of peak signal from titanium to peak signal from aluminium is given by $I_{Ti}/I_{Al} = 13.5/6.0 = 2.0$. The ratio of atomic numbers for these two elements is $Z_{Ti}/Z_{Al} = 22/13 = 1.7$. As will be discussed later in this section, the intensity for a target-bremsstrahlung spectrum is proportional to the atomic number of the target material. This means the intensity ratio is consistent with target bremsstrahlung emission.

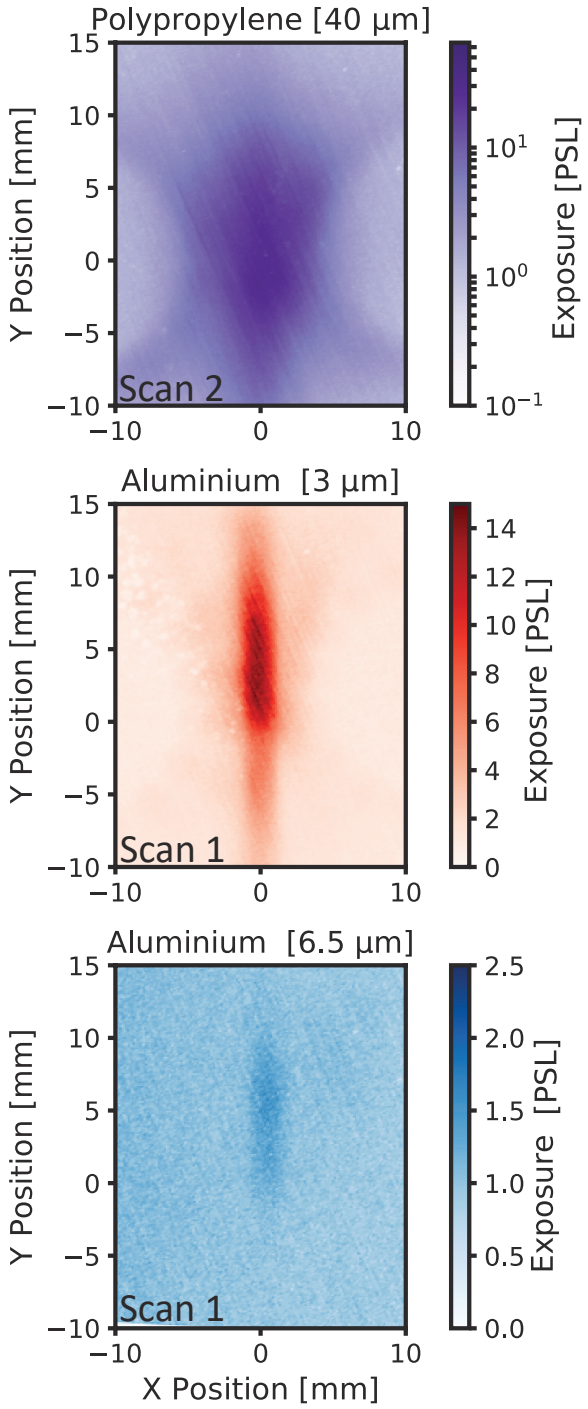

Figure 4.10: Time integrated self emission images with different filters from a reconnection experiment in which the composite target shown in figure 4.9 was used. The image filtered with polypropylene film was saturated on the first scan, and the data shown here is from the second scan of the plate. The data shown for the two aluminium filters is from the first scan of the plate.

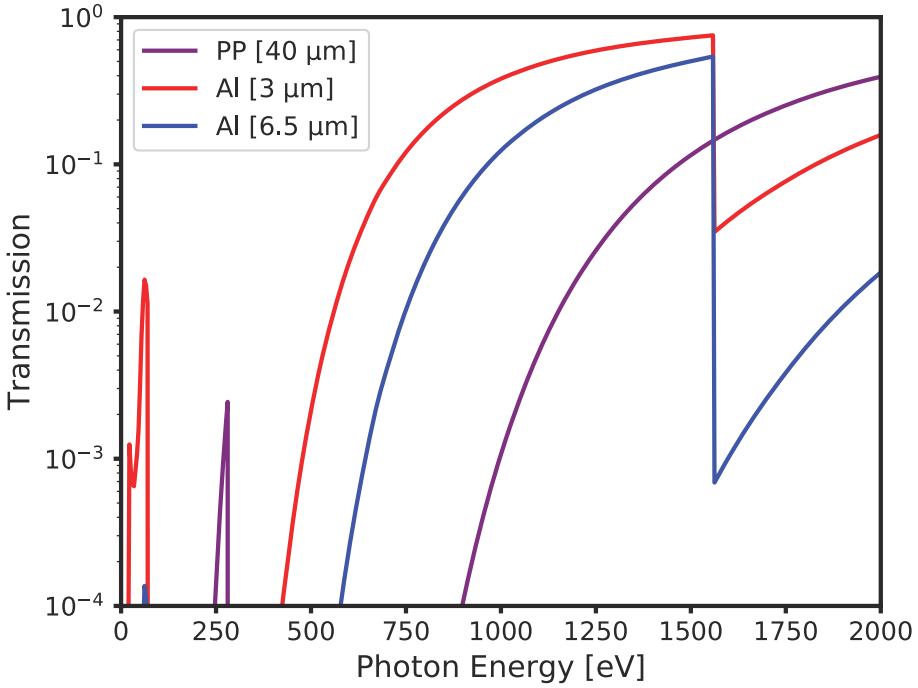

Figure 4.11: Transmission curves for the three filters used in figure 4.10 calculated using data from [Henke, 1993; Gullikson, 1994].

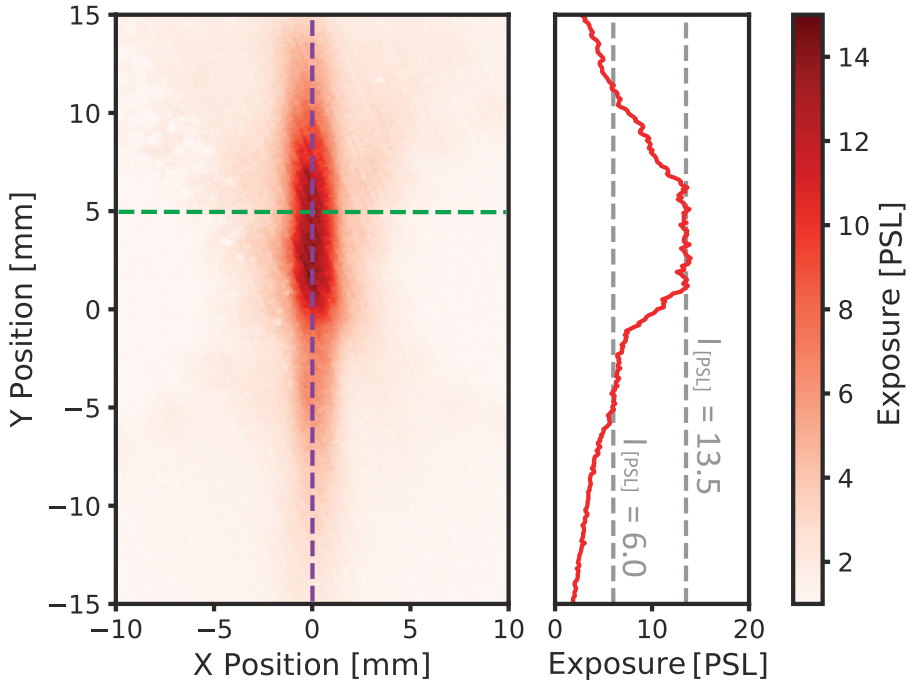

Figure 4.12: The same 3 µm filtered pinhole image which is shown in figure 4.10, along with a profile line showing the average PSL values along the line $X = 0 \pm 0.5$ mm. The transition between emission from the aluminium and titanium regions of the target is clearly visible

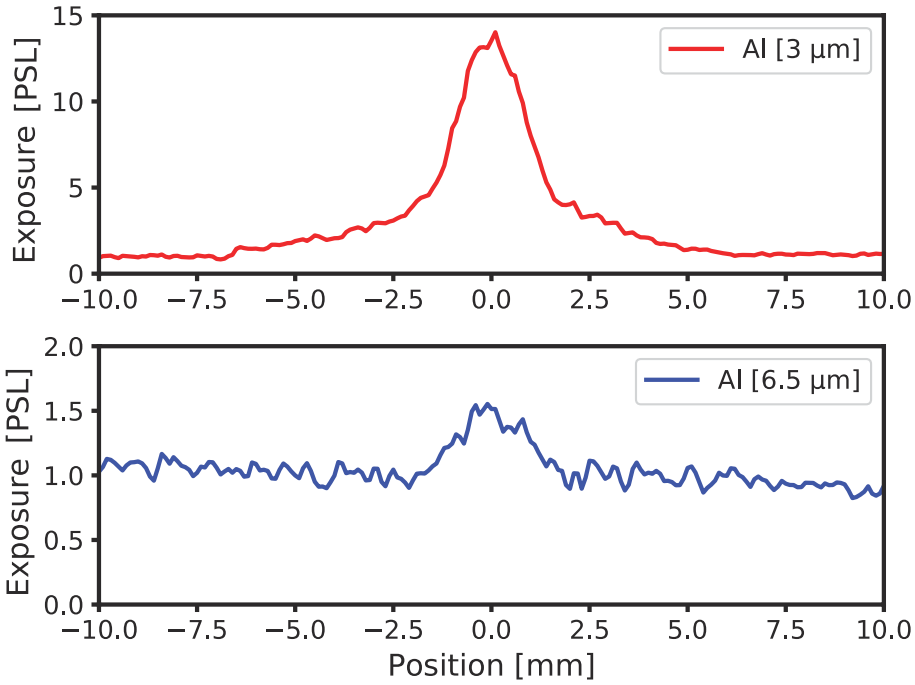

Figure 4.13: Horizontal profile lines, along $Y = 5$mm, taken from the two aluminium images presented in figure 4.10. The data shows that the ratio of maximum signal obtained from the 3 µm to maximum signal obtained from 6.5 µm aluminium filters is ~ 10.

The final piece of analysis it was possible to perform using this data was to consider if the ratio of exposure in the 3 µm to exposure in 6.5 µm aluminium filtered images reveals useful information about the characteristic energy of emission in the experiment. Figure 4.13 shows horizontal profile lines taken along $Y = 5$ mm which is the position of the green dashed line in figure 4.12. The profiles show that the ratio of maximum exposure in the 3 µm to the 6.5 µm images is ~ 10.

The full width half maximum of the image plate profiles is around 1 mm. This consistent with the interferometry data when taking into account the the magnification of the pinhole camera ($M = 0.5$) and the pinhole diameter of 800 µm; implying a resolution of 1.2 mm.

In order to interpret the ratio of emission seen between the two profiles, it was assumed that the signal seen in the pinhole images was completely dominated by emission from the target so equation 4.1 was reduced to

$$S(u, v) = \int \int G\, R(\varepsilon)\mathcal{T}(\varepsilon)\, F_T[f_e]\, d\varepsilon dt. \tag{4.2}$$

The response of the image plate was assumed to take the form

$$R(\varepsilon) = \begin{cases} k\epsilon, & \varepsilon > 8\ eV \\ 0, & \text{otherwise,} \end{cases} \tag{4.3}$$

where k is a constant of proportionality with the dimensions [PSL/eV], and the 8 eV cut-off represents the size of the bandgap in the phosphor. This is clearly a simplification based on the results presented in section **??**, but is reasonable compared to other uncertainties in this analysis, at least for the range 10 eV – 2 keV, where emission is likely to be strongest for this experiment.

The form of $\mathcal{T}(\varepsilon)$ for the two filters were calculated from values in [Henke, 1993], as described above. All this leaves is a consideration of the form of the emission spectrum. The flux of bremsstrahlung spectrum obtained from a single electron incident upon a thick, cold, metal target is approximated by an equation of the form

$$F_T(\varepsilon)d\varepsilon = cZ(\varepsilon_0 - \varepsilon)d\varepsilon, \tag{4.4}$$

where ε_0 is the initial energy of the incident electron; Z is the atomic number of the target; and c is a constant [Dyson, 1990, p. 15].

It follows that the bremsstrahlung emission spectrum one anticipates for an ensemble of electrons is given by the equation

$$F_T(\varepsilon) = cZ \int_{\varepsilon_0=\varepsilon}^{\infty} (\varepsilon_0 - \varepsilon) f_e(\varepsilon_0) d\varepsilon_0, \tag{4.5}$$

where f_e is the electron energy distribution at the position of the target.

The form of I_ε for a Maxwellian and a mono-energetic electron beam were calculated – analytically for the electron beam, and numerically for a range of Maxwellians at discrete temperatures.

This is all the information which is required in order to evaluate the ratio of expected values of $S(u, v)$ for different filters. Considering signal ratios for different filter thicknesses is advantageous compared to considering absolute signal values. This is because in the process of dividing the signals, values of constants which carry high uncertainty (i.e. k, c, G, and the density one should use in f_e) cancel out. In particular the value of k – the constant which appeared in equation 4.3, is problematic because it includes information about the sensitivity of the image plate scanner which was not calibrated.

Figure 4.14 shows that, the observed signal ratio ($S_0/S_1 \sim 10$) requires an electron temperature ~ 100 eV if the emission is stimulated by a thermal electron population; or a characteristic energy ~ 1 keV if the emission is stimulated by an electron beam.

The value of 100 eV one obtains by assuming the electron population is thermal agrees with the layer temperature measured by Thomson scattering. However the target bremsstrahlung model assumed that incident electrons were energetic enough to penetrate deep into the unperturbed bulk of the target. For low energy electrons (less than around 900 eV) results from X-Ray tube experiments show a reduction in the intensity of photons emitted, and a deviation from proportionality of intensity to target atomic number [Dyson, 1990]. The estimate of 100 eV Maxwellian from this model should therefore be considered only as a lower bound on temperature.

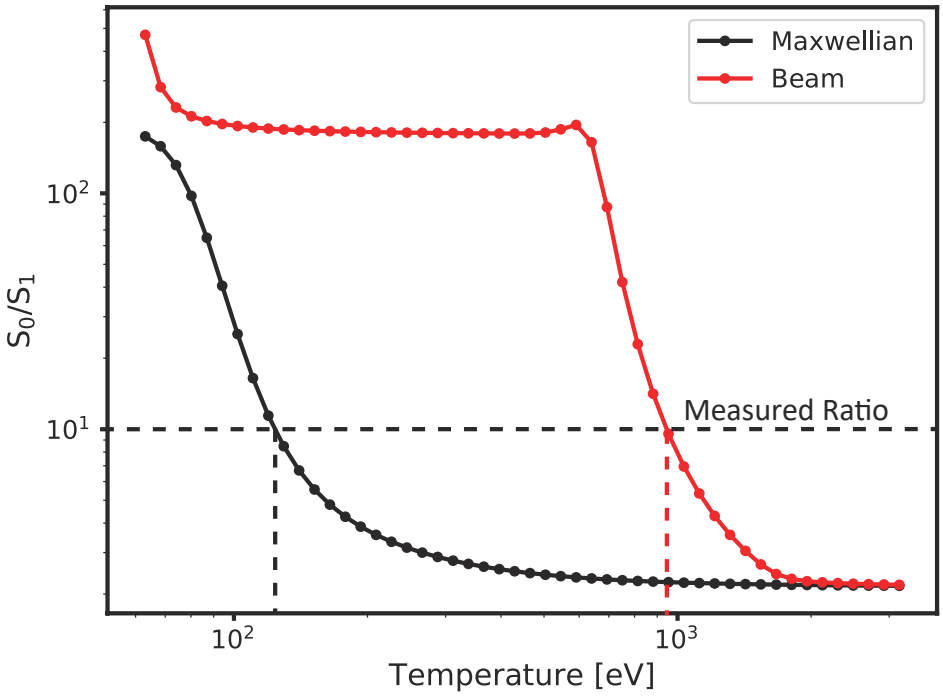

Figure 4.14: Ratio of the signal expected through 3 µm aluminium (S_0), to 6.5 µm aluminium (S_1), plotted for a Maxwellian energy distributions and a mono-energetic electron beams as a function of temperature/characteristic energy.

It also seems very unlikely that emission from the target would dominate over emission from the plasma if the situation really was a thermal plasma in contact with a cold target. I say this because in such a situation one would expect there to be a layer of colder, denser plasma at the boundary between the target and the carbon plasma. Electrons would be slowed in this layer rather than making it to the unperturbed solid target. This means that it would be expected that emission from the target would have a colder spectral character, rather than the harder character suggested by the data.

I would also expect that the radiation produced by by this boundary plasma ought to emit radiation with intensity proportional to $\bar{Z}^2$, where $\bar{Z}$ is the average ionisation state in the plasma [Zeldovich, 1966, p. 258]. From an energetics perspective it seems unlikely that the ionisation state of plasma made from aluminium vs. titanium might have an ionisation state which differs by more than a factor of a few for the same inferred temperature ($\sim 100\,\mathrm{eV}$). Therefore, the presence of a variation in intensity in proportion to target atomic number suggests that emission was from non thermal electrons.

To summarise the discussion contained within this section, time integrated pinhole images do not conclusively prove that non thermal electron acceleration is occurring in reconnection experiments but they do suggest that acceleration may be occurring. The images also show that if acceleration does occur then it happens exclusively inside the reconnection layer, and that if the energetic population is described by a beam, then that beam has a characteristic energy of order 1 keV.

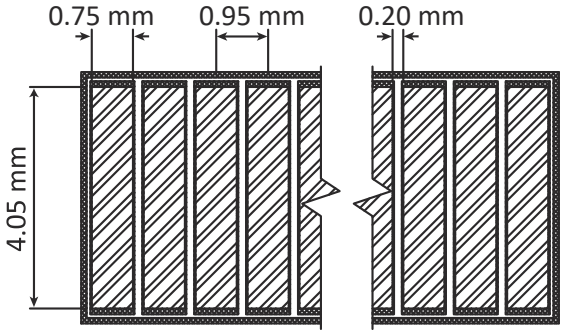

Figure 4.15: A diagram showing the geometry of the diode array. Photoconcucting elements are indicated by diagonal shaded features in the diagram.

4.3 Time Resolved Slit Images of the Reconnection Layer

To improve on measurements which had been made with the time integrating pinhole camera, a series of experiments were conducted in which X-Ray flux was measured using an array of silicon photodiodes. These measurements were useful for two reasons. Firstly, they provided time resolution. This meant it was possible to ensure that X-Ray emission measured in previous experiments was a signature of the reconnection processes rather than some transient effect associated with the early or late time behaviour of the experiment or current feed. Secondly, the photon energy resolved response of the photodiodes was relatively well characterised. This made it possible to make an absolute intensity measurement of the emission from the experiment which was compared against a model for plasma emission.

The series of experiments which were performed with the diode array used the flat spectral target setup which had previously been fielded for time integrated pinhole camera experiments (shown in figure 4.9). The targets used in this series of experiments were all made of aluminium sheet material. The diode array was an Opto Diode AXUV20ELG, which consists of 20 photoconducting elements arranged linearly, as shown in figure 4.15. The figure shows that the size of each element is $0.75 \times 4.05\,\mathrm{mm}^2$ and that the separation between the centre of each element is 0.95 mm.

These diodes use Opto Diode's AXUV technology which is described in section 2.4.2. The array consists of a single anode (which is common to every photoconducting element) and a separate cathode for each individual element. For the work presented here, the common anode was biased to $-9\,\mathrm{V}$, and the current through the 10 central elements was relayed to an oscilloscope using separate coaxial cables. Each cable was terminated using a $50\,\Omega$ resistor positioned at the oscilloscope. The voltage across each terminating resistor was measured and used to infer the X-Ray fluence incident upon each element in the array. The outer 10 elements in the 20 element array were not used in order to reduce the complexity of the experimental setup.

Figure 4.16 is a cross section of the X-Ray imaging system used for these experiments.

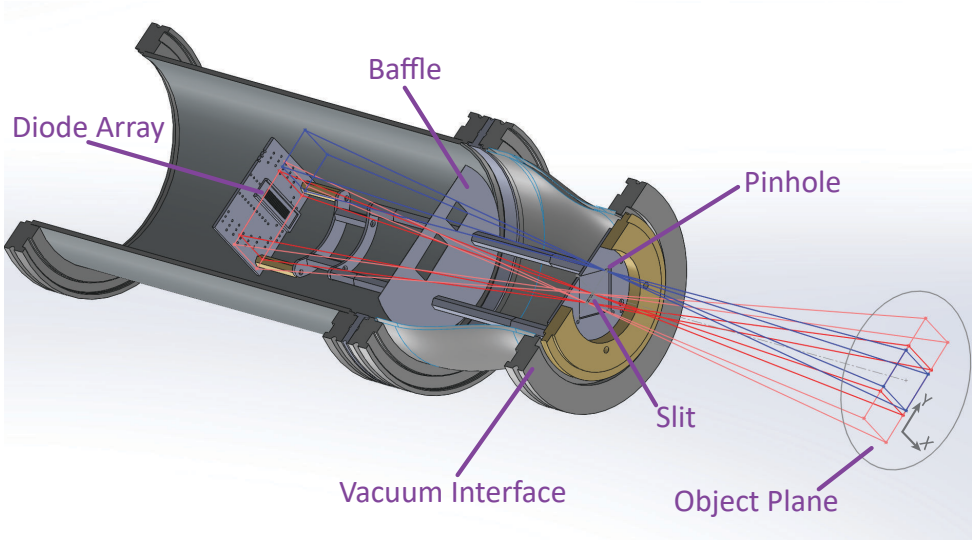

Figure 4.16: A cross section of the diagnostic setup which was use to image the reconnection layer onto a diode array. Ray traces for the pinhole and slit imaging systems are shown in blue and red respectively.

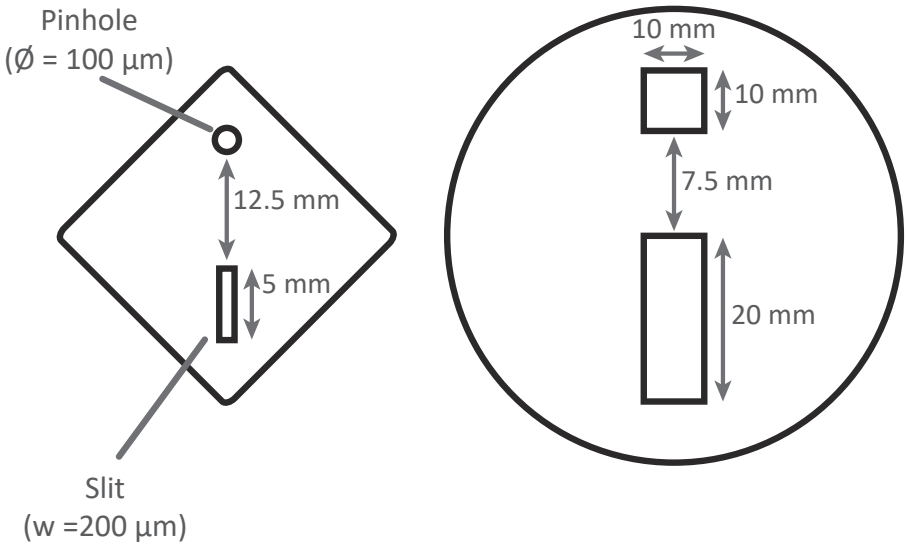

Figure 4.17: *Left:* A diagram (not to scale) of the plate containing the X-Ray apertures used to image the reconnection plane. *Right:* A diagram of the baffle plate, which was used to prevent cross talk between the two imaging systems used in this setup. Both plates were laser cut from 200 µm thick stainless steel.

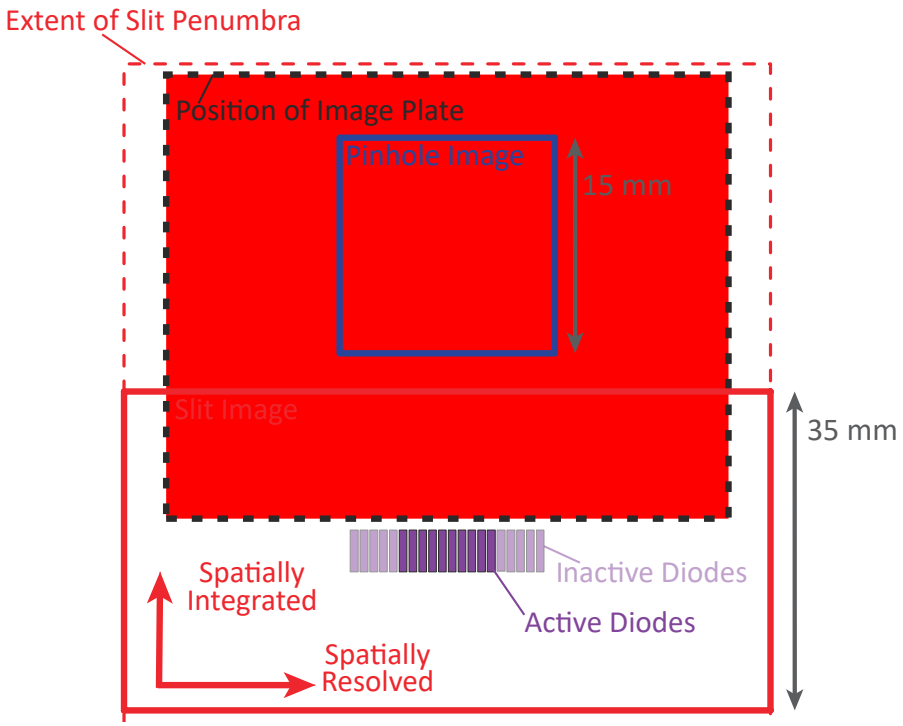

Figure 4.18: A diagram showing images formed by the setup used for experiments with a linear photodiode array on the detector plane. The diagram shows the setup formed two images, a slit image and a pinhole image. The diode array consisted of 20 photoconducting elements, the central 10 of which were used in experiments — with the rest shorted out.

The figure shows the system used two separate apertures to image radiation from the experiment. The first of these was a pinhole which cast light (blue rays) onto a piece of image plate positioned on the same plane as the diode array. The second was a slit imaging system which cast light (red rays)onto both the image plate and the diode array. In the figure, a ray-trace for the pinhole imaging system is shown in blue, and one for the slit imaging system is shown in red. Diagrams showing the geometry of the X-Ray apertures, and the baffling which was employed to prevent cross talk between the two imaging systems are shown in figure 4.17.

Projections of the ray traces onto the image and object planes are shown in figures 4.18 and 4.19 respectively. The image plane diagram also shows the relative positions of the image plate and the diode array. The diode array was oriented so that it was spatially resolving in the same direction as the slit. The system was setup so that, for light cast from the object plane, the X-axis of the pinhole image could be directly related to the spatially resolved axis of the slit image. This enabled features seen in the signal from the diode array to be related to features seen in pinhole images obtained in previous experiments.

In figure 4.16 showing the projection of the ray traces onto the object plane, the positions of the arrays and the reconnection layer are also shown. The slit was oriented to resolve structure across the reconnection layer (in the X-direction of the experiment). The magnification of the system meant that the width of the image of the layer was comparable to the

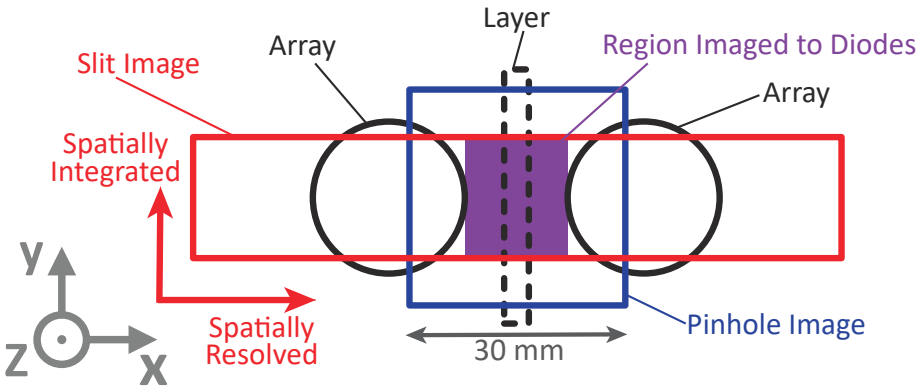

Figure 4.19: A diagram showing the expected position of features imaged by the setup used for experiments with a linear photodiode array in the plane of the target which was placed below the reconnection layer.

width of an element in the array. It is important to note that the positions of the arrays and layer indicated in figure 4.19 are the intended alignment rather than what was achieved in real experiments. The design of this diagnostic meant that the relative positions of the X-Ray detectors, baffling , and imaging apertures were well defined, but the alignment of the whole system with respect to experimental hardware was very difficult to achieve and so the position of features on the object plane were only accurate to $\sim 4\,\text{mm}$. This was a significant limitation of the setup and if I was to re-design the diagnostic I would devote a serious amount of thought to how I might ensure a more reliable alignment. That said, in-spite of this alignment error, the pinhole imaging data provided the means to establish which diode(s) light from the reconnection layer was imaged onto. This meant that data obtained using the diagnostic could be reliably interpreted reliably.

Figure 4.20 shows example image plate data obtained using this experimental setup. The pinhole was filtered with $40\,\mu\text{m}$ polypropylene and the slit was filtered with $6.5\,\mu\text{m}$ aluminium. In general the images are as expected, although the slit image does not cover quite as much area as was predicted – something which can be attributed to a horizontal misalignment of the diagnostic.

A total of eight experiments were conducted using this experimental setup. Signal was only seen on the diodes in two of these (s0427_18 and s0509_18). This was attributed in part to the fact that the diagnostic was difficult to align accurately enough to ensure that emission from the layer was imaged onto the diodes. Even taking this into account, the number of experiments in which signal was obtained is very low – making it impossible to exclude the possibility that some non repeatable aspect of the reconnection process contributed to the observed X-Ray emission. A possible interpretation is that the X-Ray emission depends on some aspect of the experiment which has not been observed in previous experiments. If the emission could be attributed to electron acceleration then it would imply that the number or energy of fast electrons varied from shot to shot.

In an attempt to reliably capture the region of interest, the magnification of the imaging

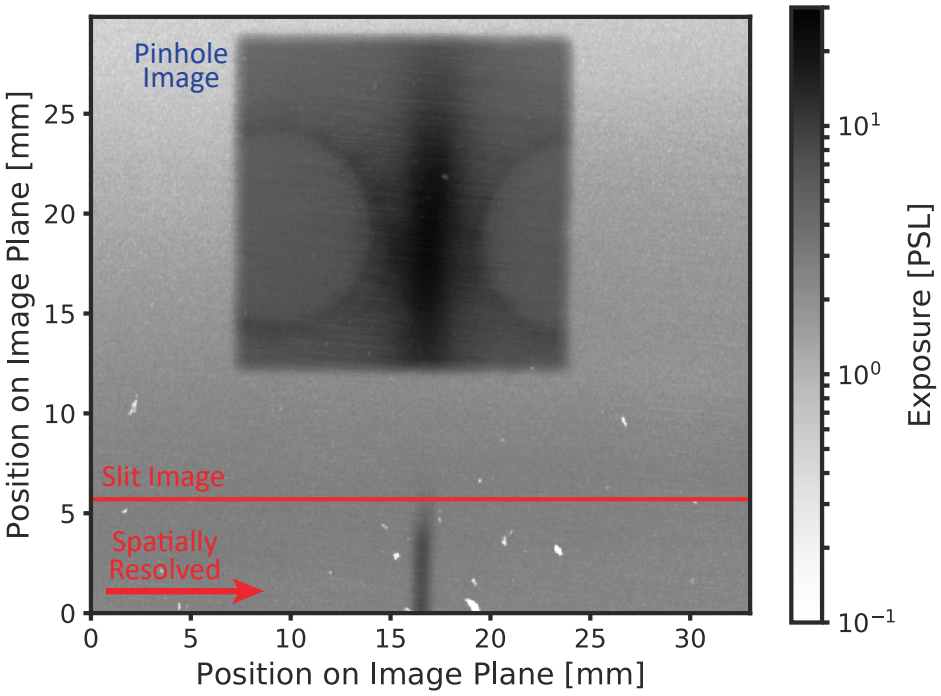

Figure 4.20: Image plate data used from an experiment in which the linear photodiode array was fielded (s0505_19). The extent of the slit image which was predicted through raytracing is shown as a red horizontal line.

system was reduced in order to increase its field of view. The dimensions in figures 4.19 and 4.19 correspond to the configuration used in s0509_19, where the magnification was 0.5, and the slit width was 400 µm, implying a geometric resolution of 1.2 mm. For s0427_19, the same slit was used but the magnification was 1.0 so the geometric resolution was 0.8 mm. The width of an element in the diode array was 0.75 mm.

Figure 4.21 shows the diode signals obtained in s0427_18 and s0509_18. The X-axis of the plot is time (in nanoseconds) after current start; the signal from each diode is mapped to a position on the Y-axis which corresponds to its location in the array; and the colour-map indicates diode signal (in volts). The pinhole image from s0427_18 showed that the layer was imaged onto the diode at 2 mm. This diode shows signal in the interval 250–500 ns after current start. In s0509_18, the layer was imaged to the diodes at 2 and 3 mm which both show signal in the interval 250–350 ns after current start. In s0427_18, other diodes in the array do not show any signal. In s0509_18, all of the diodes in the array show a peak with a width of ~ 40 ns and centred on $t = 100$ ns. Since this feature is not localised to a region in the experiment, it is not possible to speculate about the mechanism which might have caused it.

From interferometry images, the width of the reconnection layer is 1 mm and this is consistent with the fact that signal appears on one diode in s0427_18 (where the image resolution is less than the width of the object), and across two diodes in s0509_18 (where the layer would not be fully resolved due to geometric resolution of the imaging system).

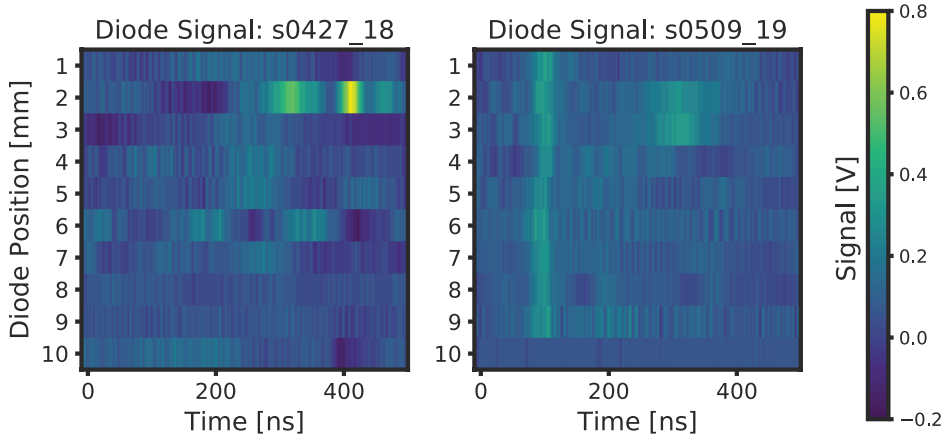

Figure 4.21: A heatmap showing the diode signals obtained in two reconnection experiments (s0427_18 and s0509_18). In this plot, $t = 0$ ns is defined as the time at which current drive through the arrays is first measured on the Rogowski probes.

Figure 4.22 shows the signal from the 2 mm diode in s0427_18 and the *sum* of the signals in the from the diodes at 2 and 3 mm in s0409_18. In addition to diode signals, the plot shows normalised current traces (i.e. I/I_{max}) obtained from the two experiments. The current traces are normalised in this way in order to best compare the shape of the different current profiles. In an absolute sense the current in s0509_18 peaked at 1.4 MA, in s0427_18 it was closer to a peak of 1 MA. The reduction in current in s0427_18 was related to miss timing in the pulsed power current feeds, which would have resulted in systematically lower densities and temperatures in the inflow to the reconnection layer in this experiment.

The signal from the diode in s0427_18 consists of three peaks, the first of which is centred on 320 ns; is ∼50 ns wide; and has a maximum amplitude ∼0.6 V. The second peak is more intense (V_{peak} =0.75 V), and narrower ($\Delta\tau$∼25 ns).

In s0509_18, the signal has two peaks, the first of these was not localised to the layer, as discussed previously. The second is broadly similar to the first peak in s0427_19 in its terms of width, its amplitude and the time when it occurred.

In order deduce if the signal observed on the diodes could be explained by thermal emission from the plasma in the reconnection layer, a number of simulations were performed with the atomic code PrismSPECT. These simulations were used to predict the signal one expects to measure on the diodes in response to thermal emission from plasma in the reconnection layer, taking into account the response and geometry of the diagnostic.

Figure 4.23 shows an example of a simulated spectrum. The simulation was run with an electron temperature of 100 eV and an ion density of 1×10^{17} cm^{-3}, values which were based on quantities measured in previous experiments. The geometry of the simulation was planar, with a length of 16 mm. This length was based on a measurement of the extent of

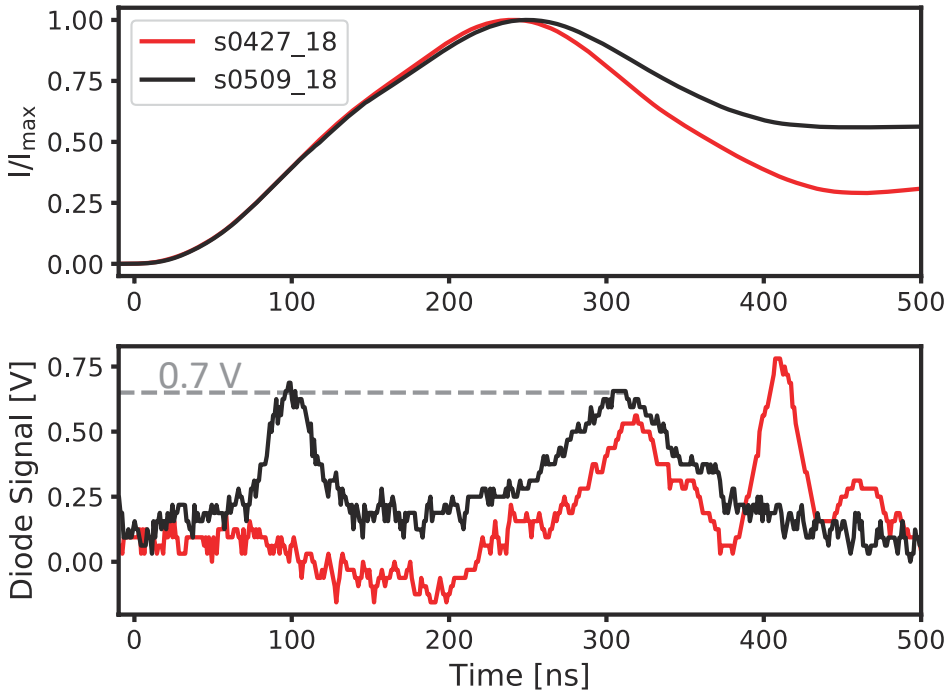

Figure 4.22: *(Top)* A plot showing the normalised current inferred from pair of Rogowski coils positioned on two different return posts and processed using the technique discussed in section **??**. *(Bottom)* A plot showing the diode signal obtained from the diode at 2 mm for s0427_19, and the sum of the signals from the diodes at 2 mm and 3 mm for s0509_19.

the reconnection layer in the Z direction, made from interferometry images. The simulated spectrum can be viewed as a prediction of the radiative emission (per unit area, and per unit solid angle) which is expected from the top surface of the reconnection layer in the experiment – neglecting any contribution from the target.

The simulations were run with a non-LTE atomic level population model, and the default 'emission K-shell spectroscopy' atomic model (provided by Prism) was selected.

Bremsstrahlung is shown separately in the plot in order to highlight that contributions from bound-free and K-Shell line emission actually dominated over Bremsstrahlung at energies $\sim$1 keV[1].

Figure 4.24 shows the photon energy resolved signal [denoted $s(\varepsilon)$] which one expects to obtain on a diode from the spectrum shown in figure 4.23. This was calculated using the equation

$$s(\varepsilon) = R(\varepsilon)\, T(\varepsilon)\, I(\varepsilon)\, \Omega\, A_O, \tag{4.6}$$

where R is the response of the diodes (in W/V); T is the transmission through the foil; I is intensity; Ω is the solid angle subtended by the detector; and A_O is the area of the object's

[1]Originally I assumed (perhaps naively) that Bremsstrahlung would be the only emission process which was relevant at these energies and completely discounted the possibility of any contribution to aluminium filtered image from the plasma based on an analytic calculation of Bremsstrahlung intensity. You live and learn.

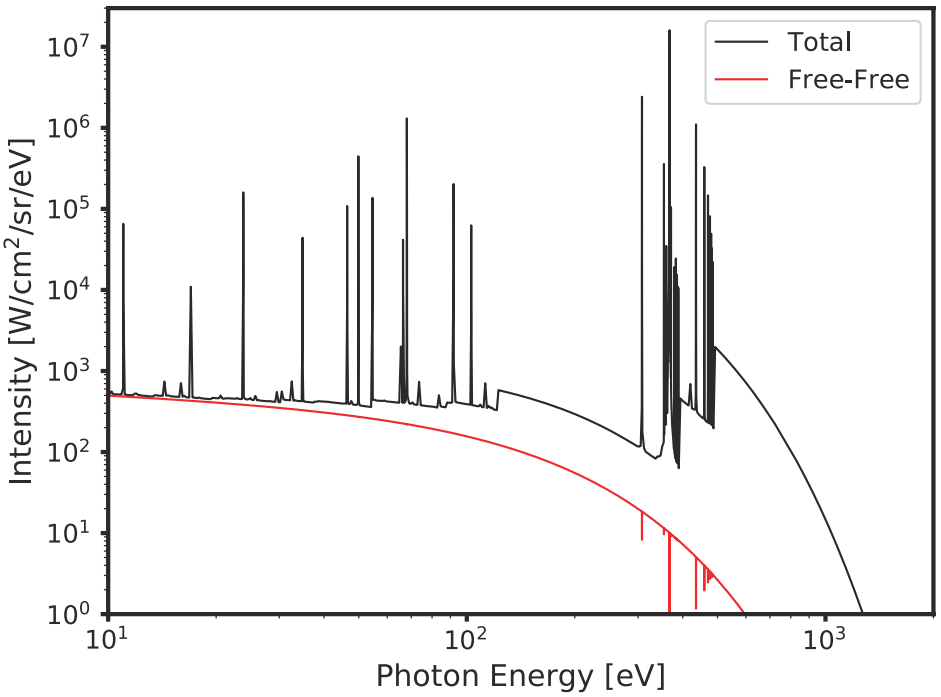

Figure 4.23: A simulated spectrum produced with the atomic code PrismSPECT. The simulation was run in a planar geometry with a length of 16 mm; the electron distribution was Maxwellian with a temperature of 100 eV; the ion density was 1×10^{17} cm^{-3}; and the atomic level population model was non-LTE. In the legend, 'total' refers to the combined contributions from free-free; free-bound; and bound-bound emission processes.

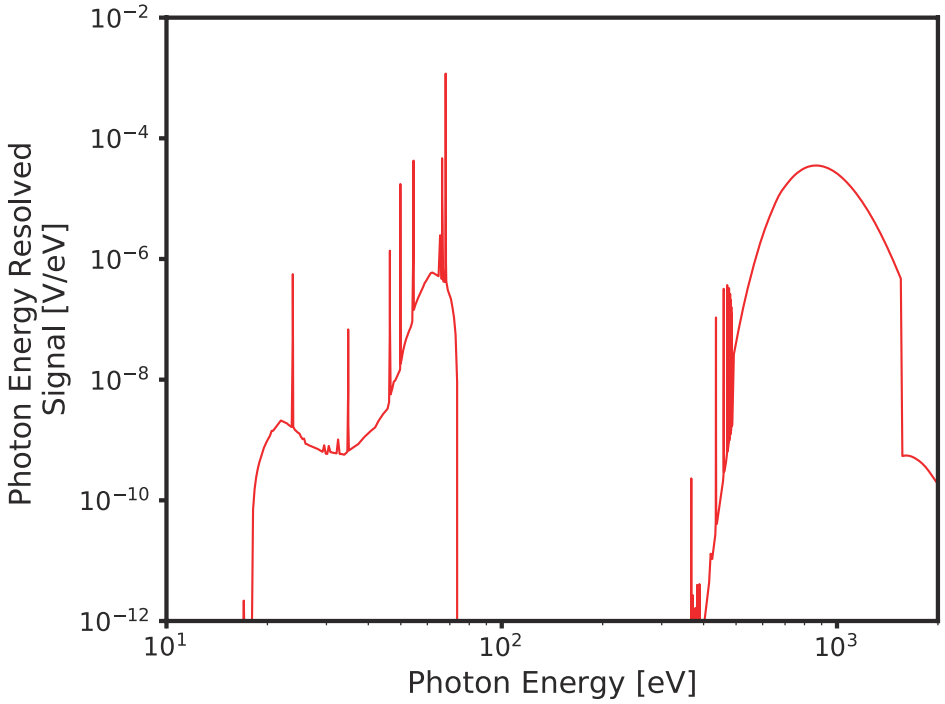

Figure 4.24: A plot showing the photon energy resolved signal (in V/eV) which one expects to obtain on a diode from the simulated spectrum shown in figure 4.23, accounting for setup geometry which was used for these experiments.

emitting surface. To calculate this quantity, the response of the diodes was of the form discussed in section 2.4.2; the transmission was calculated from [Henke, 1993] for 6.5 µm thick aluminium; intensity was taken from the simulated spectrum; and A was taken as 1×1.6 µm^2, which was based on the size of the layer measured in interferometry data.

Figure 4.25 is a schematic illustrating how the solid angle subtended by the detector was calculated . It shows a point source in the top left hand corner. Light from this source is cast through the slit (drawn in red) onto the diode (drawn in purple) ; the width of the slit is denoted w; the height of the diodes is L_D; the separation between the source and the slit is u; between the slit and the detector the separation is v; and the angles within which the combined system collects light are 2θ and 2φ. The diagram shows that the angle subtended by the instrument is limited by the size of the slit in the θ direction and by the height of the diodes in the φ direction. From the diagram, the angles subtended are

$$2\theta = \frac{u}{w}, \tag{4.7}$$

and

$$2\varphi = \frac{L_D}{u+v}. \tag{4.8}$$

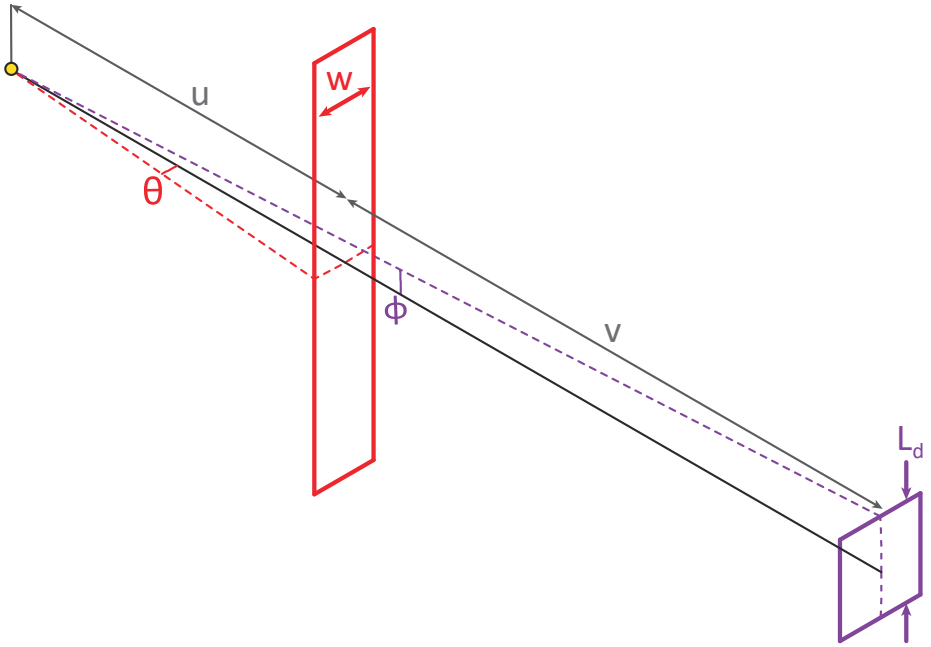

Figure 4.25: A diagram showing the limiting apertures defining the solid angle subtended by the slit imaging system that was used with the diode array. The imaging slit is shown in red and a single element in the diode array is shown in purple. This figure is not to scale.

This implies that the solid angle subtended by the instrument (Ω) was given by

$$\Omega = 2\theta \times 2\varphi = \frac{w}{u} \times \frac{L_d}{u+v}. \tag{4.9}$$

Stating that the angle subtended by the instrument in the θ direction was limited by the slit width is a little bit of a simplification. In reality the image of the layer fell on two diodes for one of the experiments described in this section. In this case, if I had considered the signal from one diode then the measurement would have been limited by the diode's width in θ. For the discussion presented here I have taken the sum of the signal from the two diodes onto which the layer was imaged. For this combined signal, the angle subtended is still limited by the slit. The treatment neglects the fact that there was an 0.2 mm dead region between the two diodes, which lead to the predicted signal being slightly over estimated.

Shot	u [mm]	v [mm]	w [µm]	L_d [mm]	Ω [µsr]
s0427_18	250	250	400	4.1	13
s0509_18	264	145	400	4.1	20

Table 4.1: Estimated values for the solid angle subtended by the instrument in s0427_18 and s0509_18.

Estimated values of Ω for the two experiments considered in this section are are given in table 4.1. In the following discussion I will take the larger of the two values, which is

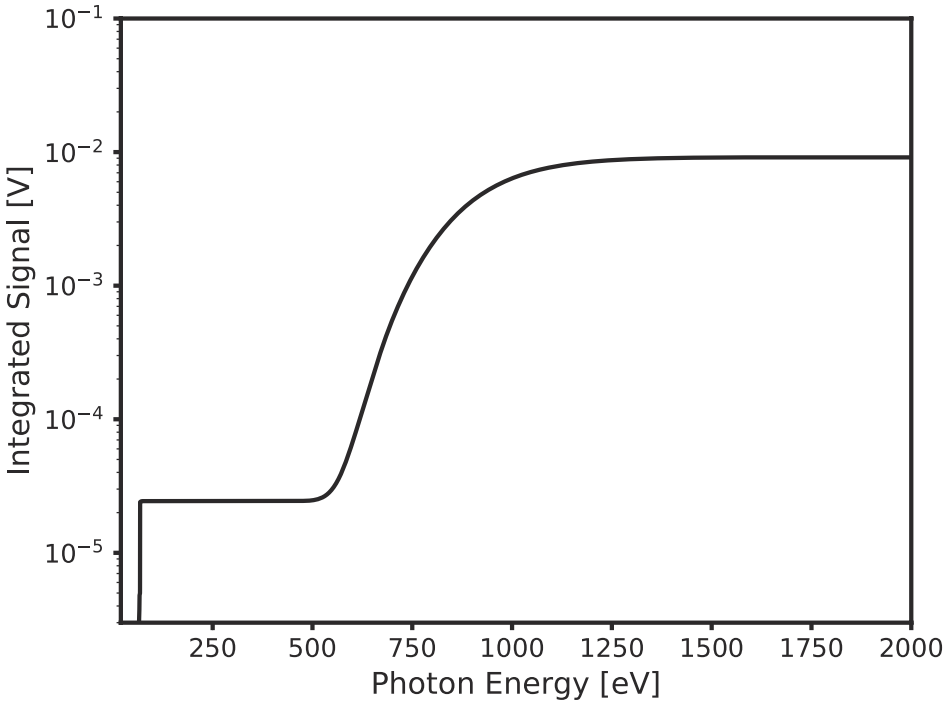

Figure 4.26: A plot showing a running integral of the photon energy resolved signal shown in figure 4.24. This is useful to help understand which spectral features contribute to the integrated signal.

$\Omega = 20\,\mu\text{sr}$.

Figure 4.26 shows a plot of what you might call cumulative signal [denoted $S(\varepsilon)$].This is given by

$$S(\varepsilon) = \int_{\varepsilon'=10\ eV}^{\varepsilon'=\varepsilon} s(\varepsilon')d\varepsilon', \tag{4.10}$$

where ε is plotted on the X axis of the figure. The quantity is sometimes called a running integral. The lower energy bound at 10 eV is the lower limit of the simulation's spectral grid. Energy below this range is not transmitted by the aluminium filter and so does not contribute.

A key thing to note in the plot of integrated signal is that the contribution from photon energies exceeding 1.5 keV is small, and so there is no need to extend the upper energy limit of the simulation beyond 2 keV.

Figure 4.27 is a scatter plot showing the value of $S(\varepsilon = 2\,\text{keV})$ for various electron temperatures and ion densities. It also shows the region of parameter space in which independent measurements place the plasma in the reconnection layer. In previous experiments laser interferometry was used to measure electron density inside the reconnection layer. It was found to be in the range 6×10^{17} – $1 \times 10^{18}\,\text{cm}^{-3}$ at $t = 300\,\text{ns}$. In all of the PrismSPECT simulations used to produce the plot, the average ionisation stage was in the 5.5 – 6 range, indicating an ion density in the range 1×10^{17} – $1.8 \times 10^{17}\,\text{cm}^{-3}$. Thomson scattering measurements put the electron temperature at around 100 eV.

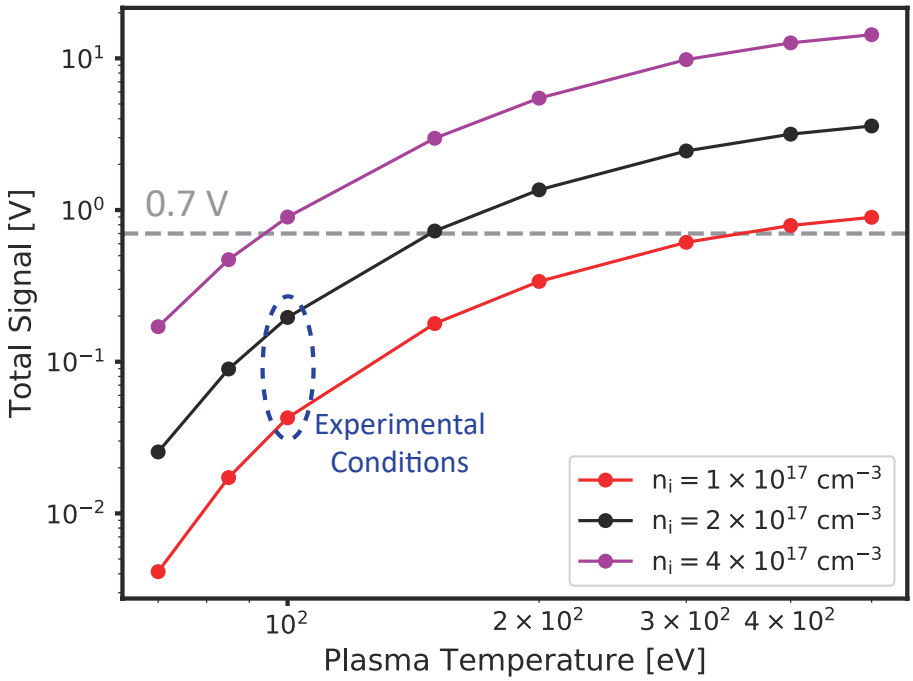

Figure 4.27: A parameter scan showing the total signal one expects for a range PrismSPECT simulations run with different plasma densities and temperatures, compared to the experimentally measured peak signal of 0.7 V.

The scatter plot shows the PrismSPECT model predicts a total signal around one order of magnitude lower than the peak value of 0.7 V measured in the experiment. In this sense the result presented here is very consistent with the time integrated pinhole measurements because it suggests that emission from the spectral target dominates over emission from the reconnected plasma. In terms of what this result means for particle acceleration, it is important to stress that, in the absence of a decent model to understand the emission spectrum simulated by a thermal plasma interacting with a spectral target, saying that emission from the target dominates is not equivalent to a statement that hot electrons are present in the experiment.

The time evolution of the diode signals is very interesting. The peak centred on $t = 300$ ns which was present in both experiments can be reliably interpreted as being a signature of magnetic reconnection as Faraday rotation and interferometry data (obtained from a large number of different shots) show that the layer is well formed for the duration of this emission. The same interpretation cannot at present be applied to the narrower more intense features seen in s0427_18 as there is not sufficient data to demonstrate that the reconnection layer is well defined this late into the experiment. It is therefore possible that the features could be signatures transient behaviour associated with the disruption of the reconnection layer at late time in the experiment.

The full width half maximum of the $t = 300$ ns peak was around 70 ns in both shots. This is interesting because the reconnection layer was observed for an interval of over 200 ns.

The shorter time interval of the emission peak could be interpreted as a signature of plasma dynamics within the reconnection layer, which occur on a relatively short timescale.

A relevant timescale to compare to the width of this peak is the Alfvén time, denoted τ_A. This is given by

$$\tau_A = \frac{L}{v_A}, \tag{4.11}$$

where L is the half-length of the current sheet, and v_A is the inflow Alfvén velocity. From the measurements presented previously in this thesis, the values of v_A and L are well constrained and yield a value of $\tau_A \simeq 100\,\text{ns}$. That's to say, the timescale associated with X-Ray emission is comparable to the Alfvén time.

The predicted timescale associated with the advection of plasmoids from the reconnection layer is also the Alfvén time, and optical self emission images made with a fast framing camera in previous experiments have shown that this prediction is true for pulsed power driven reconnection experiments. A compelling interpretation of the time resolved array measurements was therefore that the measured X-Ray emission was associated with the observation of plasmoids within the reconnection layer. As discussed previously in the thesis, there is some evidence in the computational literature that plasmoid dynamics are associated with particle acceleration [Totorica, 2017; Dahlin, 2015] and so this was an obvious line of enquiry to follow.

4.4 Time Gated Self Emission Images of the Reconnection Layer

In an attempt to understand the time variability of signals seen with the diode array I performed an experimental campaign in which time gated images of emission from the layer were captured using an MCP detector. Experiments were performed using an MCP with four independently triggered plates and the concept was that these would be used to capture images of the layer at two different times – with pairs of plates triggered at the same time. The two simultaneous images were designed to be sensitive to different regions of the emission spectrum. One of was unfiltered and was so was most sensitive to softer radiation (between about 10 eV and 100 eV). The other image was filtered with aluminium and so was most sensitive to harder emission in the aluminium X-Ray transmission window (in the region 500 eV to 1.5 keV). The softer emission image was intended to show what the dynamics of plasma in the layer was doing, and the harder image was to indicate of where a hotter electron population existed within the layer. By comparing the structures in the two images it was hoped that it would be possible to infer if particular features in the layer were associated with hot electrons. The spectral target used in this experimental campaign was oriented parallel to the reconnection plane, as shown in figure 4.9, and was made from 0.5 mm thick sheet tungsten.

In reality, the extremely limited dynamic range of the MCP detectors made imaging the

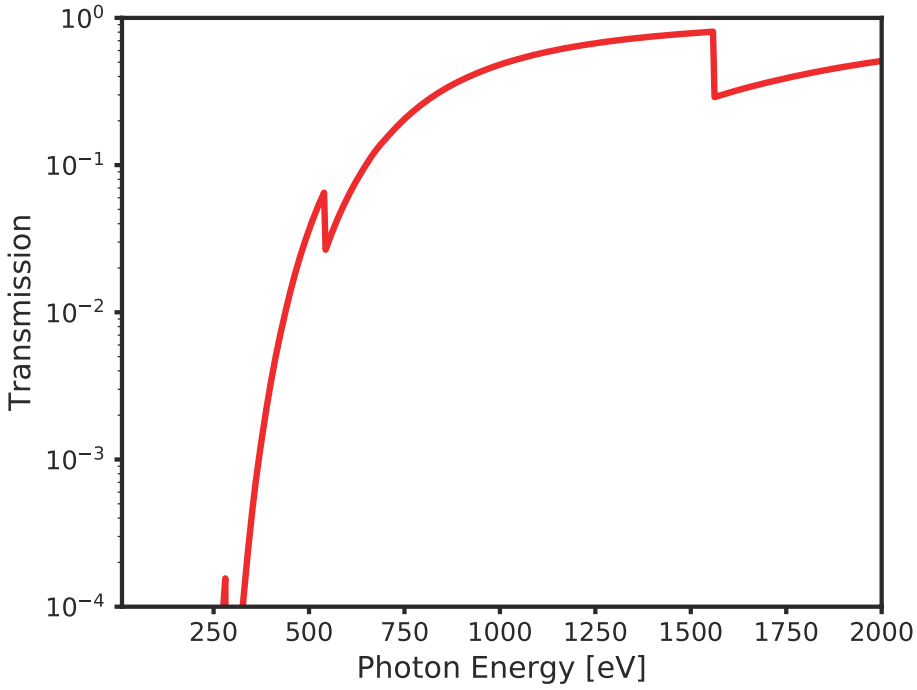

Figure 4.28: An X-Ray transmission curve for a filter consisting of 1 µm thick aluminium foil overlapped with 1 µm mylar film, calculated from [Henke, 1993]. This was the filter which was used to capture the image shown in figure 4.30.

emission through the aluminium filter exceedingly challenging because the overall signal strength was relatively small. In an attempt to combat this difficulty the filter used was adjusted, and eventually a filter pack consisting of 1 µm thick aluminium foil, overlaid with 1 µm thick mylar film was used. Mylar, a polymer with the chemical formula $C_{10}H_8O_4$, was used because it is possible to obtain in the form of exceedingly thin films which are resistant to tearing. The transmission curve for this filter is shown in figure 4.28. This filter allowed little transmission below about 400 eV, with things really picking up above 750 eV. The mylar served the purpose of eliminating transmission through the aluminium XUV window with minimal effect on the X-Ray window transmission. This filter represents maximal transmission in the harder region which it was possible to achieve using established techniques.

Experiments were also conducted with film placed directly against the MCP plates' phosphorous layer. As the phosphor emits photons over 2π, this improved the coupling efficiency of the diagnostic when compared to using a CCD and lens to capture emission. In addition to this, the pinhole used for filtered images had a diameter of 400 µm; compared to 100 µm for the filtered images. Even with all these mitigating strategies things were still severely limited.

Figures 4.29, and 4.30 show an unfiltered image and a filtered one taken during the same experiment. The images were taken 30 ns apart but they the best quality data from the campaign in terms of signal to noise. The magnification of the imaging system was 0.5.

This makes the geometric resolution 0.3 mm for the unfiltered image, and 1.3 mm for the filtered image.

Looking at the unfiltered image, it is clear that emission from the layer dominates which is unsurprising. Structure in the background emission was caused by cross-talk between the different frames in the imaging system rather than actually reflecting a emission which varied across the reconnection plane. The level of background emission was estimated from the region adjacent to the layer. A linear fit to this background profile is shown as a dotted line in the profile of emission from the layer in the figure.

The image shows a internal structure along the length of the layer, which is consistent with that observed with laser interferometry. Particularly striking is the presence of a strong peak in emission centred on $y = 0$ mm, with an extent of around 3 mm in the Y direction. This is consistent with the size of plasmoids observed in interferometry images and so can therefore be interpreted as the signature of a plasmoid in XUV self emission.

In the filtered image, emission from the layer is clearly structured, but the poor noise ratio, and reduced geometric resolution of the imaging system makes it more difficult to associate this structure with layer dynamics than for the unfiltered image. The background in this image does not seem to vary across the reconnection plane – but the estimated background level is again shown as a dotted line in the figure.

Figure 4.31 shows the profile of structure along the layer for the two images plotted side by side. In these plots, the background level has been subtracted and the data has been normalised against peak values. When comparing the two profiles side by side, one possible interpretation is that the structure in the aluminium filtered image is broadly speaking consistent with a bulk motion of the structure seen in the unfiltered image by ~ 3 mm in the negative Y direction. The minima which was present at 0 mm in the filtered image is the place where this is most obvious. The narrow peak at $y = 0$ mm in the unfiltered image appears to be wider, and is less intense relative to the surrounding signal in the filtered image. Part of this peak smoothing can be attributed to the reduced spatial resolution in the unfilterted image. The rest might be attributed to a reduction in the dynamic range for the filtered image.

Saying anything more quantitate about the data presented here is not possible – the diagnostic simply lacks the ability to resolve structure on spatial scales relevant to the reconnection layer. If there had been a difference in emission observed from the same region of the layer in filtered images compared to unfiltered then this may have provided qualitative information about non-thermal electrons. Even this was not possible with data of the quality which was obtained.

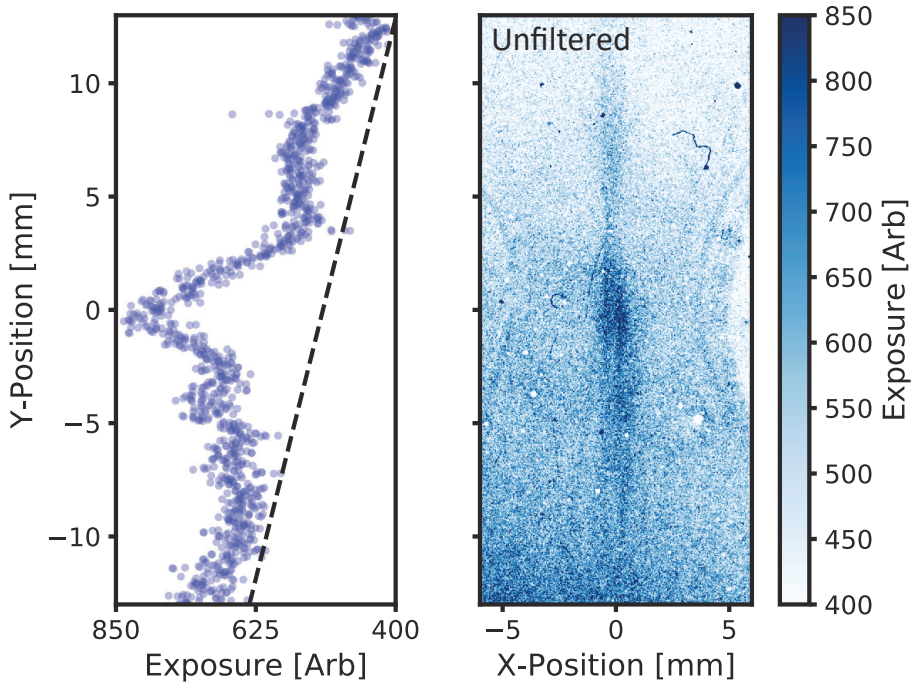

Figure 4.29: *Right:* A time gated, unfiltered image of the reconnection layer, captured with an MCP. The imaging system used a 100 µm pinhole and the image was captured 330 ns after current start. *Left:* A profile line showing structure along the Y-axis and along the centre of the layer. This profile was calculated by taking the average of exposure over $-0.75 < x < 0.75$ mm.

4.5 Side-On Interferometry of the Reconnection Layer in the presence of a tungsten target

Figure 4.32 shows side on processed interferometry data taken during the same experiment as the time gated X-Ray images presented in the previous section. The interferogram was captured $t = 300$ ns after current start. The line integrated electron density profile is very consistent with previous measurements that were made in the absence of a spectral target. I took this result as a good indication that the presence of a target did not act to significantly perturb the properties of the plasma in the reconnection layer – something which is assumed to be true for all of the work discussed in this chapter.

4.6 Measurement of soft X-Ray emission from the plasma in the reconnection layer

In the following section I present the results from an experiment in which a pair of time integrating pinhole cameras were used to diagnose emission from the reconnection layer. One was fielded along the side-on line of sight, in order to resolve structure in the X-Z plane of the experiment. The other was fielded end-on in order to resolve structure in the X-Y plane of the experiment. The two pinhole cameras were nominally identical. They

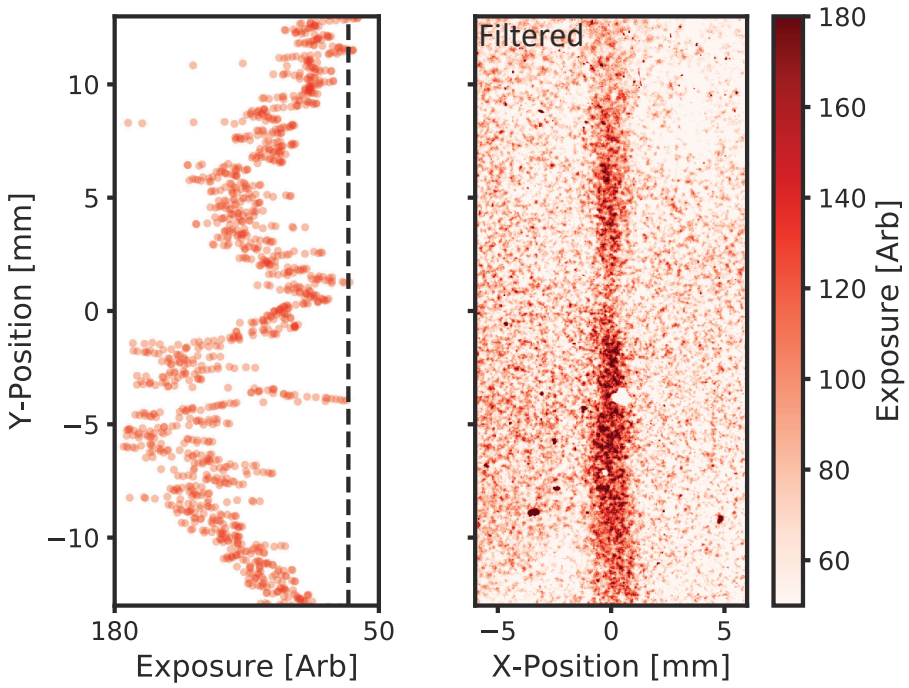

Figure 4.30: *Right:* A time gated, filtered image of the reconnection layer in, captured with an MCP. The filter was made of 1 µm aluminium foil and 1 µm mylar film. The imaging system used a 400 µm pinhole and the image was captured 360 ns after current start. *Left:* A profile line showing structure along the Y-axis and along the centre of the layer. This profile was calculated by taking the average of exposure over $-0.75 < x < 0.75$ mm.

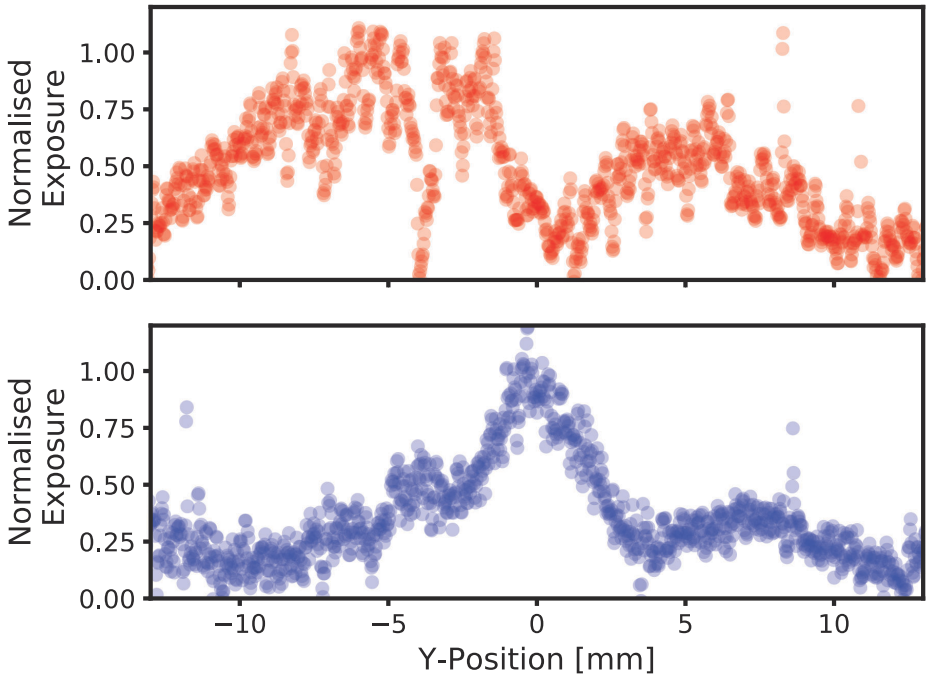

Figure 4.31: A plot comparing structure along the layer from the two MCP images shown above. The background level (indicated by dotted lines in figures 4.30 and 4.29) has been subtracted. Both images are normalised against their peak exposure after background subtraction. The unfiltered (blue) image was captured 330 ns after current start, and the red (filtered) image was captured 30 ns later.

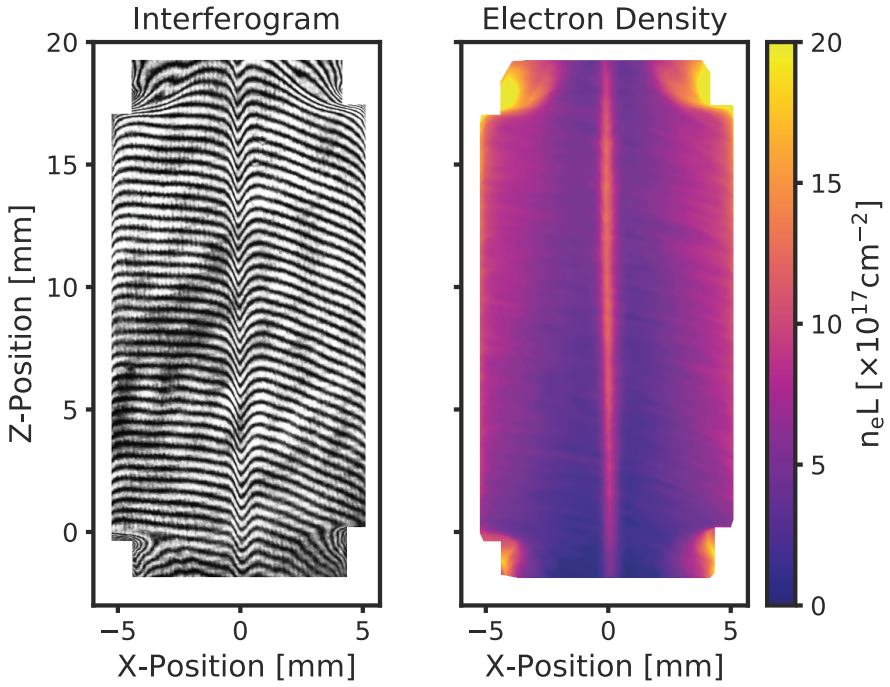

Figure 4.32: A side on interferogram and processed electron density map from an experiment performed with a tungsten target placed 8 mm below the bottom of the arrays. The data shows that this density profile is unperturbed by the presence of the target.

used the same filters; the pinholes were positioned at the same distance from the centre of the experimental hardware; and they had the same magnification. The experiment was performed with a target made of tungsten positioned 8 mm below the reconnection layer and parallel to the X-Y plane of the experiment, which is the geometry shown in figure 4.9.

Figure 4.33, shows the images which were obtained along the end on line of sight. Qualitatively this data is similar to the results shown in figure 4.9 however in these images there is enhanced emission in a region of the reconnection layer localised to $y = -1$ mm, with a width of around 3 mm which was not seen in the previous experiment. Some similarity is expected because pinhole cameras used in both were the same, as was the load setup. A more detailed comparison of data from the two experiments will be given in my subsequent discussion.

Figure 4.34 shows images obtained from the camera which was looking along the side on line of sight. It shows emission from the plasma in the reconnection layer in all three aluminium filtered images. Emission from this image is predominantly from the reconnection layer – in the region $Z = 5 - 10$ mm. The 3 µm image also shows some emission from the region of the target (which was positioned at $z = -8$ mm). Emission is absent from this region in the images filtered with thicker aluminium.

The fact that the region of emission near the target is only seen through the thinnest aluminium filter suggests that this emission is dominated by transmitted through the aluminium XUV window, so is colder in spectral character than the emission from the recon-

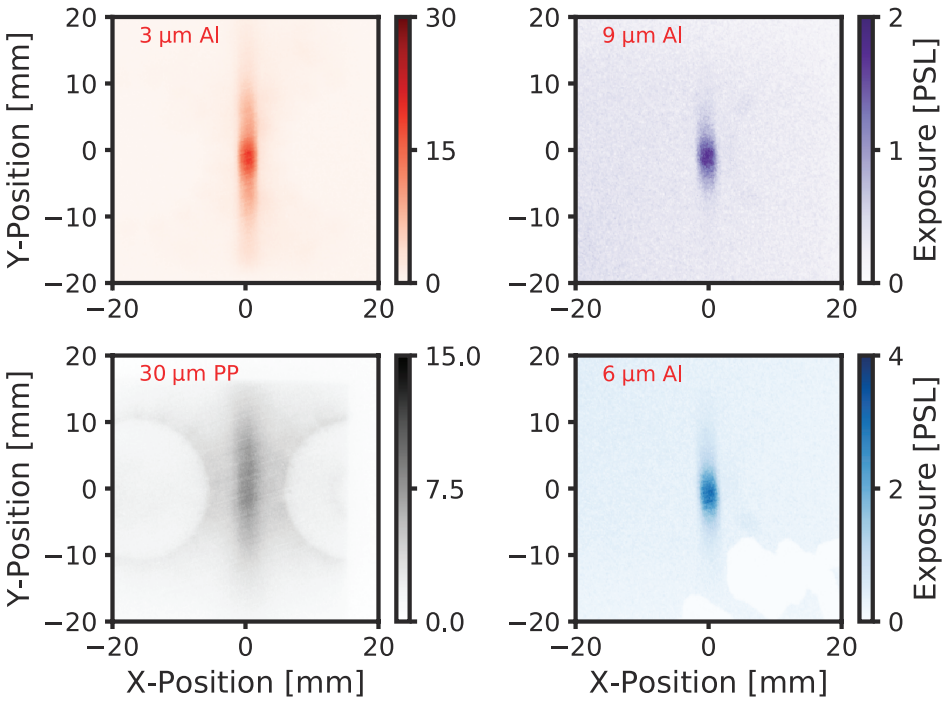

Figure 4.33: Four time integrated self emission images of the reconnection layer. Three are filtered with aluminium (Al) foil in thicknesses of 3 µm, 6 µm, and 9 µm. One is filtered with 40 µm polypropylene (PP) film. The images which were filtered with aluminium used an 800 µm pinhole, and the image filtered with polypropylene used a, 100 µm pinhole. The pinhole camera was fielded along the 'end on' line of sight – which means the images resolve structure in the X-Y plane of the experiment.

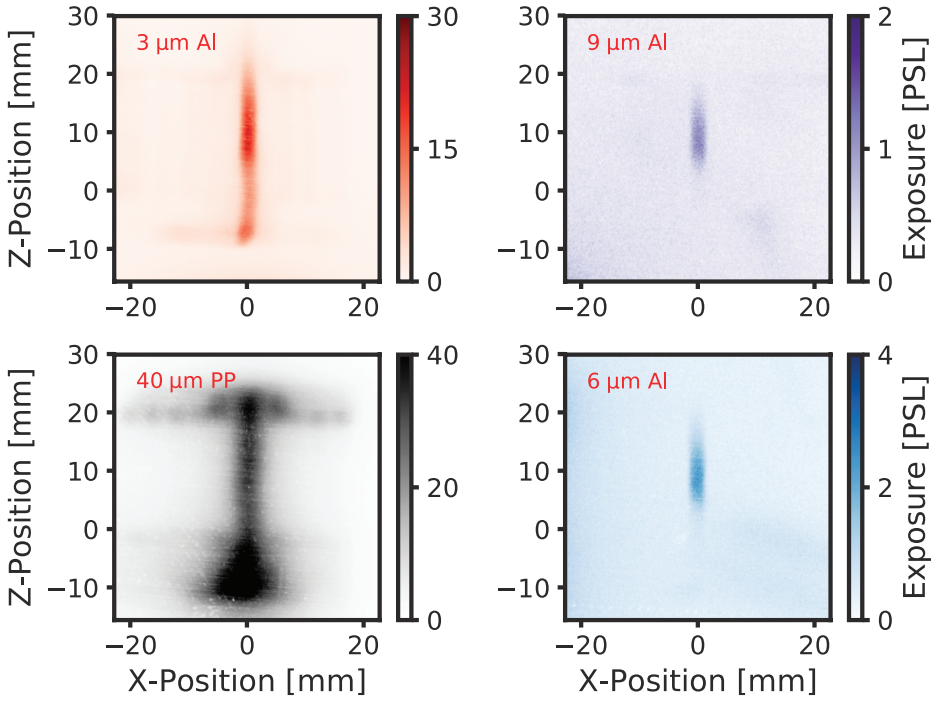

Figure 4.34: Four time integrated images, obtained in the same shot and using the same imaging geometry as those shown in figure 4.33. The filtering and pinholes were identical except for the fact that the polypropylene filter was 40 µm thick and all of the pinholes diameters were 800 µm. These images were taken using the 'side on' line of sight – which means they resolve structure in the X-Z plane of the experiment

nected plasma. This is obviously in contention with the interpretation of results which were presented earlier in this chapter – which suggested that signal in X-Ray self emission images was dominated by emission from the target and that the spectral character of the emission was hotter than the electron temperature in the reconnected plasma.

Figures 4.35 and 4.36 show profile lines along the length of the layer for the three aluminium images from both of the two pinhole cameras. These profiles run along the line $x = 0\,\text{mm}$ and are averaged over a width of 1.3 mm. In a qualitative sense, the magnitude of signal obtained through the three filters is similar. To make this statement more concrete one can compare the values of the quantities

$$S_{\text{end on}}(d) = \int_{y_1}^{y_2} \frac{s_{\text{end on}}(y,d)}{l_{px} \times M} dy, \tag{4.12}$$

$$S_{\text{side on}}(d) = \int_{z_1}^{z_2} \frac{s_{\text{side on}}(z,d)}{l_{px} \times M} dz, \tag{4.13}$$

where d is the thickness of aluminium used for a filter; y and z are coordinates on the object planes; $s(y,d)$ [or $s(z,d)$] is a given end on [or side on] profile line; M is the magnification of the imaging systems; and l_{px} is the physical size of a pixel. For the setup used in this experiment, $M = 0.5$ and $l_{px} = 0.05\,\text{mm}$. If it is assumed that the bounds of these integrals

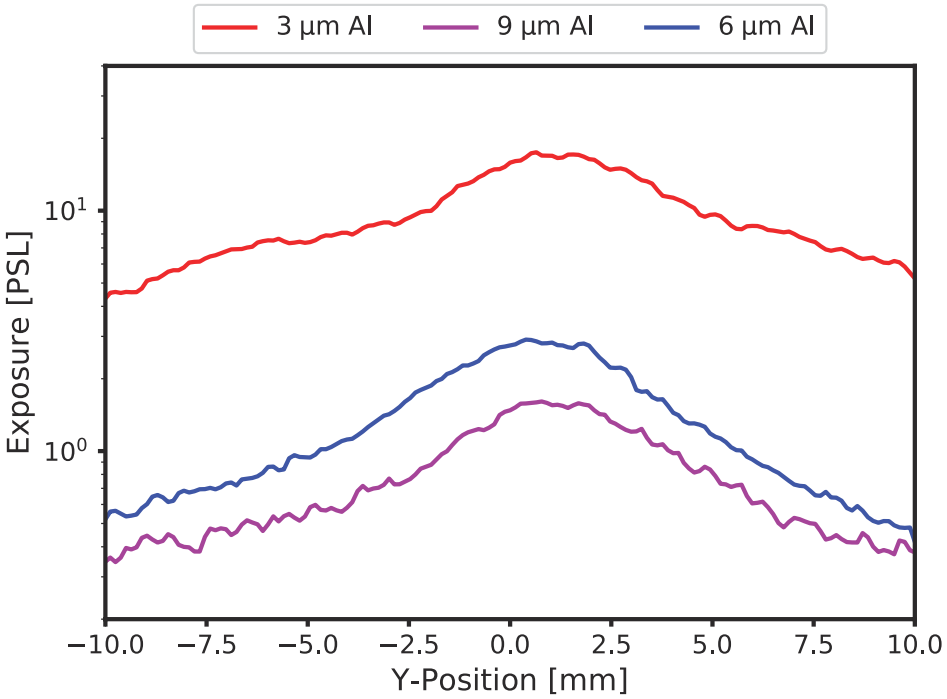

Figure 4.35: Profile lines showing variation along the reconnection layer from the three aluminium filtered end on images shown in figure 4.33. The profiles run along $x = 0$ mm, and are averaged across 1.3 mm in the X-direction.

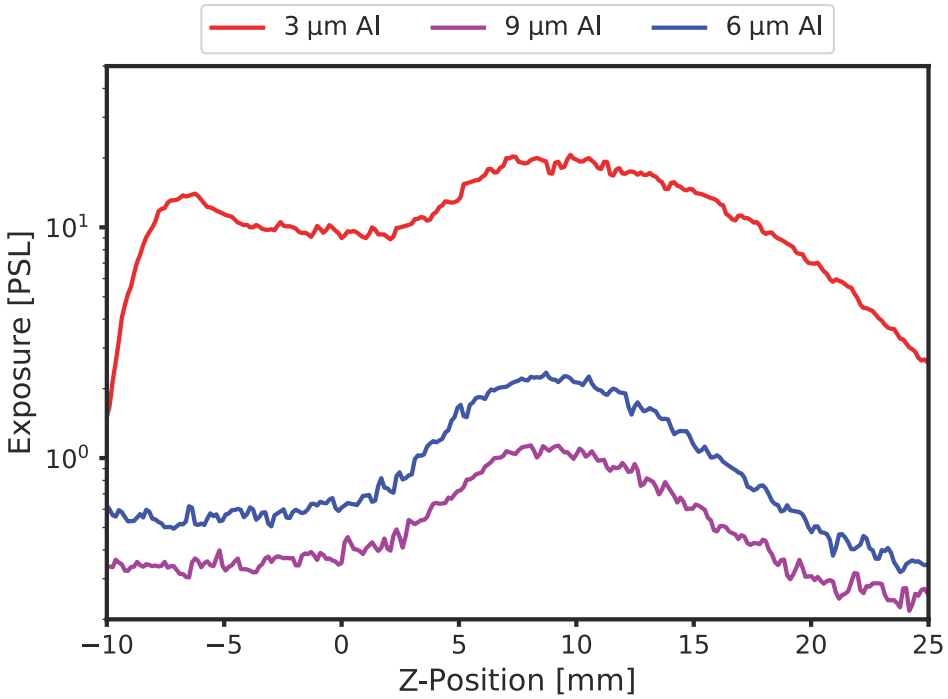

Figure 4.36: Profile lines showing variation along the reconnection layer from the three aluminium filtered side on images shown in figure 4.34. The profiles are averaged in the same way as those shown in the previous figure.

enclose all of the emission in the experiment then it is follows that, if $S_{\text{end on}}(d) = S_{\text{side on}}(d)$, then all of the emission seen in both sets of images is from plasma in the layer and not the target.

Line of Sight	d [µm]	S [PSL]
end on	3	9,760
side on	3	16,100
end on	6	1,310
side on	6	1,400
end on	9	877
side on	9	752

Figure 4.37: Values of total exposure, integrated along the layer, obtained from the images shown in figures 4.33 and 4.34.

Table 4.37 shows values of $S(d)$ for $y_1 = -20\,\text{mm}$; $y_2 = +20\,\text{mm}$; $z_1 = -10\,\text{mm}$; and $z_2 = 25\,\text{mm}$. The integrated exposures agree to within 20% for 6 µm and 9 µm but the values for $d = 3\,\mu\text{m}$ are not consistent with one another. A possible interpretation of this result is that the length of the object in the Y direction is significantly larger than the field of view of which is imaged by the end on pinhole camera and that the temperature of the layer decreases in the Y direction as distance from the centre of the experiment increases. This would increase the exposure seen in the side on images most prominently for the 3 µm filter, as this is comparatively more transmissive to XUV emission and the colder plasma at the edges of would radiate more in the XUV than the X-Ray range of the spectrum.

This interpretation is speculative, but I think the take home message from the data presented in this section is fairly clear: At least for 6 µm and 9 µm aluminium filters, the signal seen in the end on images is dominated by emission from reconnected plasma in the layer, at least for this particular shot.

If one assumes that radiation from the reconnected plasma dominates, then the data can be used to obtain an estimate of the electron temperature in the layer. To do this, I considered the form of equation 4.2, neglecting emission from the target;

$$S(u,v) = \int\int GR(\varepsilon)\mathcal{T}(\varepsilon,d)l_Z P_{\text{rad}}[f_e]d\varepsilon dt. \tag{4.14}$$

The response of the image plate $[R(\varepsilon)]$ was assumed to be given by equation 4.3; and the transmission curves for the filters $[\mathcal{T}(\varepsilon)]$ were calculated using [Henke, 1993]. I assumed that power radiated by the plasma $[P_{\text{rad}}(\varepsilon)]$ took the form

$$P_{\text{rad}}(\varepsilon) = P_0(T_e) \times \mathrm{e}^{-\varepsilon/T_e}. \tag{4.15}$$

Note that this is not equivalent to assuming plasma emission is dominated by Bremsstrahlung radiation, as the spectral character of a single recombination feature is also given by the equation. Therefore, the assumption which was made is that the signal on the pinhole

Line of Sight	d [µm]	Spatial Extent [mm]	μ_E [PSL]	σ_E [PSL]
Side on	3	$Z = 8.75 - 11.25$	19	1
Side on	6	$Z = 8.75 - 11.25$	2.1	0.1
Side on	9	$Z = 8.75 - 11.25$	1.0	0.1
End on	3	$Y = 0.0 - 2.5$	17	1
End on	6	$Y = 0.0 - 2.5$	2.7	0.2
End on	9	$Y = 0.0 - 2.5$	1.5	0.1

Figure 4.38: A table showing the average exposure (μ_E) and the associated standard deviation (σ_E), within the specified spatial extent, from the profile lines shown in figures 4.35 and 4.36.

camera is either dominated by Bremsstrahlung or a single recombination feature. If one takes the electron temperature measured with Thomson scattering as a prior, then figures 4.23 and 4.24 suggest that the signal in this experiment was dominated by recombination from C-VI to C-V, which I use as a justification for assuming this spectral model.

Putting all of this together suggests that the signal from a given pixel take the form

$$S(d;T_e) = \int_0^\infty k\varepsilon \times \mathcal{T}(\varepsilon, d) \times P_0(T)\mathrm{e}^{-\varepsilon/T_e} d\varepsilon, \tag{4.16}$$

and this reduces to

$$S(d;T,A) = A\int_0^\infty \varepsilon \times \mathcal{T}(\varepsilon, d) \times \mathrm{e}^{-\varepsilon/T}\, d\varepsilon. \tag{4.17}$$

The average exposure value for the most intense region of emission for both sets of aluminium filtered pinhole images was measured and is summarised in table 4.38. This data was fitted to the model specified by 4.17 using a non-linear least squares technique. The fitted curves for both lines of sight are shown in figure 4.39. The errors quoted in the plot are those which are implied by the fitting algorithm. As such, they do not represent errors in the experimental measurement because they do not reflect the assumptions which went into the fitting model (for example the fact that signal is temporally and spatially integrated). They are quoted to give an idea of consistency between the images along different lines of sight.

The figure shows that the temperatures obtained for both lines of sight are very consistent with the value of $T_e = 100\,\mathrm{eV}$ which was measured with Thomson Scattering. The convergence of this result appeared robust in the sense that the optimisation algorithm returned similar temperatures for initial guesses to the value of T_e varying between 1 eV and 10 keV.

An obvious question to ask is what this result means in the context of my previous results which were presented in figure 4.10, in which structure corresponding to a change in target metal was seen – suggesting that emission from the target dominated the signal seen in end on pinhole images. Figure 4.40 shows the current pulse measured by the return Rogowskis for two shots. The first of these is s1016_17, which was the experiment where a target made of titanium and aluminium was fielded. The second was s0409_19 which is the experiment

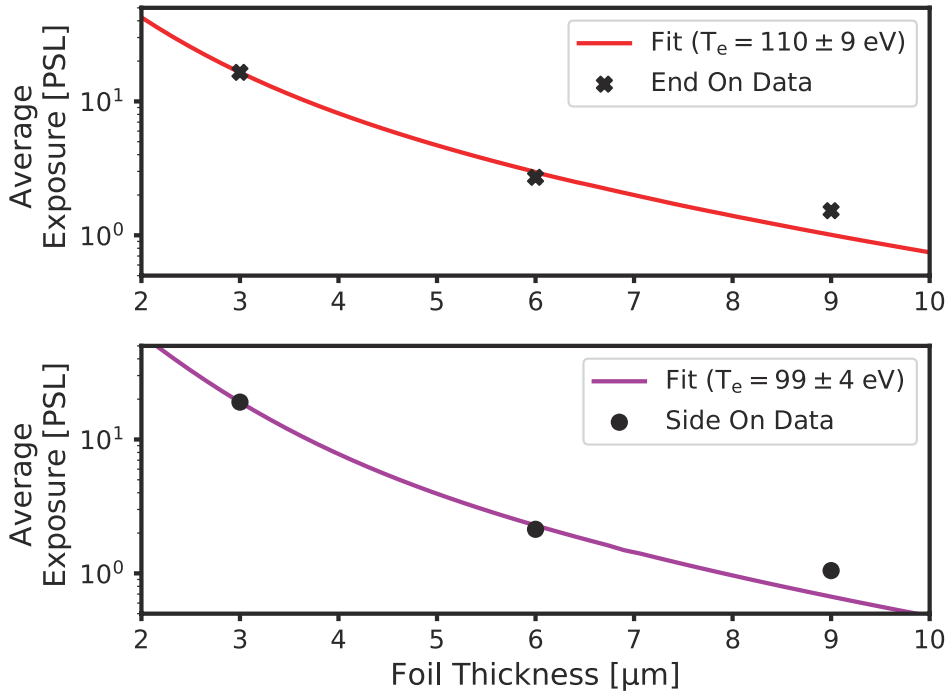

Figure 4.39: A fit of the most intense region of the signal in the sets of images shown in figures 4.33 and 4.34 to the model specified in equation 4.17. The electron temperatures obtained from both sets of images agree with with values measured by Thomson scattering.

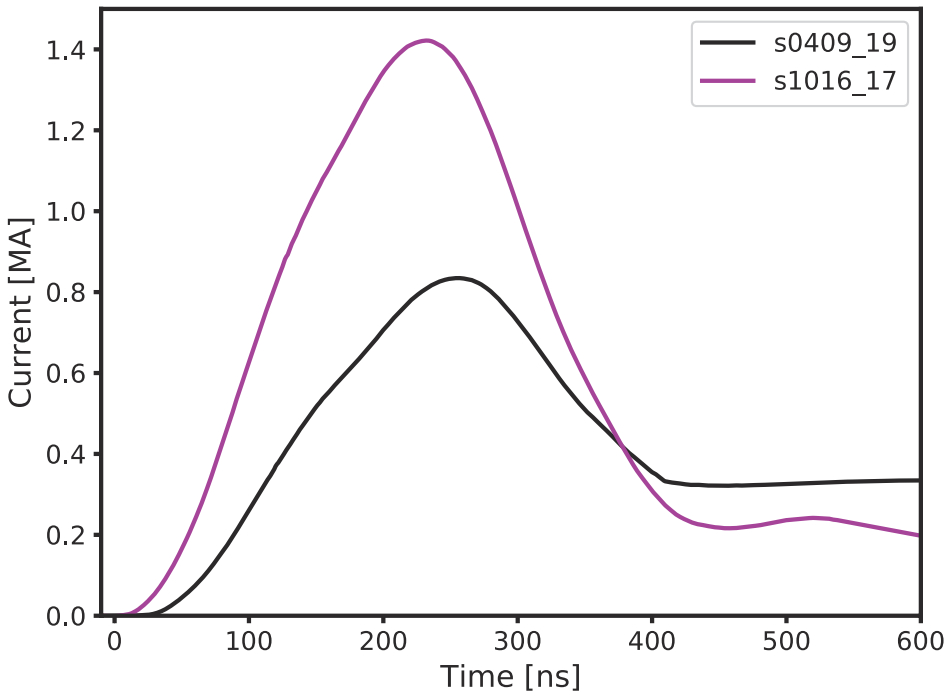

Figure 4.40: A comparison of the current pulses delivered to the loads in s1016_17 and s0409_19. The pulses were calculated from Rogowski probe measurements. The plot shows that the current pulse in s1016_17 had a peak of 1.4 MA, whereas in s0409_19 the peak current was 0.8 MA. This loss of current can likely be attributed to leakage in the MITL.

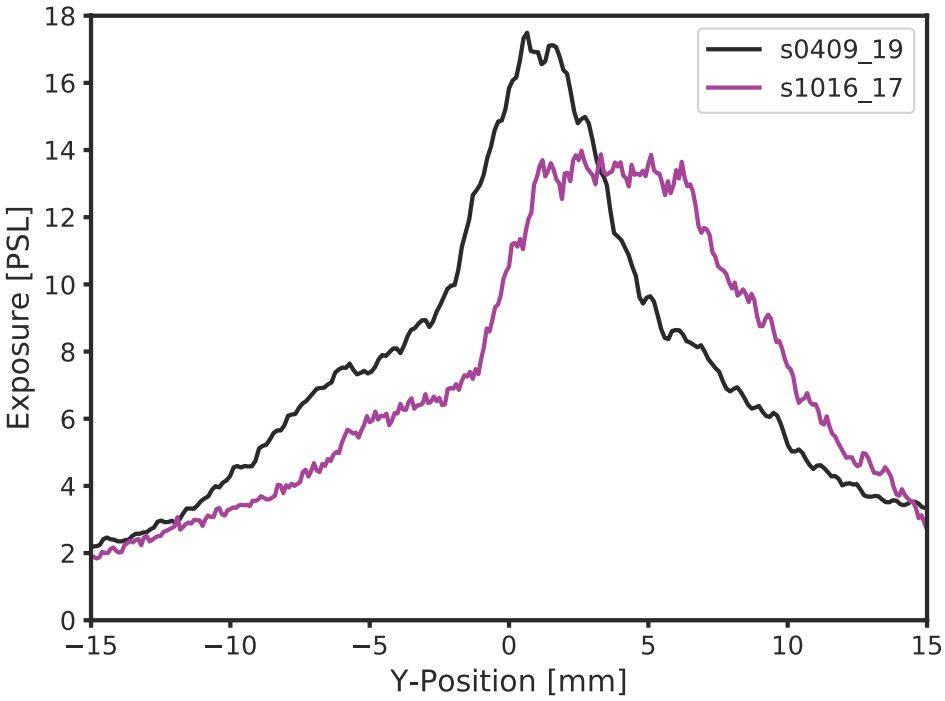

Figure 4.41: A comparison of the profile lines along the length of the layer from the images taken using 3 µm aluminium filters in s1016_17 and s0409_19. The structure of the profiles is different however the peak exposure values are similar.

in which the data which has been presented in this section was obtained.

The plot shows that the current in s1016_17 peaked at 1.4 MA whereas, in s0409_19, the peak current was just 0.8 MA. The loss of current in the second shot was likely caused by leakage in the MITL. In terms of what this reduction in peak current might mean, it is not easy to say. As I have stated previously, in experiments with exploding wire arrays at reduced current, peak inflow densities and temperatures have been observed to be slightly reduced [HarveyThompson, 2014]. It is quite difficult to speculate how this might influence the reconnection process.

A more obvious difference is that a reduction in peak current implies that the maximum voltage across the experimental volume is reduced, so the reconnecting electric field was smaller in s0409_19 than in a normal reconnection experiment. If electrons were accelerated by this electric field then it does not seem unreasonable to suggest that there exists some threshold value of electric field strength, below which acceleration does not occur – and this is essentially the approach which was adopted by Dreicer. It is a bit convoluted but not totally without foundation to speculate that such a threshold was exceeded in s1016_17 but not in s0409_19. If this were true then the intensity of the radiation measured by the camera ought to be smaller in the second experiment. Another possible interpretation is that signal from the target dominated when the target was made from aluminium but not when it was made from tungsten. Again, if this were true the signal measured in s0409_19 ought to be smaller than which was measured in s1016_17.

Figure 4.41 shows the emission profiles from the two experiments which were measured along the layer in the 3 µm aluminium images. The pinhole cameras used in the two experiments were almost identical and so the exposure curves can be compared in an absolute sense. Looking at the plot it seems clear that the peak exposures are very comparable, although the structure in the profiles are quite different. I think that what one has to take away from this is that there is no emission process present in s1016_17 which was not also contributing to the signal in s0409_19, and that means that it was actually emission from the plasma which dominated in both sets of experiments. This is obviously quite difficult to reconcile with the observation the modulation in emission which was observed in response to a change in target material which was observed in s1016_17, and I see this discrepancy as an outstanding question resulting from the work which is presented in this section.

5 Conclusions, reflections, and further work

5.1 Conclusions

The results presented in this thesis used a suite of X-Ray diagnostics to characterise a series of pulsed power driven magnetic reconnection experiments. The experimental setup consisted of two inverse wire arrays, which were driven wired in parallel, to produce counter propagating plasma flows. Measurements from a suite of laser probing and optical self emission diagnostics were used to characterise plasma flows. These results indicated that the plasma flows from the two arrays carried oppositely directed magnetic fields and that, in the region where the two flows met, magnetic flux was efficiently annihilated in a well defined reconnection layer. The magnetic energy released in the flux annihilation process was observed to cause plasma heating, and to increase fluid velocity in the outflows. The reconnection layer was observed to be unstable to the plasmoid instability, and this is consistent with the semi-collisional form of the plasmoid theory as described by [Loureiro, 2016].

Bibliography

[Banasek, 2018] J. T. Banasek, T. Byvank, S. V. R. Rocco, W. M. Potter, B. R. Kusse, and D. A. Hammer. "Time-Resolved Thomson Scattering on Laboratory Plasma Jets". In: *IEEE Transactions on Plasma Science* 99 (2018). DOI: 10.1109/TPS.2018.2850278.

[Benz, 2016] A. O. Benz. "Flare Observations". In: *Living Reviews in Solar Physics* 14.1 (Dec. 2016), p. 2.

[Bertschinger, 2004] G. Bertschinger, W. Biel, H. Jaegers, and O. Marchuk. "Compact imaging Bragg spectrometer for fusion devices". In: *Review of Scientific Instruments* 75.10 (2004). DOI: 10.1063/1.1781755.

[Biskamp, 1986] D. Biskamp. "Magnetic reconnection via current sheets". In: *Physics of Fluids* 29.5 (1986), p. 1520.

[Bland, 2004] S. N. Bland, D. J. Ampleford, S. C. Bott, S. V. Lebedev, J. B. A. Palmer, S. A. Pikuz, and T. A. Shelkovenko. "Extreme ultraviolet imaging of wire array z-pinch experiments". In: *Review of Scientific Instruments* 75.10 (2004). DOI: 10.1063/1.1787926.

[Borghesi, 2001] M. Borghesi, A. Schiavi, D. H. Campbell, M. G. Haines, O. Willi, A. J. Mackinnon, L. A. Gizzi, M. Galimberti, R. J. Clarke, and H. Ruhl. "Proton imaging : a diagnostic for inertial confinement fusion / fast ignitor studies". In: *Plasma Physics and Controlled Fusion* 43 (2001), p. 267. DOI: 10.1088/0741-3335/43/12A/320.

[Burdiak, 2012] G. C. Burdiak. "An Investigation of Cylindrical Liner Z-pinches as Drivers for Converging Strong Shock Experiments". Imperial College London, 2012.

[Byvank, 2019] J. T. Byvank, N. Hamlin, L. Atoyan, C. E. Seyler, and C. E. Kusse. "Plasma Jet Formation Disruption From a Critical Applied Uniform Axial Magnetic Field". In: *IEEE Transactions on Plasma Science* 47.7 (2019). DOI: 10.1109/TPS.2019.2920147.

[Chittenden, 2016] J. P. Chittenden, B. D. Appelbe, F. Manke, K. McGlinchey, and N. P. L. Niasse. "Signatures of asymmetry in neutron spectra and images predicted by three-dimensional radiation hydrodynamics simulations of indirect drive implosions". In: *Physics of Plasmas* 23.5 (2016). DOI: 10.1063/1.4949523.

[Dahlin, 2015] J. T. Dahlin, J. F. Drake, and M. Swisdak. "Electron acceleration in three-dimensional magnetic reconnection with a guide field". In: *Physics of Plasmas* 100704.2014 (2015).

[Dewar, 2019] A. Dewar. (Private communication). Raytek (www.raytek.co.uk), 2019.

[Drake, 2006] J. F. Drake, M. Swisdak, H. Che, and M. A. Shay. "Electron acceleration from contracting magnetic islands during reconnection". In: *Nature Letters* 443.7111 (2006), p. 553.

[Dreicer, 1959] H. Dreicer. "Electron and Ion Runaway a Fully Ionized Gas". In: *Physical Review* 115.2 (1959).

[Dyson, 1990] N. A. Dyson. *X-Rays in Atomic and Nuclear Physics*. Second Edition. Cambridge University Press, 1990.

[Ertley, 2018] C. Ertley, O. Siegmund, J. Vallerga, A. Tremsin, N. Darling, J. Hull, J. Tedesco, T. Curtis, and C. Paw. "Microchannel plate detectors for future NASA UV observatories". In: *PROCEEDINGS OF SPIE* 17.3 (2018). DOI: 10.1117/12.2314197.

[Fermi, 1949] E. Fermi. "The origin of cosmic radiation". In: *Physical Review* 2.8 (1949), p. 6.

[Fiksel, 2012] G. Fiksel, F. J. Marshall, C. Mileham, and C. Stoeckl. "Note: Spatial resolution of Fuji BAS-TR and BAS-SR imaging plates". In: *Review of Scientific Instruments* 83.8 (2012). DOI: 10.1063/1.4739771.

[Fiksel, 2014] G. Fiksel, W. Fox, A. Bhattacharjee, D. H. Barnak, P. Y. Chang, K. Germaschewski, S. X. Hu, and P. M. Nilson. "Magnetic reconnection between colliding magnetized laser-produced plasma plumes". In: *Physical Review Letters* 113.10 (2014), p. 1. DOI: 10.1103/PhysRevLett.113.105003.

[Forbes, 1991] T. G. Forbes. "Magnetic reconnection in solar flares". In: *Geophysical & Astrophysical Fluid Dynamics* 62.1-4 (1991). DOI: 10.1080/03091929108229123.

[Froula, 2011] D. H. Froula, S. H. Glenzer, N. C. Luhmann, and S. J. *Plasma Scattering of Electromagnetic Radiation. Theory and Measurement Techniques*. 2nd ed. Elsevier, 2011. DOI: 10.1016/C2009-0-20048-1.

[Gamboa, 2011] E. J. Gamboa, D. S. Montgomery, I. M. Hall, and R. P. Drake. "Imaging X-ray crystal spectrometer for laser-produced plasmas". In: *Journal of Instrumentation* 6.04 (2011). DOI: 10.1088/1748-0221/6/04/p04004.

[Gosling, 2012] J. T. Gosling. "Magnetic Reconnection in the Solar Wind". In: *Space Science Reviews* 172 (2012). DOI: 10.1007/s11214-011-9747-2.

[Gullikson, 1994] E. M. Gullikson, P. Denham, S. Mrowka, and U. J. H. "Absolute photoabsorption measurements of Mg, Al, and Si in the soft-x-ray region below the $L_{2,3}$ edges". In: *Physical Review B* 49.23 (1994). DOI: 10.1103/PhysRevB.49.16283.

[Hall, 2006] G. N. Hall, S. A. Pikuz, T. A. Shelkovenko, S. N. Bland, S. V. Lebedev, D. J. Ampleford, J. B. A. Palmer, S. C. Bott, J. Rapley, J. P. Chittenden, and J. P. Apruzese. "Structure of stagnated plasma in aluminum wire array Z pinches". In: *Physics of Plasmas* 13.8 (2006). DOI: 10.1063/1.2234284.

[Hare, 2017a] J. D. Hare, S. V. Lebedev, L. G. Suttle, N. F. Loureiro, A. Ciardi, G. C. Burdiak, J. P. Chittenden, G. F. Swadling, J. Ma, and J. Wu. "Formation and Structure of a Current Sheet in Pulsed-Power Driven Magnetic Reconnection Experiments". In: *Physics of Plasmas* (2017), p. 1.

[Hare, 2017b] J. D. Hare, L. Suttle, S. V. Lebedev, N. F. Loureiro, A. Ciardi, G. C. Burdiak, J. P. Chittenden, T. Clayson, C. Garcia, N. Niasse, T. Robinson, R. A. Smith, N. Stuart, G. F. Swadling, J. Ma, J. Wu, and Q. Yang. "Anomalous Heating and Plasmoid Formation in a Driven Magnetic Reconnection Experiment". In: *Physical Review Letters* 085001.February (2017), p. 1. DOI: 10.1103/PhysRevLett.118.085001.

[Hare, 2019] J. D. Hare, J. N. MacDonald, S. N. Bland, J. Dranczewski, J. W. D. Halliday, S. V. Lebedev, L. G. Suttle, T. E. R., and W. Rozmus. "Two-colour interferometry and Thomson scattering measurements of a plasma gun". In: *Plasma Phys. Control. Fusion* 61.085012 (2019). DOI: 10.1088/1361-6587/ab2571.

[HarveyThompson, 2014] A. J. Harvey-Thompson, S. V. Lebedev, S. N. Bland, J. P. Chittenden, G. N. Hall, A. Marocchino, S. C. Bott, J. B. A. Palmer, and C. Ning. "Quantitative analysis of plasma ablation using inverse wire array Z pinches". In: *Physics of Plasmas* 022701.2009 (2014). DOI: 10.1063/1.3077305.

[Hecht, 2016] E. Hecht. *Optics, Global Edition*. Pearson Education Limited, 2016.

[Henke, 1993] B. L. Henke, E. M. Gullikson, and J. C. Davis. "X-ray interactions: photoabsorption, scattering, transmission, and reflection at E=50-30000 eV, Z=1-92". In: *Atomic Data and Nuclear Data Tables* 54.2 (1993), p. 181.

[Howard, 2018] A. Howard, D. Haberberger, R. Boni, R. Brown, and D. H. Froula. "Implementation of a Wollaston interferometry diagnostic on OMEGA EP". In: *Review of Scientific Instruments* 89.10B107 (2018). DOI: 10.1063/1.5036956.

[Hutchinson, 2002] I. H. Hutchinson. *Principles of Plasma Diagnostics*. Cambridge University Press, 2002. DOI: 10.1017/CBO9780511613630.

[Katz, 2013] J. Katz, J. S. Ross, C. Sorce, and D. H. Froula. "A reflective image-rotating periscope for spatially resolved Thomson-scattering experiments on OMEGA". In: *Journal of Instrumentation* 8.12 (2013). DOI: 10.1088/1748-0221/8/12/c12009.

[Krucker, 2010] S. Krucker, H. S. Hudson, L. Glesener, S. M. White, S. Masuda, J. P. Wuelser, and R. P. Lin. "Measurements of the coronal acceleration region of a solar flare". In: *Astrophysical Journal* 714.2 (2010), p. 1108. DOI: 10.1088/0004-637X/714/2/1108.

[Ladislas Wiza, 1979] J. Ladislas Wiza. "Microchannel plate detectors". In: *Nuclear Instruments and Methods* 162.1 (1979). DOI: 10.1016/0029-554X(79)90734-1.

[Leblans, 2011] P. Leblans, D. Vandenbroucke, and P. Willems. "Storage Phosphors for Medical Imaging". In: *Materials* 4.6 (2011). DOI: 10.3390/ma4061034.

[Lemen, 2012] J. R. Lemen, A. M. Title, D. J. Akin, P. F. Boerner, C. Chou, J. F. Drake, D. W. Duncan, C. G. Edwards, F. M. Friedlaender, G. F. Heyman, N. E. Hurlburt, N. L. Katz, G. D. Kushner, M. Levay, R. W. Lindgren, D. P. Mathur, E. L. McFeaters, and S. Mitchell. "The Atmospheric Imaging Assembly (AIA) on the Solar Dynamics Observatory (SDO)". In: *Solar Physics* 276.17-40 (2012). DOI: 10.1007/s11207-011-9776-8.

[Loureiro, 2007] N. F. Loureiro, S. C. Cowley, W. D. Dorland, M. G. Haines, and A. A. Schekochihin. "Instability of current sheets and formation of plasmoid chains". In: *Physics of Plasmas* 14.10 (2007).

[Loureiro, 2016] N. F. Loureiro and D. A. Uzdensky. "Magnetic reconnection: from the Sweet-Parker model to stochastic plasmoid chains". In: *Plasma physics and controlled fusion* 58.014021 (2016).

[Lyubarsky, 2000] Y. Lyubarsky and J. G. Kirk. "Reconnection in a Striped Pulsar Wind". In: *The Astrophysical Journal* 547.1 (2000). DOI: 10.1086/318354.

[McPherson, 2016] L. A. McPherson, D. J. Ampleford, C. A. Coverdale, J. W. Argo, A. C. Owen, and D. M. Jaramillo. "High energy X-ray pinhole imaging at the Z facility". In: *Review of Scientific Instruments* 87.6 (June 2016). DOI: 10.1063/1.4953004.

[Meadowcroft, 2008] A. L. Meadowcroft, C. D. Bentley, and E. N. Stott. "Evaluation of the sensitivity and fading characteristics of an image plate system for x-ray diagnostics". In: *Review of Scientific Instruments* 79.11 (2008). DOI: 10.1063/1.3013123.

[Mitchell, 1996] I. H. Mitchell, J. M. Bayley, J. P. Chittenden, J. F. Worley, A. E. Dangor, M. G. Haines, and P. Choi. "A high impedance mega ampere generator for fiber z-pinch experiments". In: *Review of Scientific Instruments* 67.4 (1996), p. 1533. DOI: 10.1063/1.1146884.

[Moore, 2009] J. H. Moore, C. C. Davis, M. A. Coplan, and G. S. C. *Building Scientific Apparatus*. Cambridge University Press, 2009.

[Nilson, 2006] P. M. Nilson, L. Willingale, M. C. Kaluza, C. Kamperidis, S. Minardi, M. S. Wei, P. Fernandes, M. Notley, S. Bandyopadhyay, M. Sherlock, R. J. Kingham, M. Tatarakis, Z. Najmudin, W. Rozmus, R. G. Evans, M. G. Haines, A. E. Dangor, and K. Krushelnick. "Magnetic reconnection and plasma dynamics in two-beam laser-solid interactions". In: *Physical Review Letters* 97.25 (2006), p. 1. DOI: 10.1103/PhysRevLett.97.255001.

[OptoDiode, 2017] OptoDiode. *AXUV Series Absolute UV Silicon Photodiodes*. 2017.

[Parker, 1957] E. N. Parker. "Sweet's mechanism for merging magnetic fields in conducting fluids". In: *Journal of Geophysical Research* 62.4 (1957). DOI: 10.1029/JZ062i004p00509.

[Parkes, 1970] W. Parkes, R. Gott, and R. A. Pounds. "Soft X-Ray Studies of Channel Multipliers and Multiplier Arrays". In: *IEEE Transactions on Nuclear Science* 17.3 (1970). DOI: 10.1109/TNS.1970.4325713.

[Patankar, 2015] S. Patankar, E. T. Gumbrell, T. S. Robinson, H. F. Lowe, S. Giltrap, C. J. Price, N. H. Stuart, P. Kemshall, J. Fyrth, J. Luis, J. W. Skidmore, and R. A. Smith. In: *Applied Optics* 36 (2015). DOI: 10.1364/AO.54.010592.

[Pikuz, 2008] S. A. Pikuz, J. D. Douglass, T. A. Shelkovenko, D. B. Sinars, and D. A. Hammer. "Wide band focusing x-ray spectrograph with spatial resolution". In: *Review of Scientific Instruments* 79.1 (2008), p. 013106. DOI: 10.1063/1.2834834.

[Pikuz, 2015] S. A. Pikuz, T. A. Shelkovenko, and D. A. Hammer. "-Pinch. Part I". In: *Plasma Physics Report* 41.4 (2015). DOI: 10.1134/S1063780X15040054.

[Pikuz, 2016] S. A. Pikuz. (Private communication). 2016.

[Priest, 2000] E. Priest and T. Forbes. *Magnetic Reconnection*. Cambridge University Press, 2000.

[Raymond, 2016] A. Raymond, C. F. Dong, A. McKelvey, C. Zulick, N. Alexander, T. Batson, A. Bhattacharjee, P. Campbell, H. Chen, V. Chvykov, E. Del Rio, P. Fitzsimmons, W. Fox, B. Hou, A. Maksimchuk, C. Mileham, J. Nees, P. M. Nilson, C. Stoeckl, A. G. R. Thomas, M. S. Wei, V. Yanovsky, L. Willingale, and K. Krushelnick. *Relativistic Magnetic Reconnection in the Laboratory*. 2016. arXiv: 1610.06866 [plasm-ph].

[Reader, 2000] J. Reader, C. J. Sansonetti, and R. D. Deslattes. "Image plates for registration of far-ultraviolet spectra". In: *Applied Optics* 39.4 (2000). DOI: 10.1364/AO.39.000637.

[Richardson, 2019] A. S. Richardson. *NRL Plasma Formulary*. 2019.

[Ryutov, 2015] D. D. Ryutov. "Characterizing the Plasmas of Dense Z -Pinches". In: *IEEE Transactions on Plasma Science* 43.8 (2015). DOI: 10.1109/TPS.2015.2453265.

[Schekochihin, 2020] A. Schekochihin. *Lectures on Kinetic Theory and Magnetohydrodynamics of Plasmas*. 2020.

[Sinars, 2006] D. B. Sinars, D. F. Wenger, K. L. Keller, G. A. Rochau, and J. L. Porter. "Focusing, adjustable spectrometer with temporal resolution for the Sandia Z facility". In: *Review of Scientific Instruments* 77.10 (2006). DOI: 10.1063/1.2336727.

[Suttle, 2016] L. G. Suttle, J. D. Hare, S. V. Lebedev, G. F. Swadling, G. C. Burdiak, A. Ciardi, J. P. Chittenden, N. F. Loureiro, N. Niasse, J. Wu, Q. Yang, T. Clayson, A. Frank, T. S. Robinson, R. A. Smith, and N. Stuart. "Structure of a Magnetic Flux Annihilation Layer Formed by the Collision of Supersonic , Magnetized Plasma Flows". In: *Physical Review Letters* 225001.June (2016), p. 1. DOI: 10.1103/PhysRevLett.116.225001.

[Swadling, 2011] G. Swadling. "An experimental investigation of the azimuthal structures formed during the ablation phase of wire array z-pinches". Imperial College London, 2011.

[Swadling, 2014] G. F. Swadling, S. V. Lebedev, G. N. Hall, S. Patankar, N. H. Stewart, R. A. Smith, C. Burdiak, P. D. Grouchy, J. Skidmore, L. Suttle, S. N. Bland, K. H. Kwek, L. Pickworth, J. D. Hare, W. Rozmus, J. Yuan, G. F. Swadling, S. V. Lebedev, G. N. Hall, S. Patankar, and N. H. Stewart. "Diagnosing collisions of magnetized , high energy density plasma flows using a combination of collective Thomson scattering , Faraday rotation , and interferometry". In: *Review of scientific instruments* 85.2013 (2014). DOI: 10.1063/1.4890564.

[Sweet, 1958] P. A. Sweet. "The Neutral Point Theory of Solar Flares". In: *Electromagnetic Phenomena in Cosmical Physics*. Vol. 6. IAU Symposium. 1958.

[Theobald, 2018] W. Theobald, C. Sorce, M. Bedzyk, S. T. Ivancic, F. J. Marshall, C. Stoeckl, R. C. Shah, M. Lawrie, S. P. Regan, T. C. Sangster, E. M. Campbell, T. J. Hilsabeck, K. Englehorn, J. D. Kilkenny, D. Morris, T. M. Chung, J. D. Hares, A. K. L. Dymoke-Bradshaw, P. Bell, J. Celeste, A. C. Carpenter, M. Dayton, D. K. Bradley, M. C. Jackson, L. Pickworth, S. R. Nagel, G. Rochau, J. Porter, M. Sanchez, L. Claus, G. Robertson, and Q. Looker. "The single-line-of-sight, time-resolved x-ray imager diagnostic on OMEGA". In: *Review of Scientific Instruments* 89.10 (2018). DOI: 10.1063/1.5036767.

[Thompson, 1994] C. Thompson. "A model of gamma-ray bursts". In: *Monthly Notices of the Royal Astronomical Society* 270.3 (1994). DOI: 10.1093/mnras/270.3.480.

[Totorica, 2017] S. R. Totorica, T. Abel, and F. Fiuza. "Particle acceleration in laser-driven magnetic reconnection". In: *Physics of Plasmas* (2017).

[Yamada, 1994] M. Yamada, F. M. Levinton, N. Pomphrey, R. Budny, J. Manickam, and Y. Nagayama. "Investigation of magnetic reconnection during a sawtooth crash in a high-temperature tokamak plasma". In: *Physics of Plasmas* 1.10 (1994). DOI: 10.1063/1.870479.

[Yamada, 1997] M. Yamada, H. Ji, S. Hsu, T. Carter, R. Kulsrud, N. Bretz, F. Jobes, Y. Ono, and F. Perkins. "Study of driven magnetic reconnection in a laboratory plasma". In: *Physics of Plasmas* 4.5 (1997), p. 1936. DOI: 10.1063/1.872336.

[Yamada, 2006] M. Yamada, Y. Ren, H. Ji, J. Breslau, S. Gerhardt, R. Kulsrud, and A. Kuritsyn. "Experimental study of two-fluid effects on magnetic reconnection in a laboratory plasma with variable collisionality". In: *Physics of Plasmas* 13.5 (2006). DOI: 10.1063/1.2203950.

[Zeldovich, 1966] B. Zeldovich and R. P. *Physics of Shock Waves and High-temperature Hydrodynamic Phenomena*. Dover Edition, 1966.

[Zhong, 2010] J. Zhong, Y. Li, X. Wang, J. Wang, Q. Dong, C. Xiao, S. Wang, X. Liu, L. Zhang, L. An, F. Wang, J. Zhu, Y. Gu, X. He, G. Zhao, and J. Zhang. "Modelling loop-top X-ray source and reconnection outflows in solar flares with intense lasers". In: *Nature Physics* 6.12 (2010), p. 984. DOI: 10.1038/nphys1790.

[Zweibel, 2009] E. G. Zweibel and M. Yamada. "Magnetic Reconnection in Astrophysical and Laboratory Plasmas". In: *Annual Review of Astronomy and Astrophysics* 47.1 (2009), p. 291. DOI: 10.1146/annurev-astro-082708-101726.

[Zweibel, 2016] E. G. Zweibel and M. Yamada. "Perspectives on magnetic reconnection". In: *Proceedings of the Royal Society A: Mathematical, Physical and Engineering Sciences* 472.2196 (2016). DOI: 10.1098/rspa.2016.0479.

Written Copyright Permissions

Copyright permissions for this thesis. The location of the item in this thesis is shown in the first column by the figure number it appears in, the source of the material is shown in the second column and the year and copyright holder in the third column. Written permission has been obtained for **all** items prior to use in this thesis, and these permissions are shown on the subsequent pages, in the same order as they appear in this table.

Figure	Source	Copyright holder